THE MEASUREMENTS OF NEUTRON AND GAMMA DOSE RATES IN MIXED RADIATION FIELDS, USING A LIQUID SCINTILLATION COUNTER

by

BASHIR IBRAHIM OMAR SHAKSHAK

A thesis submitted for the degree of

Doctor of Philosophy

THE UNIVERSITY OF ASTON IN BIRMINGHAM

March, 1989

THE UNIVERSITY OF ASTON IN BIRMINGHAM

THE MEASUREMENT OF NEUTRON AND GAMMA DOSE RATES IN MIXED RADIATION FIELDS, USING A LIQUID SCINTILLATION COUNTER

by

BASHIR IBRAHIM OMAR SHAKSHAK

A thesis submitted for the degree of

Doctor of Philosophy

March, 1989

SUMMARY

Measurements of neutron and gamma dose rates in mixed radiation fields, and gamma dose rates from calibrated gamma sources, were performed using a liquid scintillation counter NE213 with a pulse shape discrimination technique based on the charge comparison method.

A computer program was used to analyse the experimental data.

The radiation field was obtained from a ^{241}Am-^{9}Be source.

There was general agreement between measured and calculated neutron and gamma dose rates in the mixed radiation field, but some disagreement in the measurements of gamma dose rates for gamma sources, due to the dark current of the photomultiplier and the effect of the perturbation of the radiation field by the detector.

An optical fibre bundle was used to couple an NE213 scintillator to a photomultiplier, in an attempt to minimise these effects. This produced an improvement in the results for gamma sources. However, the optically coupled detector system could not be used for neutron and gamma dose rate measurements in mixed radiation fields. The pulse shape discrimination system became ineffective as a consequence of the slower time response of the detector system.

Key words: MIXED (NEUTRON + GAMMA) RADIATION FIELDS,
NEUTRON AND GAMMA DOSE MEASUREMENTS,
FIBRE BUNDLES, FIBRE COUPLING.

TO MY FAMILY

ACKNOWLEDGEMENTS

I am very much indebted to my supervisor, Dr.A.Bore, for his continuous guidance and supervision throughout the project work.

I wish to express my sincere gratitude to Dr.P.N.Cooper for his invaluable advice and constant encouragement throughout this work.

I am also grateful to Professor T.M.Mulvey and other members of the academic staff for many valuable discussions throught the project work.

My thanks to the Physics workshop staff for their help in building the experimental components.

Finally, I wish to express my thanks to my wife, Sobhia, for the sacrifices made throughout this work and to my son, Omar, a constant source of pleasure and encouragement for the future.

CONTENTS

LIST OF SYMBOLS

Bq	Bequerel (2.7×10^{-11} Curie)
DE	Dose equivalent
DF	Distribution factor
G_y	Gray (100 rad)
I.A.E.A.	International Atomic Energy Agency
I.C.R.U.	International Commission for Radiological Protection and Units
I.E.N.E.A.	International and European Nuclear Energy Agency
LET	Linear energy transfer (kev / μm)
N.B.S.	National Bureau of Standards
NA	Numerical aperture = ($\sin \theta_c$)
q	Dose per unit flux for neutrons of source energy (μGy per $n.cm^{-2}\ s^{-1}$)
QF	Quality factor
R	Units of exposure dose (roentgen)
Rad	Units of absorbed dose
RBE	Relative biological effectiveness
rem	Roentgen equivalent man (units of dose equivalent)
Sv	Sievert (100 rem)
TLD	Thermoluminescent dosimeter

LIST OF TABLES

LIST OF FIGURES

CHAPTER ONE: NUCLEAR RADIATION AND THE HUMAN BODY

1.1 Biological Effects of Nuclear Energy Deposition:

In the process of losing energy to an absorbing medium, a variety of direct and indirect effects occur that depend, not only on the atomic composition of the absorber, but also on the molecular makeup, its crystal structure and the nature of the surrounding material. Ionization of atoms and molecules may lead to the breaking of chemical bonds or the formation of new ones, the energy deposited in the complex molecules may lead to excitation to higher vibrational or rotational states, and the resulting rise in temperature in a larger assembly of irradiated molecules may result in more rapid chemical reaction rates or in faster diffusion. Thus a whole branch of chemistry has grown around such radiation-induced or radiation-effected reactions.

Many of the bombardment reactions lead to the production of secondary atoms, produced by the recoil of atoms of the target material in scattering events. In other cases, such as the capture of neutrons, energetic heavily charged ions are introduced into the medium causing a variety of secondary events; but always resulting in a transfer of energy from the incident particle to the target medium, with a steady, often indirect, degradation of the initial kinetic energy to heat, i.e. vibrational energy of the target atom. The amount of energy thus transferred to the medium and converted to chemical energy or heat is usually called the dose to that medium. More formally the absorbed dose D is defined as:

$$\text{Absorbed dose} \quad D = \frac{\Delta E}{\Delta m}$$

i.e. the dose equals the change in kinetic energy per unit mass absorbed as the radiation

traverses the material. Since most chemical, physical and biological effects in the target material depend on this quantity, the determination of dose is a major field of radiation measurement, and various instruments (i.e. dosimeters) have been designed specifically for this purpose.

One of the major applications of dosimetry is for the determination of dose in human tissue. Although the chemical composition of tissue, made up as it is of hydrogen, carbon, oxygen and a variety of lesser elements, appears to vary little from one form of tissue to another, the highly specialised nature of the molecules forming the various organs and tissues makes them susceptible to radiation to a varying degree, with more highly specialised material and cells with high mitotic activity being particularly susceptible to damage.

In the sense of biological effects of nuclear radiation to the human body, radiation exposure may be chronic or acute. Chronic exposure implies continual exposure over a long period of time leading to a given total dose value. Acute exposure refers to sudden, perhaps massive, radiation exposure such as might arise in radiation therapy or a nuclear explosion.

1.2 Radiation Units:

(i) The unit of exposure dose is the roentgen (R), that quantity of X- or gamma radiation producing a charge of 2.58×10^{-4} C kg^{-1} of air at 0°C and 1 atmospheric pressure. Either sign of air pair carries a charge of 1.602×10^{-19} C, therefore:
1R corresponds to the production of 1.6×10^{15} ion pairs kg^{-1}.

Since the average energy to produce an ion pair is 5.47×10^{-18} J in air and 6×10^{-18} J in tissue, the energy absorption which corresponds to an exposure of 1R is equal to 8.77×10^{-3} J kg^{-1} in air and 9.7×10^{-3} J kg^{-1} in tissue.

The roentgen (R) applies only to the exposure dose from X- or gamma radiation.

(ii) The absorbed dose in any ionizing radiation is the amount of energy imparted to the matter by ionizing particles per unit mass of irradiated material at the place of interest. It is measured in rads or gray.

$$1 \text{ gray } (G_y) = 100 \text{ rad} = 1 \text{ J kg}^{-1}$$

1R corresponds to 8.77×10^{-3} G_y in air or 9.7×10^{-3} G_y in water (soft tissue).

(iii) The dose equivalent is defined as the product of absorbed dose (D), quality factor (QF), dose distribution factor (DF) and many other factors introduced for radiation protection purposes. The dose equivalent is essentially a measure of the biological risk incurred for a given radiation dose. The unit of dose equivalent (DE) is the rem (roentgen equivalent man) or the Sievert (Sv).

$$1 \text{ Sv} = 100 \text{ rem}$$

The distribution factor (DF) is a product of various modifying factors to allow for non-uniformity of distribution of a given radiation source to the organ under observation and other geometric sensitive effects.

The quality factor denotes the biological effectiveness of a given radiation dose by virtue

of the linear energy transfer (LET) of the medium traversed by the radiation. The quality factor is also related to the relative biological effectiveness (RBE), used generally in radiation biology. However, for radiation protection purposes, the values of (RBE) for man are not well known and are replaced by standard average values for different types of radiation. Table (1.1.) compares these factors for principle radiation types.

Radiation	Energy (Mev)	Av LET (kev/μm)	RBE	Quality factor
X-rays	0.01-0.2	3.0	1.0	1
Gamma rays	1.25	0.3	0.7	1
	4.0	0.3	0.6	1
Electrons (β)	0.1	0.42	1.0	1
	0.6	0.3	1.3	1
	1.0	0.25	1.4	-
Protons	0.1	90	-	6
	2.0	16	2	10
	5.0	8	2	10
Alpha particles	0.1	260	-	-
	5.0	95	10-20	10
Heavy ions	10-30	~ 150	~ 25	20
Neutrons	2.5×10^{-8}	-	4-5	3
	1.0	20	2-10	10

Table 1.1: Representative values of LET, RBE and quality factor for different types of radiation. (Geoffrey G. Eichholz, John W.Poston).

1.3 Dose Rate:

The roentgen, gray and sievert are units expressing radiation dose received over a period of time. In limiting radiation hazard it is usually necessary to know the rate at which the radiation is being received.

1.3.1 Dose Rate from Gamma Ray Sources:

Gamma radiation is the most common source producing an external radiation hazard because α and β radiation can be completely absorbed by a comparatively small thickness of absorber.

The energy flux I(r,E) at a distance r from a point gamma source can be presented by the following expression:

$$I(r,E) = \frac{3.7\times10^{10}\times2.7\times10^{-11}}{4\Pi r^2} BE$$

$$= 7.95 \times 10^{-2} \frac{BE}{r^2}$$

where:

I = Energy flux (Mev cm^{-2} s^{-1})

B = The activity of the source (Bq)

E = The energy of the activity (Mev / disintegration)

r = The distance in cm from the point source to the field position (at which the flux is measured).

The exposure dose (R_{exp}) = $I(r,E)\ \mu ea_{air}$ (Mev $cm^{-3}\ s^{-1}$)

μea_{air} is the energy absorption coefficient (cm^{-1}).

Hence, since 1R = 7.08×10^4 Mev cm^{-3} in air, the absorbed dose (G_y) will be equal to:

$$D_{abs} = 8.77 \times 10^{-3} \frac{(\mu ea/\rho)_{med}}{(\mu ea/\rho)_{air}} R_{exp} \quad \text{.....1.1} \quad \text{(Fitzgerald 1967)}$$

$$= \frac{8.77 \times 10^{-3} \times 7.95 \times 10^{-2} \times 3.6 \times 10^{3}}{7.08 \times 10^{4}} \mu ea_{air} \frac{(\mu ea/\rho)_{med}}{(\mu ea/\rho)_{air}} \frac{BE}{r^2} (G_y h^{-1})$$

$$= 3.54 \times 10^{-5} \mu ea_{air} \frac{(\mu ea/\rho)_{med}}{(\mu ea/\rho)_{air}} \frac{BE}{r^2} (G_y h^{-1}) \quad \text{.....1.2}$$

An approximate form of this equation is arrived at by substituting the following values:

μea_{air} = 3.5×10^{-5} cm^{-1} (In the energy range of 0.07 → 3 Mev)

$(\mu ea/\rho)_{water}$ = 0.0309 $cm^2\ g^{-1}$ (In the energy range of 1.25 Mev)

$(\mu ea/\rho)_{air}$ = 0.0278 $cm^2\ g^{-1}$ (In the energy range of 1.25 Mev)

$$D_{abs} = 1.38 \times 10^{-13} \frac{BE}{r^2} (G_y\ h^{-1}) \quad \text{(r-metres)}$$

1.3.2 Dose Rate from Neutron Sources:

The measurement of absorbed dose from neutrons is such a difficult measurement to make that the International Commission on Radiological Protection (I.C.R.P.) has recommended that the quantity flux can be used. Flux is simply the number of neutrons falling in each cm^2 of surface area per sec. The neutron flux $\phi(n.cm^{-2}\ s^{-1})$ from a source of strength $S(n.s^{-1})$ at a distance r (cm) from a detector can be calculated using the inverse square law:

$$\phi = \frac{S}{4\Pi r^2}$$

The flux has been related to the dose equivalent (Sv) for all ranges of neutron energies (Snyder 1957, N.B.S. Handbook 63).

1.3.3 Neutron and Gamma Dosimetry:

As both dose and dose equivalent depend on the nature of the tissue irradiated and on target geometry, it is often found that the introduction of a dosimeter may affect the measurement by additional scattering or absorption effects in the instrument materials. For this reason much effort has been devoted to the development of "tissue equivalent" dosimeters, whose composition and structure do not change any of the dose and exposure conditions. Typically, a tissue-equivalent detector should be so small as to cause negligible disturbance, or it should be constructed of materials whose atomic composition closely matches that of the surrounding tissue. It should be remembered that tissue equivalence for X- or γ-radiation, which depends mainly on electron density, is not the same as tissue equivalence for neutrons, which depends on capture and scattering

cross sections.

As radiation exposure may be chronic or acute (Section 1.1), dosimeters have to be designed to operate at low or high dose levels, to have rapid response times or to integrate and hold the reading over long periods. No instrument, in general, can be expected to meet all requirements and a careful selection must be made to obtain the desired sensitivity and performance. Some instruments must be capable of recording dose accurately in mixed radiation fields, i.e. in the presence of both neutrons and gamma-rays; while others are expected to discriminate, with only low sensitivity, to the interfering radiations. In some cases different absorbers may be introduced to distinguish between effects from different radiations, such as in the "film badge". The lead foils filter out X-rays and gamma-rays of various energy ranges, while the indium foil discriminates against thermal neutrons and the plastic sheet slows down fast neutrons.

1.3.3.1 Tissue Absorbed Dose from X- or Gamma Radiation:

The absorbed dose at a point in air or air-equivalent material that is surrounded on all sides by such material to a thickness at least equal to the range of the secondary electrons and uniformally exposed to one roentgen of X- or gamma-radiation is equal to 8.77×10^{-3} G_y. The absorbed dose at some point within an irradiated medium can be measured indirectly by a roentgen-calibrated ionization chamber, which can be positioned at the point within the medium. The calibration of the chamber should be corrected for the spectrum of the X-rays present at the point in the medium. The walls of the ionization chamber should be thick enough to exclude electrons generated in the irradiated medium. In position, the chamber measures a perturbed exposure X' (roentgen). The exposure

which would exist at the point in the absence of the chamber is $X = AX'$; where A is the correction factor which accounts for all perturbation effects. The ratio X / X' varies, mainly by: (a) Attenuation and scattering of X-rays in that amount of medium which is displaced by the insertion of the chamber and (b) X-ray scattering from the chamber connecting lead, if one is used. Modern ionization chambers can be made so small that X / X' is very nearly equal to unity.

Having thus established X at the point of interest, in roentgen, the absorbed dose in the medium (D_{med}) in G_y is obtained from equation (1.1):

$$D_{abs} = 8.77 \times 10^{-3} \left[\frac{(\mu ea/\rho)_{med}}{(\mu ea/\rho)_{air}} \right] X$$

where $(\mu ea/\rho)$ is the mass energy-absorption coefficients of the medium and/or of air, evaluated for the total spectrum of X- or gamma radiation arriving at the point of interest. In the event that no roentgen calibrated ionization chamber is available, absorbed dose can be measured with an air filled cavity ionization chamber, having walls that are very thin compared with the range of the secondary electrons. If the walls are so thin that they make a negligible contribution to the total secondary electron emission that ionizes the air in the chamber, the material of which the walls are composed is not important. If a charge Q is carried by the ions of either sign generated per 1.293×10^{-6} kg of air then,by applying the general cavity relation (1.1), D_{med} is given by 8.77×10^{-3} Q S_m G_y, where S_m is evaluated for the electron spectrum at the point of interest.

1.3.3.2 Interaction of Neutrons with Tissue:

A neutron incident on a slab of tissue will either penetrate it without interaction or will interact with it in one of the following ways:

(i) Elastically, (ii) inelastically, (iii) non-elastically, (iv) by being captured, (v) by causing spallation.

Inelastic reactions include $^{12}C(n, n' \gamma)^{12}C$; non-elastic reactions result in the emission of charged particles; e.g. $^{16}O(n, \alpha)^{13}C$; spallation occurs at neutron energies greater than 20 Mev.

The important capture reactions are $^{1}H(n, \gamma)^{2}H$ and $^{14}N\ (n, p)\ ^{14}C$

The contribution to the first collision absorbed dose from elastic scattering and radioactive capture events can be calculated using the following relation (Fitzgerald, 1967):

Dose rate (μ Gy h^{-1}) =

$$5.76 \times 10^{-4}\ \phi\ (E_n) \times \left[\Sigma_{n,p}\ (E_n)\ \frac{4A}{(A+1)^2}\ E_n + \Sigma_{n,\gamma}\ (E_n)\ E_\gamma\ B \right] \quad \ldots\ldots\ldots 1.3$$

where:

$\phi(E_n)$ = The neutron flux in ($n.cm^{-2}\ s^{-1}$)

E_γ = The radioactive capture gamma photon energy in Mev

A = The atomic mass number of target nucleus

B = A factor representing the fraction of radioactive capture gamma photon energy absorbed in the neighbourhood of

the capture

$\frac{4A}{(A+1)^2}$ = The maximum fraction of incident neutron energy imparted to the recoil nucleus.

$\Sigma_{n,p}$ = The macroscopic elastic-scattering cross section.

ıe constant factor 5.76×10^{-4} represents the energy to dose rate conversion factor Mev = 1.602×10^{-13} J and $1Gy = 1J\,kg^{-1}$] .

r energies below 10 Mev, isotropic elastic scattering dominates and therefore (n,γ) m can be ignored in equation (1.3).

ɛ major energy loss is from elastic collisions with hydrogen nuclei and accounts for re than 90% of the absorbed dose.

A plastic material containing the same percentage of hydrogen and nitrogen as a tissue is often used as a wall material in tissue equivalent ionization chambers. Absorbed dose from fast neutrons can be enhanced by the use of materials even richer in hydrogen, such as polyethylene $(C_2H_4)n$. The absorbed dose in this material is about 1.45 times that in tissue for neutron energies extended to 14 Mev. Fast neutron dose can be substantially reduced below that in tissue by using a detector made of non-hydrogenous materials. For example, the fast neutron kerma ($J\,kg^{-1}$) in carbon in the range from 0.1 to 8 Mev is only 10-20% of that in tissue, and the kerma in intermediate atomic number materials, such as magnesium and aluminium, is even less (Figure 1.1).

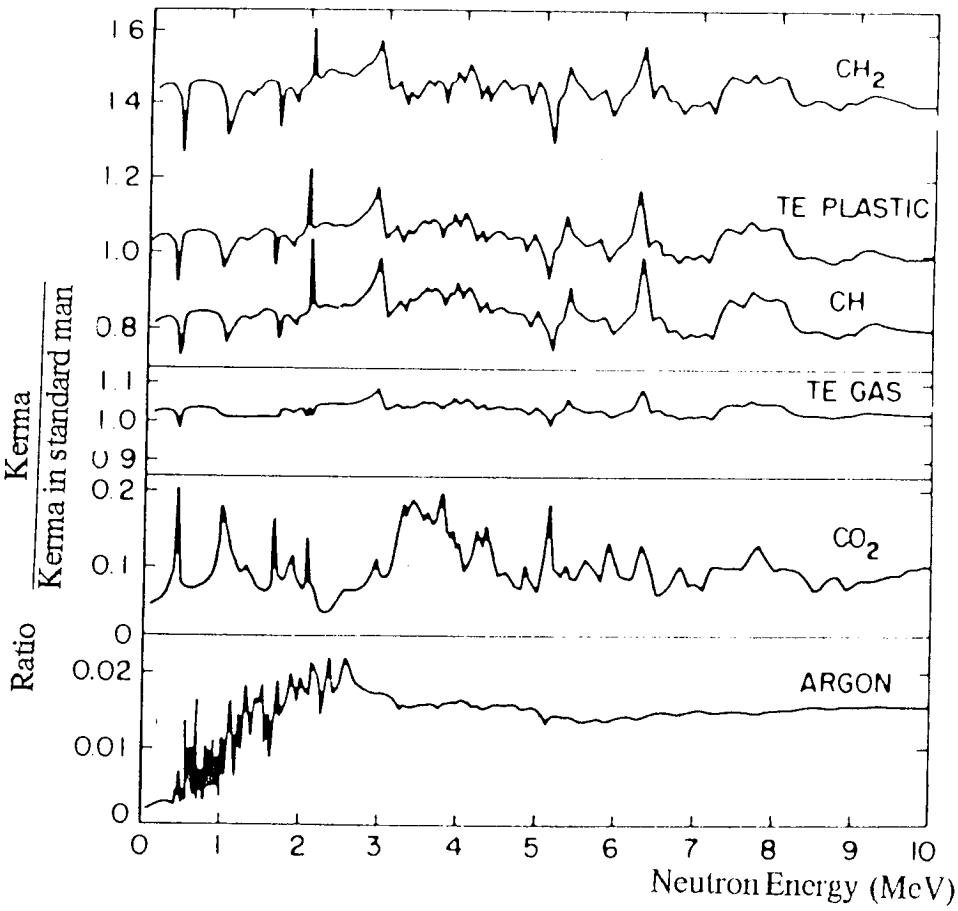

.Figure 1.1 Ratios of kerma in material to kerma in standard man, for argon, carbon dioxide, tissue-equivalent gas, acetylene (C_2H_2), tissue-equivalent plastic, and ethylene (C_2H_4) (Williamson and Mitacek, 1967).

In calculating the first collision dose rate from fast neutrons, i.e. for small volume of tissue, energy transfer is considered to be via elastic collisions with hydrogen nuclei only.

For calculation purposes, thermal neutron dose arises from the effects of [^{14}N (n,p) ^{14}C] and [^{1}H (n,γ) ^{2}H] reactions. The proton recoil nuclei from nitrogen reaction contributes 0.62 Mev of energy at the capture site, and the gamma producing reaction constitutes a source of 2.2 Mev / photon. Many of these photons escape from the mass of tissue even when as large as a human body phantom.

Since the 0.62 Mev proton emitted in the ^{14}N (n,p) ^{14}C reaction has a range in tissue of less than 10 μm, and because of the much greater range of the 2.2 Mev gamma from ^{1}H (n,γ) ^{2}H reaction, the major fraction of energy absorbed in small samples of tissue is due to the ^{14}N (n,p) ^{14}C reaction. The dose rate can be calculated using equation 1.3.

The following parameters are of value:

Hydrogen density of soft tissue = 6.26×10^{22} nuclei. cm^{-3}.

Nitrogen density of soft tissue = 1.33×10^{21} nuclei. cm^{-3}.

CHAPTER TWO: THE MEASUREMENT OF ABSORBED DOSE

This chapter provides a description of radiation detectors used in the measurement of gamma or neutron tissue dose over a wide range of dose rates. The characteristics described here were considered by the author when deciding upon the detector system to be used in the experimental work that follows.

For reasons described in Chapter 3, a typical scintillator system was chosen. An outline of the characteristics of such a detector is provided in Section 2.3 and further details given in Chapter 3.

2.1 Ionization Chambers:

Absorbed dose due to neutrons, may be determined accurately and conveniently with ionization cavities employing the Bragg-Gray relation.

Gray and Read (1939) and Rossi and Failla (1956) have described the use of tissue equivalent ionization chambers for neutron dosimetry. The important elements contributing to neutron and gamma ray absorption in tissue are incorporated into the chamber wall and gas. In this way the ionization produced in the gas volume may be directly related to the absorbed dose in tissue, when allowances are made for small differences in the value of the average energy to produce an ion pair in the gas, W. When a tissue equivalent chamber is exposed to one roentgen of gamma or hard X-rays, the corresponding absorbed dose is 9.7×10^{-3} Gy.

When a gas cavity is introduced into a medium irradiated by neutrons, the energy deposited per unit mass E_m, in the wall of the ionization chamber, is given by : $E_m = {}^{'}S_m \, W \, J_m$, where J_m is the ionization per unit mass of gas and ${}^{'}S_m$ is the mass stopping power ratio averaged over the spectrum of charged particles crossing the cavity. Generally homogeneous ionization chambers are employed and hence the mass stopping power ratio will be unity.

The ionization produced in the chamber when irradiated with neutrons will be equal to $(W_p / W_e) \times 9.7 \times 10^{-3}$ Gy. The ratio W values will depend slightly upon the gas mixtures in the chamber but will usually lie in the range of 1.03 to 1.06 (I.T. Myres 1968) - Table 2.1.

The ratios of kerma in tissue equivalent plastic and tissue equivalent gas to that of standard man, as computed by Williamson and Melacek 1967, were given in Figure 1.1 for neutron energies from 0.1 to 10 Mev. Ratios for other materials used in dosimetry, mainly argon, carbon dioxide, acetylene and ethylene are included.

Ionization chambers lined with carbon or filled with carbon dioxide (Rossi and Rosenberg, 1955) may be expected to yield a good measure of the absorbed dose delivered to tissue by electro magnetic radiations, while being rather insensitive to neutrons (due to the higher atomic number).

The values of the neutron sensitivity (K) of these devices are given in (NCRP Report 1961 - Table 193).

Gas	x-rays or γ-rays w_e (ev)	w_α (ev)	w_p (ev)
Air	33.73 ± 0.15	34.98 ± 0.05	36.0 ± 0.4
Argon	26.20 ± 0.2	26.30 ± 0.1	26.4 ± 0.8
Neon	36.20 ± 0.4	35.70 ± 2.6	28.6 ± 8.0
Nitrogen	34.60 ± 0.3	36.39 ± 0.04	36.6 ± 0.5
Oxygen	31.80 ± 0.3	32.30 ± 0.1	35.5 ± 2.0

Table 2.1: Summary of average (w) values for different gases (I.T. Myres, 1968)

2.2 Proportional Counters:

A proportional counter may be used as a dosimeter for gamma rays in the presence of neutrons, by pulse height integration of the small pulses due to gamma rays, and rejection of the large pulses due to neutrons (Caswell et.al,1963). The instruments consists of a graphite wall, He-CO_2 filled proportional counter operated at low gas pressure (2-10 Cm Hg). Large pulses due to heavy particle recoils, such as carbon recoils from the walls, and carbon and oxygen recoils from the gas, are discarded. Small secondary electron pulses are recorded and their heights are integrated. Discrimination between neutrons and gamma rays is obtained at or below pressures where the range of the carbon recoils is approximately the length of the sensitive volume of the chamber. Gamma ray response per roentgen is independent of energy to within 5% from 200 Kev to 1.25 Mev, and within 20% down to 47 Kev.

The use of graphite lining and a thin aluminium wall minimises production of gamma rays in the walls by inelastic scattering of incident neutrons. This type of instrument has relatively high sensitivity and is, therefore, of use at gamma ray exposure rates below 10^{-2} R min^{-1}. Proportional counters may be used to advantage in measuring fast neutron dose in the presence of gamma rays (Hurst 1954). This approach is opposite to that of the use of proportional counter for gamma ray dosimetry. The Bragg-Gray cavity principle applied, for example, to ethylene gas and polyethylene liners is satisfactory for fast neutrons, since the ratio of energy deposited per gram of ethylene to energy dissipated per gram of tissue is substantially independent of neutron energy. The essential departure from the ionization chamber technique is that the number of ion pairs

produced in the gas is determined by summation of pulse heights, rather than integration of charge or current measurements. This enables the integration of the pulses due to neutrons, while rejecting those due to γ-rays, if the dimensions of the gas cavity and the pressure of the gas are chosen so that the pulses due to electrons (from γ-ray effects) are generally smaller than those of the pulses due to recoil protons (from fast neutron collision). If the pulse height is proportional to the number of ion pairs produced, this method is every way equivalent to the ionization chamber, with the added advantage of being quite insensitive to gamma radiation.

2.3 Organic Scintillators:

The deposition of energy from neutron interactions with organic phosphors is similar to that in tissue. Hence, the kerma dose (J kg^{-1}), measured by observing the proton energy spectrum obtained from organic phosphors, can be expressed in terms of tissue dose. Pulses produced by proton recoils in the scintillator are recorded on a multichannel analyser for data analysis. Correction factors must be applied for non linear light output with proton energy. The differential proton energy spectrum can, in turn, be converted to a total absorbed dose, expressed in grays or sieverts per incident fast neutrons per square centimetre.

The process is simplest for gamma-rays since the response is linear with Compton electron energy, and the detector is a near tissue equivalent material.

Organic scintillators possess several advantages which make them particularly suitable

for a wide range of applications:

a) The liquid or plastic material permits great flexibility in the size and shape of the radiation detector element.

b) The density and the low atomic number of the constituent elements minimises the errors due to electron back-scattering encountered with heavier scintillators.

c) The linear scintillation response to electrons of less than 125 kev makes them suitable for β-ray spectrometry down to a few kev.

d) The high hydrogen content of organic scintillators allows them to be used for fast neutron detection and spectrometry, by observation of the recoil protons within the material.

e) The dependence of pulse shape on $\frac{dE}{dx}$ in many organic scintillators permits the use of pulse shape discrimination techniques for distinguishing scintillations due to fast neutrons (recoil protons) from those due to γ-rays (Compton electrons).

f) The low density and low atomic number of the constituent elements are an advantage for fast neutron spectrometry, but less suitable for X-ray or γ-ray spectrometry, but the efficiency can be increased by using a large scintillator volume. However, organic scintillators are still useful for gamma dose measurements, since such scintillators contain mainly carbon and hydrogen, and are similar in composition to water, the main component of soft tissue.

g) The reduced scintillation efficiency to heavy particles and the associated non-linear scintillation response to protons, deutrons, α-particles, etc., except at higher energies, limits the use of these detectors. However, calibration of the energy response allows organic scintillators to be used satisfactorily for heavy particles and fast neutron dosimetry.

A variety of scintillators can be used for the measurement of neutron and gamma doses.

Liquid Scintillators:

i) NE213 This xylene based scintillator is used primarily for neutron detection and particularly where gamma background is a problem. NE213 exhibits good pulse-shape discrimination properties. It exhibits a light-output of 78% that of anthracene with decay constant of 3.7 n.s. Further details of the characteristics of this scintillator and its use within a detector system are given in Chapter 3.

ii) NE226 Is based on hexafluorobenzene and is virtually hydrogen free. It is, therefore, transparent to neutrons and very useful for detection of gamma radiation in the presence of fast neutron fluxes.

iii) NE314A This scintillator type is loaded with 75% lead in order to improve the detection of low energy gamma or X radiations.

Plastic Scintillators:

i) NE102A Has an excellent balance of properties, high light-output of 65% of anthracene, a fast decay time (2.4 n.s) and good light-transmission (2.5 metres). It is suitable for fast neutron dosimetry.

ii) NE105 is recommended primarily for use in radiation dosimetry and has applications in the field of low energy X-ray measurements. It is a clear homogeneous

scintillator with no after glow, and has a more linear energy response than an air equivalent scintillator with incorporated ZnS (Ag).

iii) NE125 This new plastic scintillator was developed specially for neutron investigations and is based on a fully deuterated system. (D = 13.8%, H = 0.26%, C = 85.9%). It has a light output of 55% of anthracene and a decay time of 2.7 n.s.

Glass Scintillators:

Glass scintillators are particularly noteworthy for their chemical resistance to nearly all organic and inorganic reagents, except hydrofluoric acid. The high melting point and excellent physical characteristics of these glasses, together with their chemical resistance, permits their use under extreme environmental conditions, where measurements with other scintillating materials would not be possible. However, they have the disadvantages of a decay constant approximately 200 times higher than organic scintillators, and light output is low.

i) NE912 (7.7% lithium enriched in ^{6}Li to 95%) and NE913 (83% lithium depleted in 99.99% ^{7}Li) are useful for gamma and neutron detection, NE912 for neutrons (insensitive to gamma, γ electrons or X-rays) and NE913 for detection of electrons, gamma or X-rays (insensitive to neutrons).

ii) NE451 This detector is used for fast neutron detection. It employs a clear homogeneous plastic as a moderator and uses Zns (Ag) phosphor. Light collection is

improved by using cylindrical light guides and an integrally mounted reflector. It shows a maximum emission at 450 n.m. and a decay constant of 2×10^{-7} s.

iii) NE422 Is used for efficient detection of thermal neutrons in the presence of gamma radiation. It employs a lithium compound whose lithium content is enriched to 95% ^{6}Li dispersed in a Zns (Ag) matrix. Efficient measurement of thermal neutron fluxes is possible in the presence of gamma radiation field as high as 10^{7} gamma rays per neutron.

2.4 Neutron REM Counters:

The term rem counter is normally used for a neutron measuring instrument whose sensitivity is assumed to be proportional to the maximum dose rate equivalent in the human body.

All existing rem-counters have three factors in common:

i) They are filled with at least one thermal neutron detector. The reactions mainly used are ^{10}B (n,α) in a BF_3 proportional counter or ^{6}Li (n,α) in a LiI scintillator.

ii) The detector is always surrounded by a moderator material, usually polyethylene or paraffin wax.

iii) They are fairly heavy with most weighing over 6 kg.

In each case the basic principle is that the moderator surrounding the thermal neutron detectors is designed with suitable dimensions or additional absorbers, such that the

response probability of the neutron measuring equipment over the entire energy range of interest is, as far as possible, proportional to the dose equivalent (DE).

Rem counters can be classified as follows:

a) Rem-counters without internal absorbers. A common used instrument consists of LiI (Eu) crystal with light guide and photomultiplier. The crystal is mounted in the middle of a polyethylene moderator sphere (simple sphere rem-counter). (Hankins, 1962).

b) Rem-counters with internal absorbers. The instrument often contains a BF_3 counter in the central axis of a polyethylene cylinder. A boron containing intermediate absorber is located at a certain distance from the detector (Anderson and Brawn, 1962).

c) Another cylindrical type is based on the long counter. A spherical version contains a LiI (Eu) crystal with light guide and photomultiplier. At a certain distance from the crystal there is a cadmium dome containing a hole through which the crystal and light guide are inserted.

d) Multisphere rem-counter. Various moderator spheres are used in conjunction with the scintillator counter (McGuire 1966).

e) Multidetector rem-counter. Several detectors and one moderator are used instead of one detector with different moderators, e.g. a BF_3 counter fitted in the central axis of the polyethylene cylinder, with three other detectors parallel to it and at a certain distance apart (H.Tatsuta 1967).

f) An 8-bit microprocessor kerma rate-meter system has been developed by (J.L. Silberberg 1977). It incorporates a stilbene scintillator and is capable of measuring and displaying neutron energy spectra and neutron kerma. The dedicated microcomputer allows on-site analysis of data. A pulse height distribution can be analysed in less than one second to yield results that are within 1% values determined from the same data by a large computer system. Tissue kerma rate is calculated from the energy spectra and displayed in rads per hour.

In practice these rem-counters are usually calibrated with Po-Be, Ra-Be, Am-Be or Pu-Be neutron sources after a suitable discrimination threshold has been set.

In types (a) and (b) the indicator of the reading device is given directly in m rem h^{-1} and the devices are used for energy ranges between thermal and 7-10 Mev. In type (f), the portable microcomputer displays directly the kerma in rads per hour in the energy range of 0.2 to 20 Mev.

For multisphere rem-metry type (d), the dose equivalent rate (DE) is obtained from the equation $(DE) = k \Sigma_i F_i C_i$, where k is a proportional factor, F_i are weighting factors, and C_i counting rates with various sphere diameters, i.
The dose equivalent rate is obtained in the thermal energy range up to 50 Mev (D. Nachtigal 1967).

With multidetector rem-counters type (e), the dose equivalent rate is obtained in a similar way. For example, in the case of a cylindrical type with BF_3 counter, the dose equivalent rate (DE) is given by:

$$(DE) = (1.15\ N_1 - 0.0639\ N_2) \times 10^{-2}\ m\ rem\ h^{-1}$$

where N_1 is the counting rate of the central BF_3 counter and N_2 is the sum of the counting rates of the three BF_3 counters.

The common features of the multisphere and multidetector type is that any change in the quality factor for neutrons, and hence any change in the dose equivalent, can be allowed for by altering the moderator diameters, the position of the detector and/or the weighting factors.

2.5 Thermo-Luminescent Dosimetry:

Irradiation produces ion pairs in an insulating material. Some of these may be trapped by impurities in the crystal and require heating to release them. On heating, visible light is given out, the total light released being proportional to the dose received. A suitable material which stores the energy for long periods without significant loss and which has a good light output is calcium fluoride, containing about 3% manganese Ca_2F (Mn).

Thermoluminescent dosimeters posses several desirable characteristics, including small size, high sensitivity, wide dose range and good stability under varying conditions.

LIF (TLD) phosphor is the most useful radiation dosimeter of near tissue equivalent material, and of material chemically stable to acids, alkalis, organic solvents and water vapour. However, these types are not convenient for measuring low doses (≤ 0.1 mSv). At present, $Mg_2\ SO_4$ (T_b), $CaSO_4$ (T_m), $CaSO_4$ (DY) and CaF_2 (DY) have high

sensitive response to low doses, but they have a large effective atomic number and the sensitivity has to be calibrated.

The response of the Li7F (TLD) dosimeter (99.99% Li7) to fast neutrons has been investigated by Wingate et al (1965) from 0.25 Mev to 14 Mev neutron energy. A newly highly sensitive phosphor LiF (TLD) dosimeter has been designed by (Y. Furruta and S. Tanaka 1972) doped with three types of impurities Cu, Mg, P or Si, and can be used for low dose measurement of gamma and neutrons. The sensitivity has increased to about 23 times higher than Li7 (TL600).

CaF_2 (Mn) and LiF are the most widely used reliable dosimeters (Ginther and Kirk 1956,57 and Cameron and Defronceshi 1967).

CaF_2 (Mn) must be enclosed in an evaluated or inert gas-filled envelope to avoid generation of spurious thermoluminescent signals. The phosphor can be cemented to an ohmic heater within the envelope. The thermoluminescence is measured by placing a device in front of a suitable photomultiplier and passing an electric current through the dosimeter heater element. Doses of the order of 10^{-6} Gy are detectable and the light output is proportional to the dose up to 3×10^3 Gy.

2.6 Chemical Dosimetry:

In chemical dosimetry, radiation dose is determined from the chemical changes produced in an appropriate medium.

Chemical dosimetry systems are used mainly for measuring high doses beyond the range where ionization chambers are normally used. These systems are also attractive because

they consist of an aqueous solution, which is enclosed in a suitable container, and approximates rather closely the atomic composition and density of many biological materials.

The desirable characteristics of any chemical dosimeter are:

a) sensitivity

b) adequate reproducibility

c) stability before and after irradiation

d) dose-rate independence

e) temperature independence

f) independence from the quality of radiation (LET)

g) linear relation between reaction product and dose, and

h) simple preparation and analysis.

Ferrous sulphate systems (Frickle dosimeters) are among a wide variety of systems used today. The Frickle dosimeter atomic composition and density are close to biological systems of interest. The range of this dosimeter is from 40 - 400 Gy. The dosimeter consists of an aerated dilute solution of ferrous sulphate in 0.8 N sulphuric acid (3.832% H_2SO_4, 96.168% H_2O). This concentration was initially selected to match the mass absorption coefficient for X-rays in air.

If the radiation chemical yield is assumed to be a linear function of the absorbed dose then:

$$G(x) = \frac{\Delta n}{\Delta E} \times 100$$

where G(x) is the radiation chemical yield expressed in terms of the number of molecules or radicals formed per 100 ev of absorbed energy; Δn is the number of molecules of x formed per unit volume; and ΔE is the amount of energy (in ev) absorbed per unit volume.

If G(x) is known (refered to as G. value), the absorbed energy (expressed in electron volt per unit volume) is given by (G.G.Eicholz and J.W.Poston 1979).

$$\Delta E = \frac{\Delta n \times 100}{G(x)}$$

If the concentration of x is expressed in moles/litre (M), then

$$\Delta E = \frac{(\Delta M)\ (6.023 \times 10^{25})}{G(x)}$$

Where the absorbed energy is in electron volt per litre (evL^{-1}) and using the conversion that 1 rad equals 100 ergs g^{-1} and 1 ev = 1.602×10^{-12} ergs, the absorbed dose can be obtained:

$$D_{ab} = \frac{(\Delta M) \times 6.02 \times 10^{25} \times 10^{-3} \times 1.602 \times 10^{-12} \times 10^{-2}}{G(x)\rho}$$

$$D_{ab} = \frac{(\Delta M) \times 9.64 \times 10^{8}}{G(x)\rho} \text{ rad} = \Delta M \frac{(9.64 \times 10^{6})}{G(x)\rho} G_y \qquad \text{.....(2.1)}$$

Where $\rho(kgm^{-3})$ is the density of the irradiated system.

The above relation (2.1) may be applied to any type of radiation, where G(x) must be measured for each radiation to which the particular system is to be applied.

CHAPTER THREE : A LIQUID SCINTILLATOR SYSTEM FOR MIXED GAMMA-NEUTRON DOSE MEASUREMENTS

The liquid scintillator NE213 has been chosen for this work, mainly for its fast response, where detection of neutrons by means of proton-recoil scintillations require fast signals for time measurements. Its usefulness is limited largely to the energy range above 300 keV. Below that, photomultiplier tube noise is a serious problem. The upper limit is the fast neutrons elastic scattering limit, which is the limit of isotropic scattering and, at 10 MeV, is the maximum neutron energy of the Am-Be source used in this work. NE213 also has the advantage of good timing resolution and a reasonable counting efficiency. The fast scintillation decay time enables the NE213 liquid scintillator to be used in conjunction with fast photomultipliers to provide scintillation counts with time resolution of less than 10^{-9} s. This high scintillation response, high quantum efficiency and the well matched spectral response with the S11 photocathode response, makes the NE213 preferable to all other scintillators and especially preferred to other organic scintillators for fast neutron detection and the use of pulse shape discrimination techniques.

3.1 Characteristics of the NE213 Detector System

Liquid scintillator NE213 can be used to measure gamma dose rates because of the similar radiation absorption characteristics to water - the main component of soft tissue in the body. The NE213 liquid scintillator used in this work has a carbon to hydrogen ratio of 1 : 1.123. In both scintillator and soft tissue, the electron band strength is much less than the energy of the gamma ray and, therefore, the atomic electrons are effectively free

electrons. In water there are 10 free or loosely bound electrons per molecule, while in NE213 there are 7 free electrons per molecule. The gamma ray exposure dose absorbed by such a scintillator can be considered similar to that absorbed by soft tissue of the body. Generally, only compton scattering of the incident γ-rays need to be considered, since, for hydrogen, photoelectric effect interactions are significant only for $E_c \leq 20$ keV and, for carbon ≤ 200 keV.

NE213 can also be used to measure neutron tissue dose. The high hydrogen content allows it to be used for fast neutron detection and spectrometry, by observation of the recoil protons within the material. However, reduced scintillation sensitivity to heavy particles and the associated non-linear response to protons, deutrons and alpha particles, except at higher energies, limits its use. Calibration of the energy response is required if the scintillator is to be used for fast neutron spectrometry.

Furthermore, the dependence of pulse shape on (dE/dx) and the fast time response of this scintillator permits the use of pulse shape discrimination techniques for distinguishing scintillation due to fast neutrons (recoil protons) from those due to γ-rays (Compton electrons). Hence, the NE213 scintillator can be used to measure gamma and neutron dose in a mixed radiation field. Table 3.1 gives some relevant data for the NE213 scintillator used for this work.

The NE213 scintillator must be optically coupled to a suitable photomultiplier. The photomultiplier used in the early part of this work was an S11 (9810B) equivalent of 56AVP type, and has the characteristics shown in Table 3.2

Hydrogen nuclear density N_H (cm^{-3})	0.048382×10^{24}
Carbon nuclear density N_C (cm^{-3})	0.03985×10^{24}
Electron density N_e (cm^{-3})	0.293×10^{24}
Hydrogen / carbon ratio	1.123:1
NE213 density ρ (gcm^{-3})	0.874
Mass number A	13.123
Mass of NE213 (kg)	4.393×10^{-2}
Dimension (mm)	40 x 40

Table 3.1: Liquid Scintillator NE213 data

Wavelength range (nm)	320 - 650
Anode sensitivity (mA/watt)	5000
Rise time (ns)	2.2
Photomultiplier gain	6.7×10^7
Quantum efficiency (%)	20
Dark current (A/lumen)	min 20, max 200

Table 3.2: Photomultiplier type S11 data

The coupling efficiency between scintillator and photomultiplier is maximised by appropriate matching of the light emission of the scintillator and the spectral response of the photomultiplier. These are shown in Figure 3.1a & b.

The light output from the scintillator is converted to electrons and amplified by the use of the photomultiplier. A schematic diagram typical of the electronic amplification and data analysis system used in this work is shown in Figure 3.2 (The pulse shape discriminator included is further described in Section 3.4).

3.1.1 Spectrometer Linearity

The linearity of the spectrometer system used in this work was obtained from measured gamma ray spectra : ^{60}Co (E_γ = 1.17, 1.33 Mev), $^{137}C_s$ (E_γ = 0.66 Mev) and ^{22}Na (E_γ = 1.28, 0.511 Mev). A typical gamma spectrum is shown in Figure 3.3. The channel number corresponding to Compton edge is plotted against the Compton electron energy E_c in Figure 3.4 and illustrates the linearity of the spectrum from gamma rays. E_c is calculated from the gamma ray energy of the appropriate source by the equation:

$$E_c = E_\gamma / 1 + \frac{0.511}{2E_\gamma}$$

The scintillator light output is linear with electron energy. However, for neutron measurements, the measured proton recoil spectra must be corrected for non-linear scintillator light output with proton energy.

The relation between the scintillator light output and the energy of the recoil proton E_p

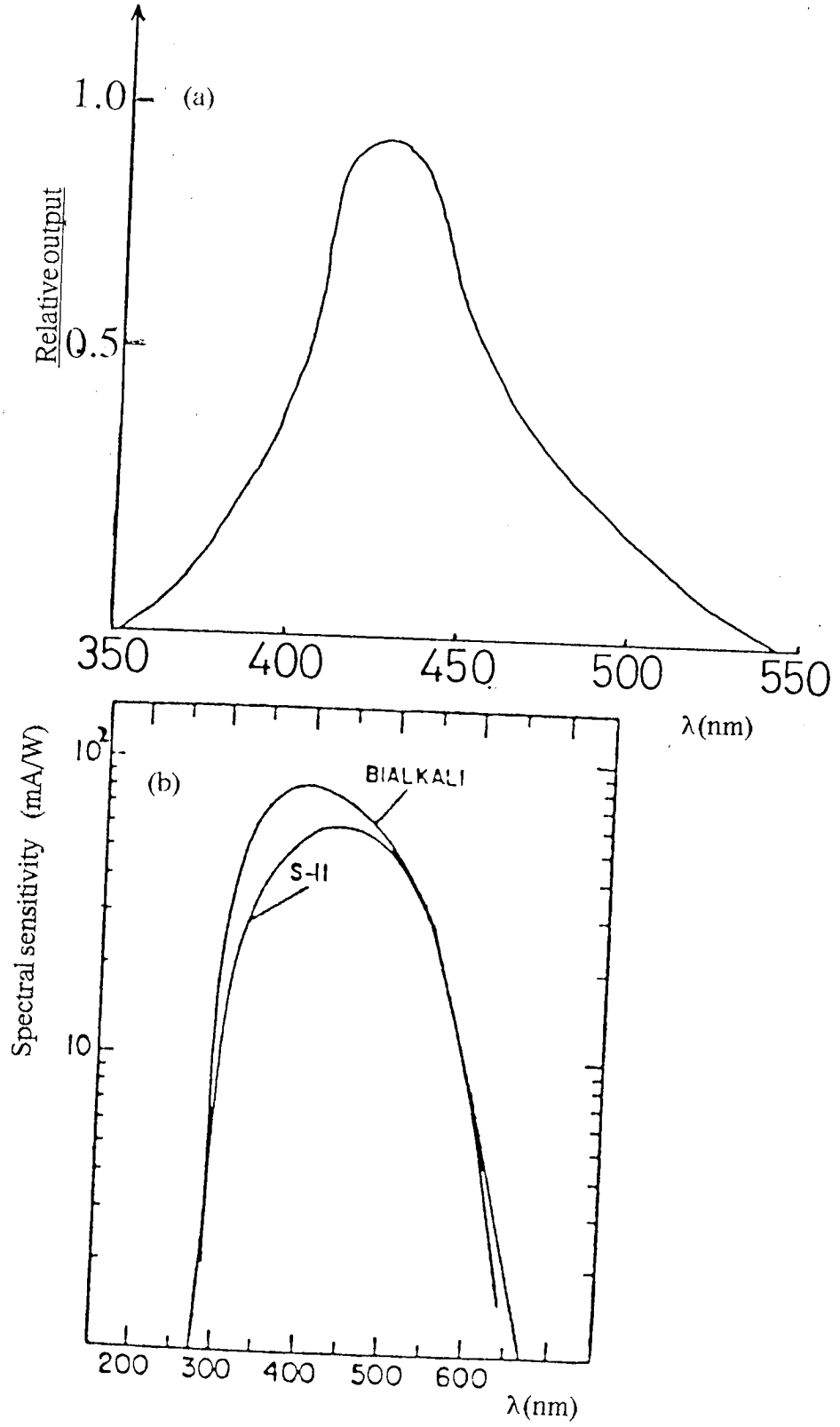

Figure 3.1 : (a) Light emission spectral response of NE213 liquid scintillator, (b) spectral response of S11 photomultiplier(Thorn EMI).

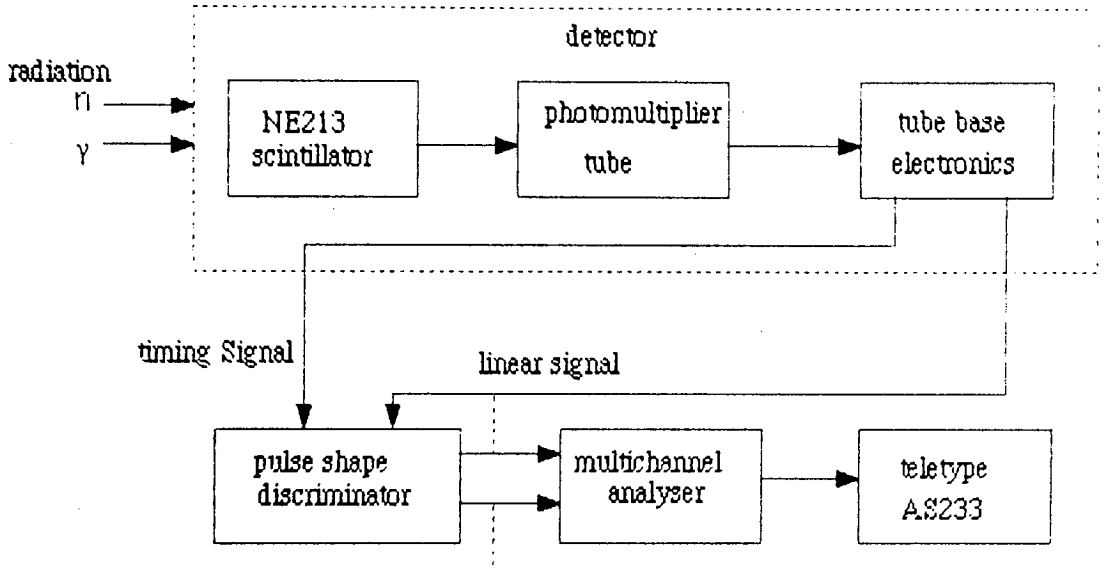

Figure 3.2 Schematic diagram of experimental data analysis system.

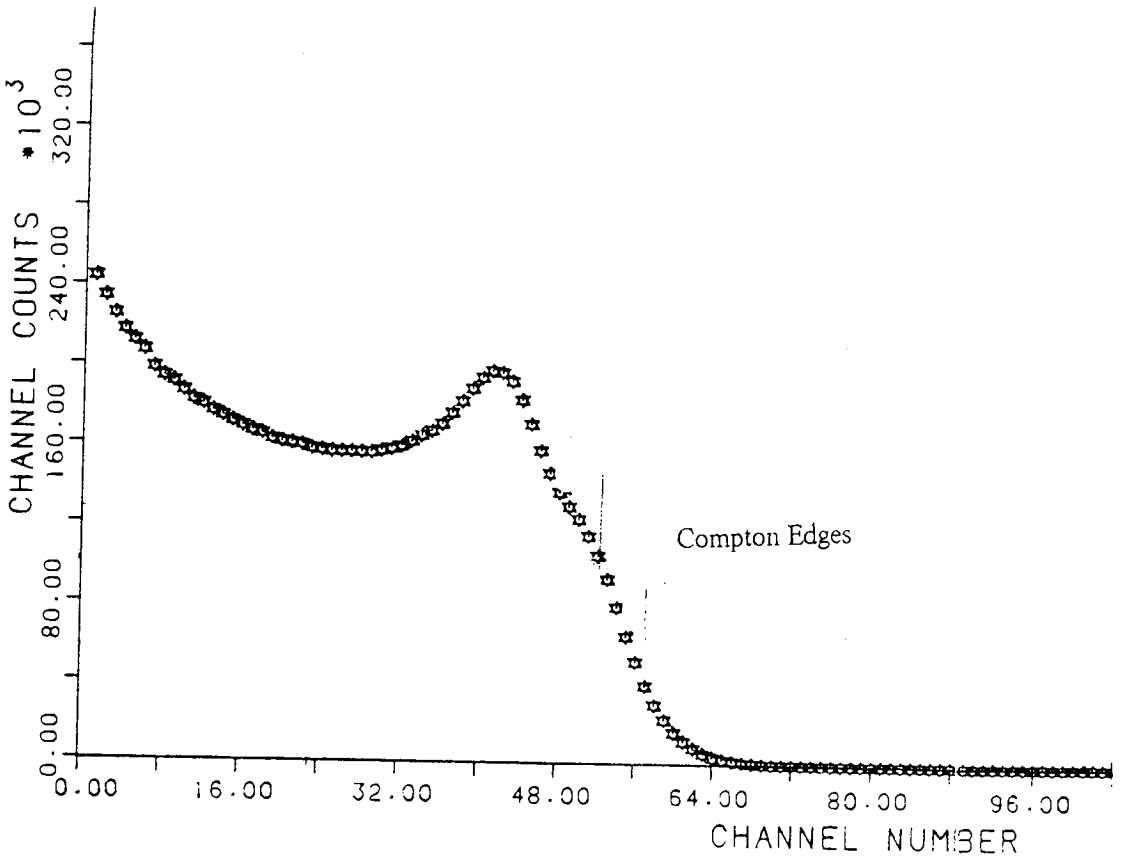

Figure 3.3 Gamma spectrum for ^{60}Co gamma ray source.

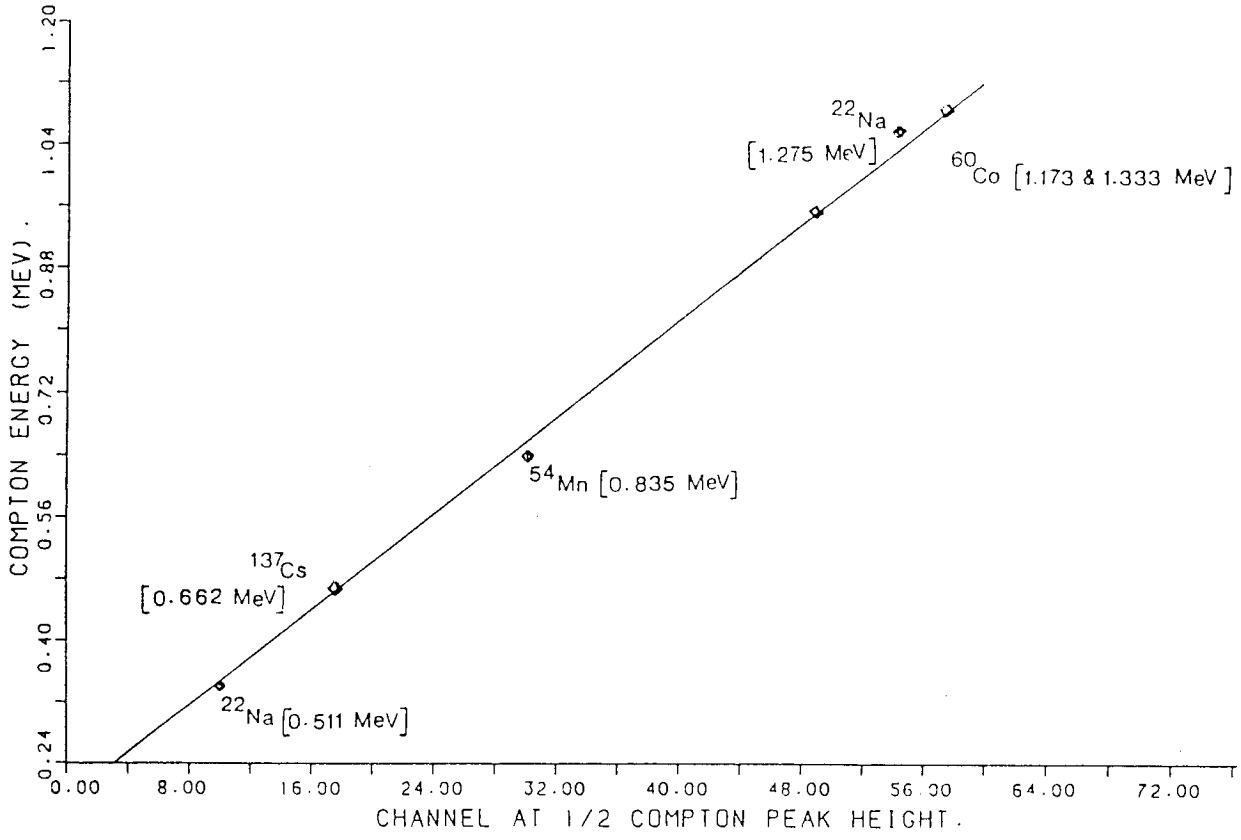

Figure 3.4 The linearity of the spectrometer.

can be determined by relating the light output to the equivalent electron energy E_e (J.B.Marion and J.L.Fowler, 1960).

$E_p \equiv 1.78 (E_e + 1.1)$ for $E_e > 1.85$ Mev

$E_p \equiv E_e$ for $E_e = 1.85$ Mev

$E_p \equiv 3.48 E_e$ for $E_e < 1.85$ Mev.

Figure 3.5 indicates the relationship between the equivalent electron energy and recoil proton energy.

3.2 Measurement of Gamma Dose Rate

A light pulse originates in the scintillator from the excitation of molecules by the Compton scattered electrons and the total energy deposited in the scintillator is proportional to the absorbed dose. The conversion of the scintillator output spectrum into a measure of absorbed dose is achieved by summation over the measured spectrum.
A computer program was written for this purpose and is listed in Appendix A. The product of C_i, the number of counts in channel i, and E_i (Mev), the energy of the channel i, is summed over the spectrum. An expression is obtained for the energy deposited in time T(s) over which the spectrum is accumulated.

The total rate of energy deposited in scintillator is equal to

$$\Sigma (C_i E_i) \times \frac{1.6 \times 10^{-13}}{T} \ J\ s^{-1}$$

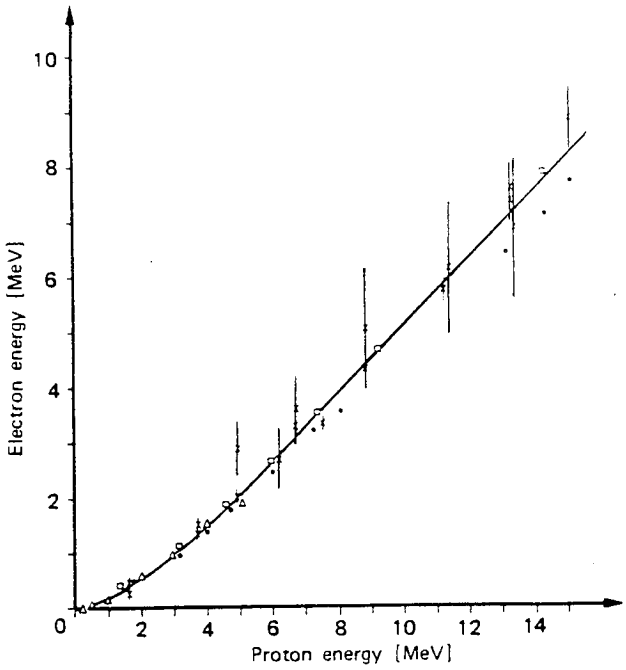

Figure 3.5 The light output (expressed in equivalent electron energy deposition) versus proton energy for liquid scintillator NE213 (From Nair and Mitschke).

Hence, if the above expression is divided by the mass of the scintillator M (kg), an expression for the absorbed dose rate is obtained, i.e.

$$\frac{1}{MT} \Sigma (C_i E_i) \times 5.76 \times 10^{-10} \text{ J kg}^{-1} \text{ h}^{-1}$$

The energy of each channel can be calculated from the equation $\Delta E_c / \Delta I_c$ where E_c (Mev) is the maximum Compton energy and I_c is the corresponding channel number of the Compton edge. Therefore, the expression for absorbed dose can be written as :

$$\frac{\Delta E_i}{MT} \times 5.76 \times 10^{-4} \Sigma (C_i I_i) \mu \text{ Gyh}^{-1} \quad \ldots\ldots\ldots\ldots \quad 3.1$$

where I_i represents the channel numbers corresponding to E_i.

A Cobalt 60 Source giving a known exposure dose was used to check the accuracy of the system, when used to measure absorbed dose rate. The Cobalt 60 Source had been purchased from Radio-Chemical Centre, Amersham, providing, on the 11th July 1978, an exposure dose of (6.97 ± 0.35) mRh^{-1} at 1m.

The absorbed dose at particular distances can be calculated using the known ^{60}Co half life of 5.28 years. These calculated values are presented in Table 3.3, alongside experimentally measured dose rates, but are subject to several correction and uncertainty factors (Table 3.4).

Position (m)	Calculated dose rate μGyh^{-1}	Measured dose rate μGyh^{-1}
1.00	30.40	26.03
0.707	61.40	51.30
0.50	121.60	101.10
0.35	248.10	193.50
0.25	486.40	375.80

Table 3.3: Uncorrected calculated and measured dose rates for ^{60}Co gamma source (15th July, 1984).

Position (m)	Source strength uncertainty μGyh-1	Attenuation factor	Source detector position uncertainty μGyh-1	Standard deviation of measurement μGyh-1	Background correction μGyh-1
1.00	± 1.5	1.12	± 0.15	± 0.13	0.7
0.707	± 3	1.12	± 0.4	± 0.5	0.7
0.50	± 6	1.12	± 1.2	± 1.3	0.7
0.35	± 12.4	1.12	± 3.6	± 3.5	0.7
0.25	± 24.4	1.12	± 9.7	± 9.4	0.7

Table 3.4 : Correction and uncertainty factors for calculated and experimental results

(i) Background dose rate:

The background correction was measured at 0.7 μ Svh^{-1}

(ii) Attenuation factor:

The experimental results listed in Table 3.3 do not take into account gamma-ray attenuation through the scintillator. If the exponential attenuation of the gamma rays as they pass through the detector, is taken into account, then the probability of Compton scattering will decrease along the length of the scintillator and, therefore, a correction must be made for this decrease in the probability of Compton scattering.

The fraction change in gamma intensity is given by $1- e^{-\mu t}$ where μ is the linear attenuation coefficient and t is the distance into the scintillator cell. The gamma interaction rate per unit area per unit gamma flux within the scintillator is μt. Hence, the results for measured dose rate should be corrected by a factor : $\mu t / 1- e^{-\mu t}$. The correction factor to be applied to the results presented in Table 3.3 was calculated for NE213 at 1.25 Mev, the average gamma ray energy for ^{60}Co, μ = Ne σ, where σ is obtained at 1.25 Mev from E.Tochlin and B.W.Shumway, 1969. Using the data given in Table 3.1, this gives a correction factor:

$$\frac{\mu t}{1- e^{-\mu t}} \simeq 1.12.$$

(iii) Uncertainty in positioning of the source:

The maximum uncertainty due to the positioning of the source relative to the centre of the scintillator was estimated to be $\pm$ 0.5 cm.

(iv) Statistical uncertainty in the measured count rate:

For a single measurement, the uncertainty in the measured count rate will be proportional to the square root of the count rate.

(v) Uncertainty in the source strength:

A ± 5% uncertainty attached to the source strength when supplied by the Radio-Chemical Centre, Amersham.

Table 3.5 presents the corrected calculated and experimental dose rates. The difference between experimental and calculated results can be attributed to the perturbation of the gamma field by the detector, particularly at distances close to the source.

Position (m)	Calculated dose rate μGyh^{-1}	Measured dose rate μGyh^{-1}
1.0	30.4 ± 1.5	28.37 ± 0.3
0.707	61.4 ± 3.1	56.70 ± 0.9
0.5	121.6 ± 6.1	112.40 ± 2.5
0.35	248.1 ± 12.4	216.00 ± 7.1
0.25	486.4 ± 24.4	420.20 ± 19.1

Table 3.5: Corrected, calculated and measured dose rates for ^{60}Co gamma source

3.3 Measurement of Neutron and Gamma Dose Rates in Mixed Radiation Fields

Some general characteristics of radioisotopes used to produce Be(α,n) neutron sources are given in Table 3.6 (E. Tochlin and B.W.Shunway, 1969). The ^{241}Am - Be Source used in this work has an extended neutron energy spectrum up to 10 Mev. Predicted neutron and gamma spectra are shown in Figure 3.6.

Experimental neutron (proton recoil) spectrum were separated from gamma spectrum (electron recoil) using a pulse shape discrimination system*, Figure 3.7 a,b. It is possible to discriminate between different radiations provided the detector produces a variation in the signal shape from these radiations. The principle of the operation is based upon the comparison of the two weighted time integrals of the detector signal.

* Link Systems, High Wycome, England.

Radioisotope	Half life	Specific activity C_i/ gm	α-particle energy (Mev)	Neutron yield $ns^{-1} \times 10^6$ per Curie	γ-ray exposure rate per Curie $\mu G_y h^{-1}$(1m)
^{226}Ra	1600 yrs	0.988	4.8, 5.3, 5.5 6.0, 7.7	20	8350
^{210}Po	138.4 days	4.5×10^3	5.30	2.5	0.3
^{238}Pu	80 yrs	17.4	5.5, 5.46	2.7	~ 0.3
^{239}Pu	24,360 yrs	0.0617	5.15, 5.13, 5.10	2.2	~ 0.3
^{241}Am	458 yrs	3.23	5.48	2.7	~ 0.3

Table 3.6 Properties of some radioisotopes used to produce Be(α,n) neutron sources (E.Tochlin and B.W.Shumway, 1969)

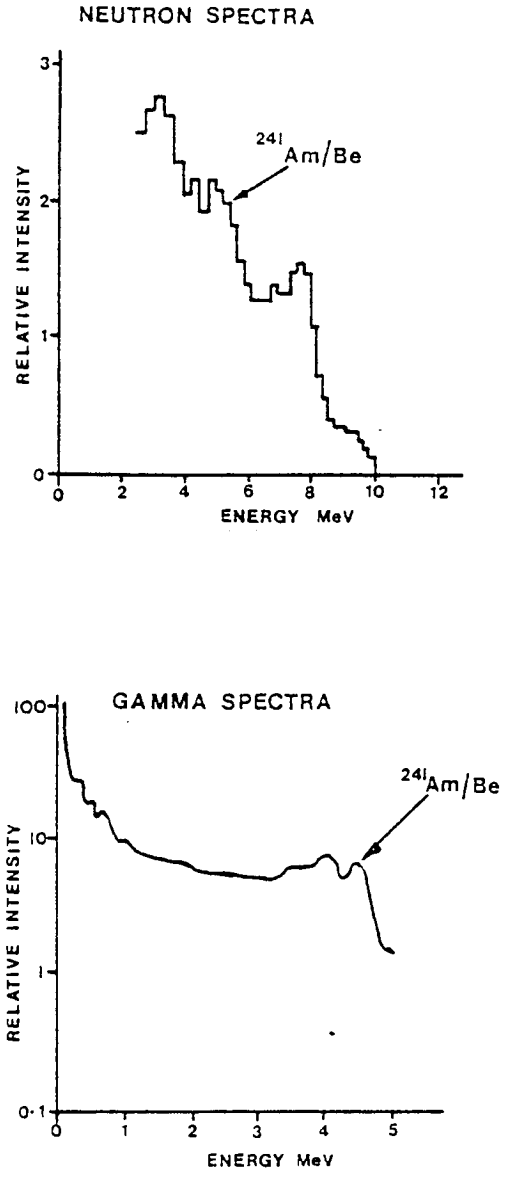

Figure 3.6 Neutron and gamma spectra from Am-Be source

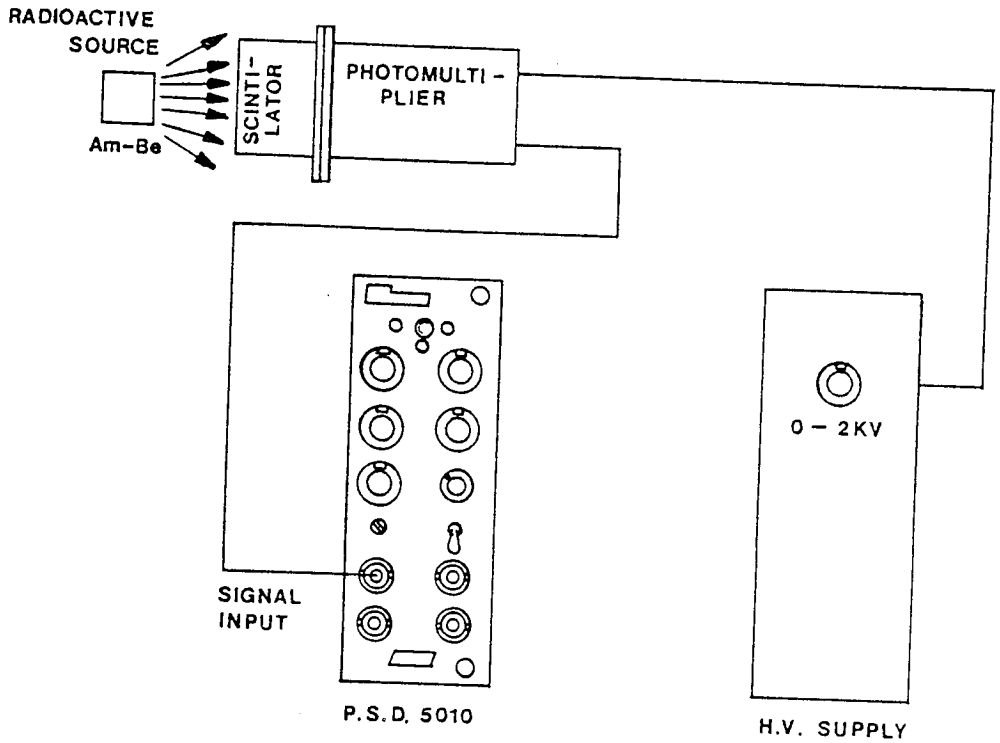

Figure 3.7a Neutron-gamma pulse shape discriminator arrangement

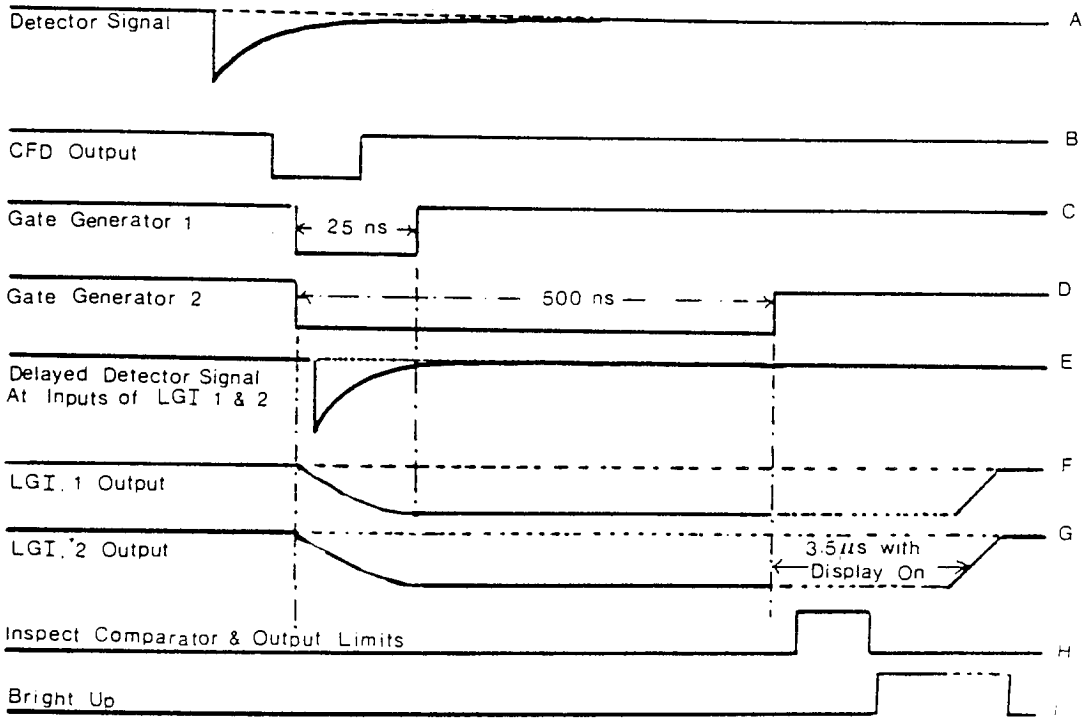

Figure 3.7b Linear gate and integrator waveforms

The radiation field interacts with the scintillator, which is optically coupled to the photomultiplier tube. The signals from the photomultiplier are fed into the signal input of the pulse shape discriminator, as shown in the schematic diagram, Figure 3.7a. The signals from the detector are delayed in a 30 ns delayed cable, and at the same time a buffer amplifier drives a start discriminator which 'enables' the constant fraction discriminator. The signal emerging from the enabling AND gate triggers the gate generators 1 and 2. The linear gate and integrators 1 and 2 integrates the input signal, for 25 ns and 500 ns, respectively. At the end of the longer of the two integrator time periods (gate 2), the control and sequence logic will perform the following operations:

(i) The state of the comparator is inspected to see whether the output of the linear gate and integrator LGI(1) is greater or less than the output of LGI(2). The result of this inspection determines whether the event is classed as a gamma or a neutron.

(ii) The upper and lower output discriminators are inspected and only those events falling between these limits are allowed to indicate an output pulse.

(iii) If an output signal occurs from the pile-up discriminator during the gate generator 2 period, the event is rejected and no output occurs.

(iv) The zero stabiliser oscillator triggers periodically if no detector signal is present. The stabilisers maintain the zero pedestal level of the integrators at a preset value.

(v) Bright up signals (z) are provided for the CRT display of the difference (y) and

total energy (x) outputs. All these basic waveforms are indicated in Figure 3.7b. The gate generator (1) duration is variable between 10 ns and 50 ns, and is normally set at 25 ns, which is well suited for plastic and liquid scintillators. The gate integrating capacitor is set to 82 pf, which is ideal for the scintillator used for this work. Similarly, the gate generator (2) duration is set at approximately 500 ns. The gate integrating capacitor is set to 180 pf, which is again ideal for stilbene and NE213. The delay line (25 cm), which is the 'clipping' line for the constant fraction discriminator, is selected for fast scintillators (stilbene, NE213, etc.), with a rise time of approximately 3-5 ns. This delay time would require lengthening if a 'slower' scintillator or other detector was being used. An analogue output is available on the front panel and can be fed into a multichannel analyser, which, when put into coincidence with either the neutron or gamma signal, will record the appropriate spectrum. When this feature is required the display ON/OFF switch must be on, in order to provide a 3.5 μs flat topped output signal.

A further computer program was used to analyse the experimental neutron spectrum data, typically those shown in Figure 3.8, and to calculate the dose rate. The program is listed in Appendix B. The measurement of neutron dose is similar to that for gamma dose (equation 3.1), where the gamma dose rate is equal to:

$$\frac{\Delta E_i}{MT} \times 5.76 \times 10^{-4} \Sigma (C_i I_i) \times Q F \, \mu Sv h^{-1} \quad (Q F = 1)$$

In the case of neutron dose, ΔE must be corrected for non-linear light output with proton energy, as described in Section 3.11.

The quality factor, computed from the ratio of dose equivalent (DE) and absorbed dose (D) values over the Am-Be neutron spectrum, has an average value of 7.4

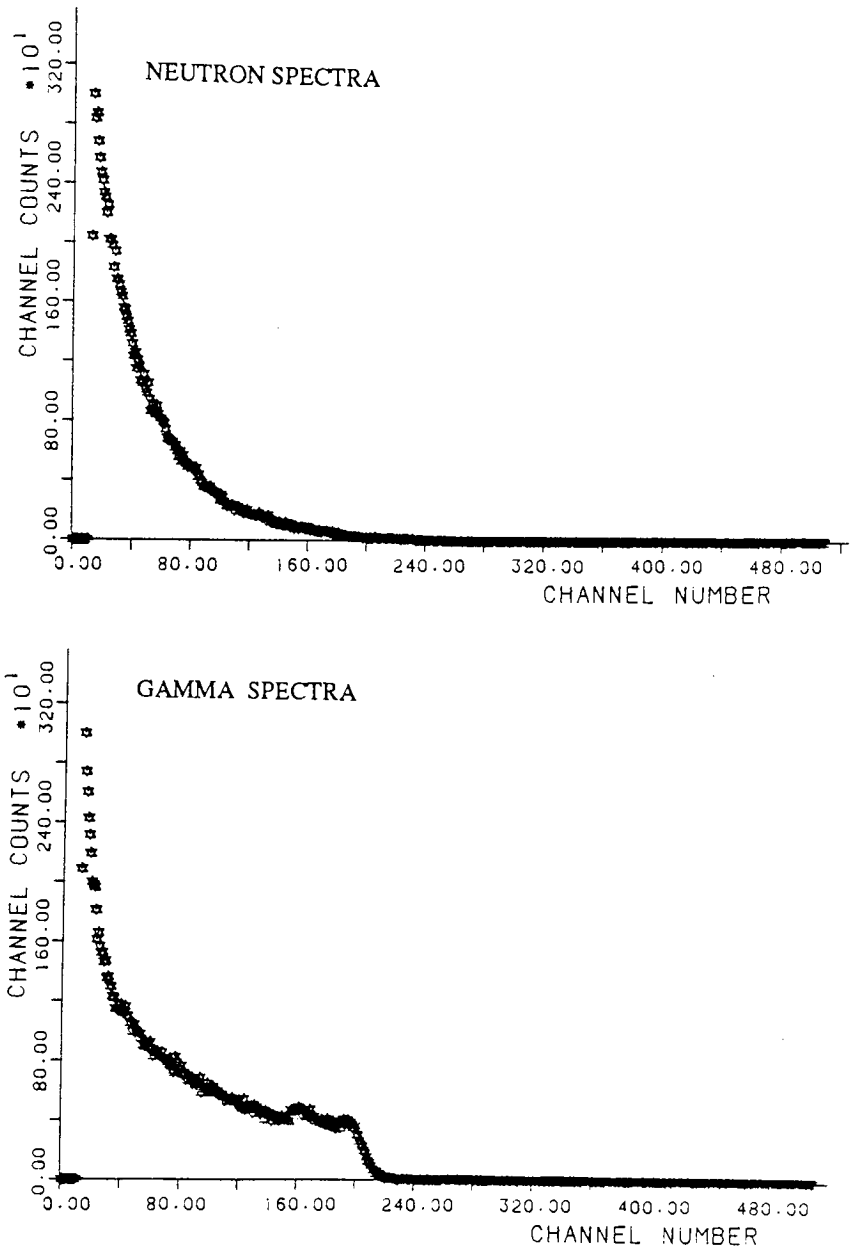

Figure 3.8 Neutron and gamma spectra for Am-Be source

(S.Pretre 1971, M. Fry 1966, E.Tochlin and B.W.Shumway 1969, D.Nachtigal 1967 and W.S.Snyder 1961).

The neutron dose rate can be calculated using the following formula of (National Bureau of Standard Handbook 63):

$$\text{Dose rate } (\mu G_y) = q \frac{S}{4\Pi r^2} \qquad \text{.....(3.2.)}$$

where:

S = Source strength ($n.s^{-1}$)

r = Distance from the source to point for which the dose rate is to be calculated (cm)

q = Dose per unit flux for neutrons of source energy (μG_y per unit neutron flux)

Table 3.7 gives the flux ($n.cm^{-2}\ s^{-1}$) for the two sources used, at different distances from the Am-Be source. The q values for the Am-Be source were taken from data given by M.Fry, 1966, which provides a kerma value (i.e. absorbed dose per unit neutron flux at the average neutron energy of 4.4. Mev. Using a value of $4 \pm 0.3 \times 10^{-5}$ μG_y per unit neutron flux, the dose rate in $\mu Sv h^{-1}$ will be equal to:

$$(4 \pm 0.3 \times 10^{-5}) \times 3.6 \times 10^{3} \times QF \times \phi\ (n.cm^{-2}\ s^{-1}).$$

The calculated dose rate from gamma radiation for the Am-Be source is obtained from equation 1.2. i.e.

Source (n. s^{-1})	Position (m)	ϕ (n. cm^{-2}. s^{-1})
Source 1:	0.3	66.4
7.5×10^5	0.5	23.9
	1.0	5.97
Source 2:	0.3	664.0
7.5×10^6	0.5	239.0
	1.0	59.7

Table 3.7 : The neutron flux (n. cm^{-2} s^{-1}) for the ^{241}Am-^{9}Be sources 1 and 2

$$\text{Dose rate} = 3.545 \times 10^{-7}\ \mu ea_{air} \frac{(\mu ea/\rho)_{med}}{(\mu ea/\rho)_{air}} \frac{BE}{r^2}\ \mu Svh^{-1}$$

$$= 1.377 \times 10^{-7} \frac{BE}{r^2}\ \mu Svh^{-1}$$

assuming QF = 1, $(\mu_{ea}/\rho)_{med} = 0.02\ cm^2\ g^{-1}$ at $E_\gamma = 4.43$ MeV

and $(\mu_{ea}/\rho)_{air} = 0.018\ cm^2\ g^{-1}$ at $E_\gamma = 4.43$ MeV (E.Tochlin, B.W.Shumway, 1969).

The gamma source strength is approximately equal to 2.8 times the neutron source strength from an Am-Be source (J.L. Silberberg 1978), giving values of 2.68×10^5 and 2.68×10^6 photons s^{-1}, respectively.

Table 3.8 gives the values of calculated and measured dose rates for both neutron and gamma fluxes ($E_\gamma = 4.43$ Mev) for the two Am-Be sources used for this work.

Source ($n.s^{-1}$)	Position (m)	Calculated neutron dose rate μSvh^{-1}	Measured neutron dose rate μSvh^{-1}	Calculated gamma dose rate μSvh^{-1}	Measured gamma dose rate μSvh^{-1}
Source 1:	0.3	70.75±5.3	41.80	1.811	1.72
$7.5x10^5$	0.5	25.46±1.9	15.20	0.652	0.59
	1.0	6.36±0.5	3.98	0.163	0.15
Source 2:	0.3	707.5±53	414.21	18.11	17.20
$7.5x10^6$	0.5	254.6±19	151.10	6.52	5.8
	1.0	63.6±5	36.70	1.63	1.49

Table 3.8: Calculated and measured dose rates for neutron and gamma fluxes

The correction and uncertainty factors presented in (Section 3.2) must again be applied. A further three corrections are needed:

(I) A small correction for carbon recoils must be considered. The cross section for carbon recoils is small compared with that for hydrogen recoil. This tissue correction factor can be calculated using equation 3.2, i.e.

Dose rate (μG_y) = $q \phi$, where ϕ is taken from Table 3.7 for the two Am-Be sources used and q (the absorbed dose per unit flux) from the National Bureau of Standard Handbook 63, giving an average value of $2x10^{-6}$ μG_y per unit flux in the energy range of 0.02 to 10 Mev. Table 3.9 gives the calculated neutron dose rate for carbon recoils.

(ii) A small correction is needed for thermal tissue dose rates due to the reaction ^{14}N (n,p)^{14}C and $^{1}H(n, \gamma)\,^{2}H$ is presented in Table 3.10. These reactions occur only in the neutron energy range from thermal to a few Mev. However, the contribution to the dose rates from these reactions was calculated using equation 3.2 and Table 3.6, in the energy range of thermal to 10 Mev. The average q value of 4.5×10^{-6} μG_y per unit neutron flux was given (National Bureau of Standard Handbook 63).

(iii) A correction is applied to the measured dose to allow for hydrogen composition of NE213 being different from that of tissue. The following data is used:

Tissue : $N_H = 6.26 \times 10^{22}$ particles cm^{-3}

NE213: $N_H = 4.822 \times 10^{22}$ particles cm^{-3}

Source ($n.s.^{-1}$)	Position (m)	Calculated neutron dose rate for carbon recoils $\mu Sv h^{-1}$
Source 1 :	0.3	3.53
7.5×10^5	0.5	1. 273
	1.0	0.318
Source 2 :	0.3	35.3
7.5×10^6	0.5	12.73
	1.0	3.18

Table 3.9 : Calculated neutron dose rate for carbon recoils for Am-Be source1 and 2

Source ($n.s^{-1}$)	Position (m)	Calculated thermal neutron dose rate μSvh^{-1}
Source 1 :	0.3	7.96
7.5×10^5	0.5	2.86
	1.0	0.72
Source 2:	0.3	79.6
7.5×10^6	0.5	28.6
	1.0	7.2

Table 3.10 Calculated thermal neurton dose rate for

[($^1H(n,\gamma)^2H$ and $^{14}N(n,p)^{14}C$)] for Am-Be source 1 and 2

A tissue equivalent correction factor of 1.28 for hydrogen recoils is necessary.

The attenuation factor for neutron and gamma doses are calculated as follows:

Attenuation factor for neutrons:

The linear attenuation coefficient $\Sigma_{n,p}$ cm^{-1} is equal to $N_H \sigma_{n,p}$, where $\sigma_{n,p}$ is the hydrogen scattering cross-section, which can be calculated from the formula of Klien-Nishina (Marion and Fowler, 1960) :

$$\sigma_{n,p} = \Pi\ [5.603 / (1 + 7.415\ E_n + 0.1105\ E^2_n) + 0.8652 / (1 + 0.2427\ E_n + 0.08\ E^2_n)]\ \text{barns / atom}$$

Using an average neutron energy of 4.4 Mev for Am-Be source, $\sigma_{n,p} = 1.234$ barns,

$\Sigma_{n,p} = N_H \sigma_{n,p} = 0.0594\ cm^{-1}$

Hence, the attenuation factor $\frac{\Sigma t}{1-e^{\Sigma t}} \simeq 1.12$

Attenuation factor for gamma radiation:

The correction factor for gamma dose rate to be applied to the results presented in Table 3.8 was calculated for NE213 at 4.43 Mev gamma energy $\mu = N_e \sigma$. where σ is obtained at 4.43 Mev from E. Tochlin and B.W.Sumway, 1969, using the data given in Table 3.1.

This gives a correction factor $\frac{\mu t}{1-e^{\mu t}} \simeq 1.04$

Neutron source strength uncertainty:

The neutron source was a non-calibrated source and an estimate of $\pm$ 0.8 x 10^5 and 0.8 x 10^6 $n.s^{-1}$ uncertainty is recommended by the Radio-Chemical Centre, Amersham.

Background corrections:

The background for both neutron and gamma measurements was measured at 0.6 $\mu Sv h^{-1}$ and 0.06 $\mu Sv h^{-1}$ respectively. Table 3.11a,b gives the correction and uncertainty factors for calculated and measured results for the neutron and gamma doses, and Table 3.12 gives the corrected calculated and measured dose rates.

The experimentally measured dose rates for neutron and gamma fluxes agrees favourably to within 5% with the calculated and measured results of other authors (D.Nachtigal 1967, E.Tochlin and B.W.Shumway 1969, J.A.Axier et al 1968, M.Fry 1966 and J.L.Silberberg 1977). A small difference is expected due to the perturbation of neutron and gamma fields, especially at positions closer to the source.

Source ($n.s^{-1}$)	Position (m)	Source strength uncertainty μ Svh^{-1}	Attenuation factor	Source detector position uncertainty μ Svh^{-1}	Hydrogen tissue dose correction factor	Total thermal dose correction factor μ Svh^{-1}	Standard deviation of measurement	Background correction μ Svh^{-1}	Carbon recoil dose correction factor μ Svh^{-1}
Source 1	0.3	± 8	1.12	± 0.7	1.28	7.96	± 0.8	0.6	3.53
	0.5	± 2.88	1.12	± 0.2	1.28	2.86	± 0.2	0.6	1.273
$7.5x10^5$	1.0	± 0.72	1.12	± 0.02	1.28	0.72	± 0.02	0.6	0.318
Source 2	0.3	± 80	1.12	± 7	1.28	79.60	± 8	0.6	35.30
	0.5	± 28.8	1.12	± 2	1.28	28.60	± 2	0.6	12.73
$7.5x10^6$	1.0	± 7.2	1.12	± 0.2	1.28	7.2	± 0.2	0.6	3.18

Table 3.11a: Neutron dose correction and uncertainty factors for calculated and experimental results for Am-Be source 1 and 2

Source (photon s^{-1})	Position (m)	Source strength uncertainty μSvh^{-1}	Attenuation factor	Source-detector position uncertainty μSvh^{-1}	Standard deviation of measurement μSvh^{-1}	Background correction μSvh^{-1}
Source 1 :	0.3	± 0.1	1.04	± 0.1	± 0.03	0.06
2.68 x 10^5	0.5	± 0.03	1.04	± 0.03	± 0.01	0.06
	1.0	± 0.01	1.04	± 0.01	± 0.001	0.06
Source 2 :	0.3	± 1	1.04	± 1	± 0.3	0.06
2.68 x 10^6	0.5	± 0.3	1.04	± 0.3	± 0.1	0.06
	1.0	± 0.1	1.04	± 0.1	± 0.01	0.06

Table 3.11b : Gamma dose correction and uncertainty factors for calculated and experimental results for Am-Be source 1 and 2.

Source (n.s-1)	Position (m)	Calculated neutron dose rate μSvh-1	Measured neutron dose rate μSvh-1	Calculated gamma dose rate μSvh-1	Measured gamma dose rate μSvh-1
Source 1 :	0.3	70.75 ± 13.3	70.60 ± 1.5	1.811 ± 0.1	1.73 ± 0.1
$7.5x10^5$	0.5	25.46 ± 4.7	25.06 ± 0.4	0.652 ± 0.03	0.56 ± 0.04
	1.0	6.36 ± 1.22	5.9 ± 0.04	0.163 ± 0.01	0.10 ± 0.01
Source 2 :	0.3	707.5 ± 133	706.95 ± 15	18.11 ± 1	17.83 ± 1
$7.5x'0^6$	0.5	254.6 ± 47	257.95 ± 4	6.52 ± 0.3	5.96 ± 0.4
	1.0	63.6 ± 12.2	62.14 ± 0.4	1.63 ± 0.1	1.50 ± 0.1

Table 3.12 Corrected, calculated and measured dose rates for Am-Be source 1 and 2

CHAPTER FOUR: OPTICAL FIBRE COUPLING OF A SCINTILLATOR AND PHOTOMULTIPLIER

4.1 Introduction:

There was a significant difference in the measurements of gamma dose rates from the calculated dose rates reported in Chapter 3, and a smaller difference in the measurements of mixed neutron and gamma dose rates in the mixed radiation fields. It was resolved to improve these results, reducing the perturbation of neutron and gamma fields by the detector, particularly at distances close to the source.

The photomultiplier was replaced by one with an effective photocathode diameter of 1cm, a higher quantum efficiency, higher sensitivity and a lower dark current, to allow the scintillator to be optically coupled to the photomultiplier via a suitable fibre bundle guide.

Further details of these experimental changes and the consequent results are given later in this chapter and in Chapter 5. The remainder of this chapter describes the characteristics of optical fibres, so as to illustrate the problems encountered in their use and to explain the arrangements adopted in optically coupling a scintillator and photomultiplier.

4.2 Optical Fibre Theory:

An optical waveguide is a dielectric structure that transports energy at wavelengths in the infrared or visible portion of the electromagnetic spectrum, and generally is divided into

three regions, as shown in Figure 4.1. The central region is the core, which is surrounded by the cladding, which in turn is surrounded by a protective jacket. Within the core, the refractive index profile (n) can be uniform or graded. The cladding index, corresponding to step index and graded index fibres, is typically uniform. It is necessary for the core index to be greater than the cladding index if the fibre is to function as an optical waveguide.

Optical waveguides can be divided into subclasses: multimode waveguides (with comparatively large cross section cores) and single mode waveguides (with comparatively small cores).

Multimode waveguides obey the condition:

$$\frac{2\Pi a}{\lambda} (n_{co}^2 - n_{cl}^2)^{1/2} >> 1,$$

where a is the redius of the fibre core, λ is the wavelength of light in free space, n_{co} is the maximum refractive index in the core and n_{cl} is the uniform refractive index in the cladding.

Multimode fibres allow the propagation of a finite number of guided modes along the channel. The number of guided modes is dependent upon the physical parameters (i.e. refractive index, core radius) of the fibre and the wavelength of the transmitted light. The approximate expression of the number of guided modes for step index fibres is given by (Gloge, 1971).

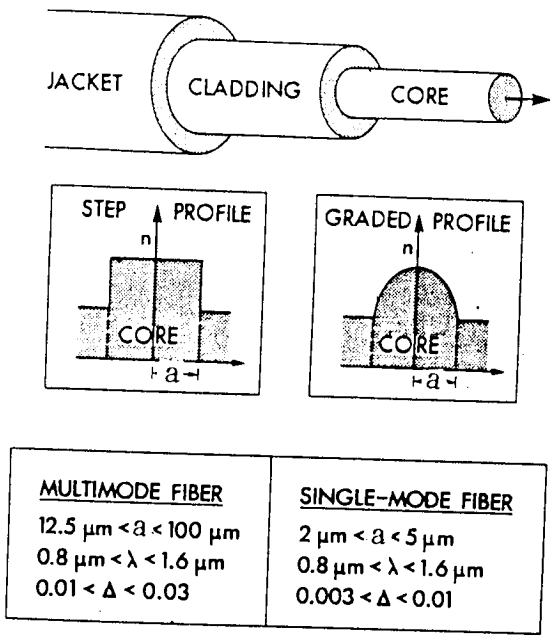

Figure 4.1 Nomenclature, profile and ranges of dimensions for typical optical fibre, where a is the core radius and λ is the free space wavelength of light (J.N.Senior, 1985)

$M_s \simeq \frac{f^2}{2}$; where f is the frequency of the fibre. For single mode step-index fibre (small core diameter), the frequency of the propagation is given by (J.N.Senior, 1985):

$$f = \frac{2\pi}{\lambda} a n_{co} (2\Delta)^{1/2}, \text{ where } \Delta = \left[1 - \frac{n_{cl}^2}{n_{co}^2}\right]^{1/2}$$

and a single mode is possible only over the range $0 \leq f \leq 2.405$ (Snitzer, 1961)

Graded index fibres do not have a constant refractive index (core) but decreasing core index n_r with radial distance, from a maximum values of n_{co} at the axis to a constant value n_{cl} beyond the core radius (a) in the cladding. The index variation may be expressed as:

$$n_{(r)} = n_{co}\left[1-2\Delta\left(\frac{r_s}{a}\right)^{\alpha}\right]^{1/2} \qquad \text{for } 0 \leq r_s \leq a$$

$$n_{(r)} = n_{co}[1-2\Delta]^{1/2} \approx n_{co}[1-\Delta] = n_{cl} \qquad \text{for } r_s \geq a$$

The number of modes which can propagate in graded index fibre of core size a and index profile α (where α is a positive constant, the power law coefficient of the refractive index distribution) is given by (G.Keiser, 1976) :

$$M_s = \frac{\alpha}{\alpha+2} \frac{(2\pi a n_{co})^2}{\lambda} \Delta \qquad \text{.....4.1}$$

Since only rays with angle to the normal greater than the critical angle θ_c at the core cladding interface are transmitted by total internal reflection, it is evident that not all rays extering the fibre core will continue to be propagated down its length. The geometry concerned with launching a light ray into an optical fibre is shown in Figure 4.2. From Snell's Law the minimum angle ϕ_{min} that supports total internal reflection for step index fibre is $\sin(\phi min) = \frac{n_{co}}{n_{cl}}$

Rays strike the core-cladding interface at angles less than θ_{min} will refract out of the core and be lost in the cladding. The condition can be related to the maximum entrance angle $\theta_{o,max}$ through the relation:

$$n \sin \theta_{o,max} = n_{co} \sin \theta_c = (n_{co}^2 - n_{cl}^2)^{1/2}$$

where θ_c is the critical angle and n is the air refractive index. Thus, those rays having entrance angles θ_o less than $\theta_{o,max}$ will be totally internally reflected at the core-cladding interface.

The maximum angle to the axis that light may enter the fibre in order to propagate is called the acceptance angle of the fibre (NA),

$$NA = n \sin \theta_{o,max} = (n_{co}^2 - n_{cl}^2)^{1/2} \qquad o \leq \theta_{co} \leq \theta_{o,max}$$

Further details of optical fibre theory are given in Appendix C.

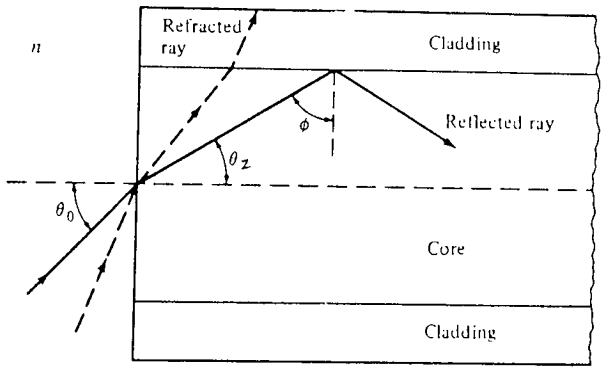

Figure 4.2 Meridional ray optics representation of the propagation mechanism in an ideal step-index optical wave-guide (G.Kieser, 1976)

4.2.1 Transmission Characteristics:

The attenuation or transmission loss of optical fibres proved to be one of the most important factors in the development of optical fibre. The transmission losses of optical fibres are commonly determined by measuring the total power at two points of separation L (Tynes et al 1972, Keck et al 1972, and Kaiser et al 1973). With P_{out} representing the power at the output, and P_{in} the power at the input, the normalized loss α is given by:

$$\alpha = \frac{10}{L(km)} \text{Log}\left(P_{out}/P_{in}\right) \text{ (dB/km)}$$

An ideal fibre would have no loss so that $P_{out} = P_{in}$, and this corresponds to 0dB attenuation, which in practice is impossible. An actual low-loss fibre may have a 3dB km^{-1} average loss. This means that the optical signal power would decrease by 50% over a 1km length and would decrease by 75% over a 2km length.

The transmission efficiency is determined by both the scattering and absorption characteristics of the fibre. Absorption is caused by three different mechanisms:

(a) Absorption by atomic defects in the glass composition.

(b) Extrinsic absorption by impurity atoms in the glass material.

(c) Intrinsic absorption by the basic constituent atoms of the fibre material.

The dominant absorption factor in the fibre is the absorption results predominantly from transition metal ions such as iron, chromium, cobalt and copper, and from OH (water) ions. Intrinsic absorption results from electronic absorption bands of the glass material in

the ultraviolet region and from atomic vibration bands in the near infrared region.

In the near infrared region, above 1.2 μm, the optical wave guide loss is determined by the presence of OH ions and the inherent infrared absorption of the constituent material.

Scattering loss in the glass arises from microscopic variations in the material density, from compositional fluctuations and from structural inhomogenuties or defects occurring during fibre manufacture. For multicomponent glasses, the scattering loss is known as Rayleigh scattering, and is given by (R.Olshansky, 1975):

$$\zeta = \frac{8\pi^3}{3\lambda^4} (\delta n_{co}^2)\, \delta V,$$

where n_{co} is the refractive-index of the core, and δV is the volume of the glass material.

Since Rayleigh scattering has a λ^{-4} dependence, it decreases dramatically with increasing wavelength. Figure 4.3 shows typical transmission characteristics of glass optical fibres.

Graded-index low loss fibres (< 10 dB km^{-1}) can be obtained by both multicomponent glasses and fused single core fibres. The multicomponent glasses generally have numerical apertures of less than 0.2. However, they can be made in the step-index version, with large cores, for use with LED light sources.

Silica core - silicon clad fibres can be fabricated with numerical apertures of approximately 0.4 and with losses below 10 dB km^{-1} for wavelengths from 0.8 to 0.85 μm.

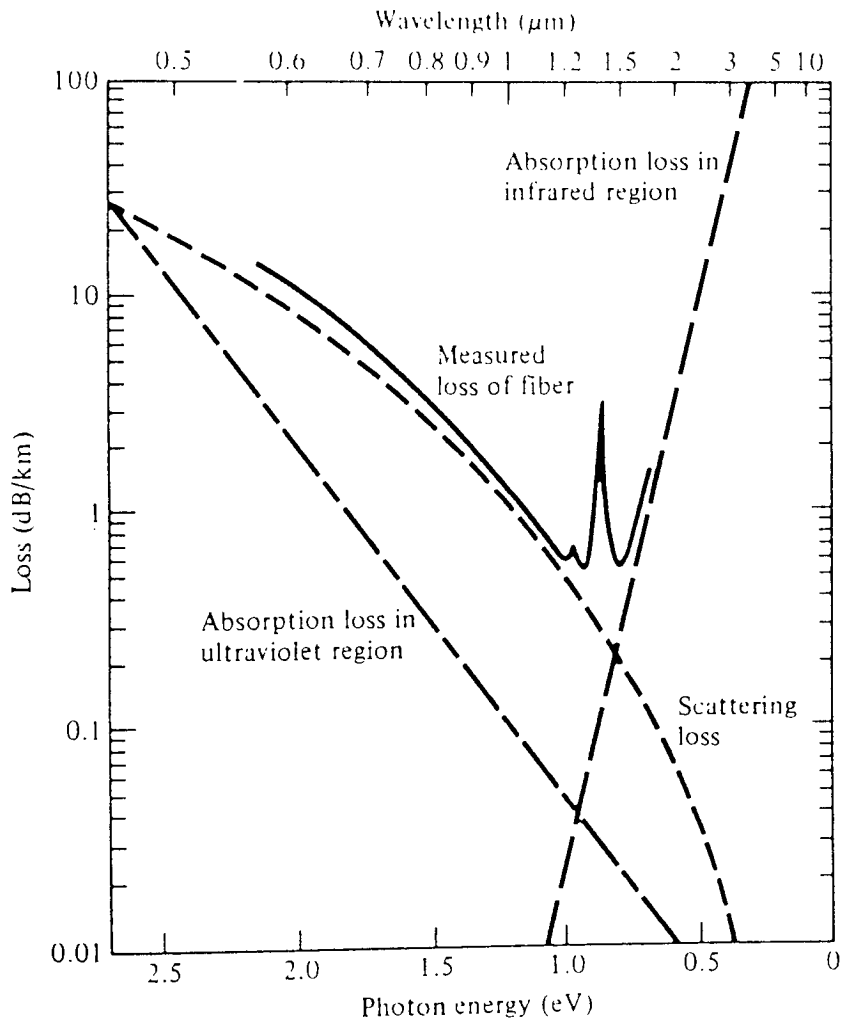

Figure 4.3 Optical fibre attenuation characteristics and their limiting mechanism for a Ge O_2. doped low-loss low-OH content fibre (Osanai et al).

Graded-index silica-borosilicate fibres produced by MCVD (modified chemical vapour deposition) exhibit low loss, but are limited to numerical apertures below 0.18. Higher numerical aperture fibres (up to 0.4) can be produced by MCVD but they consist of a GeO_2-SiO_2 core composition with small amounts of B_2O_3 or P_2O_5 and SiO_2 cladding. They exhibit losses generally below 5 dB km^{-1} in the range of 0.85 to 1.06 μm.

The MCVD method has also been successfully applied to the fabrication of single-mode fibres of borosilicate composition with losses of less than 2 dB km^{-1} (Kuppers et al 1976, Geither et al 1976, and J.B.MacClesney et al, 1974).

4.3 Fibre Coupling:

A measure of the amount of optical power emitted from a source that can be coupled into a fibre is usually given by the coupling efficiency $\eta = \frac{P_f}{P_s}$

where P_f is the power coupled into the fibre and P_s is the power emitted from the light source. The launching or coupling efficiency depends on the type of fibre that is attached to the source and on the coupling process.

A convenient and useful measure of the optical output of a luminescent source is its radiance. Radiance is the optical power radiated into a solid angle per unit emitting surface area and is generally specified in terms of watts per square centimeter per steradian. Since the optical power which can be coupled into a fibre depends on the radiance of an optical source rather than the total output power, the radiance is an important parameter when considering source to fibre coupling efficiency.

If we consider a lambertian source in which the radiant intensity at an angle θ, $I(\theta)$ is given by $I(\theta) = I_o \cos\theta$, where I_o is the radiant intensity along the line $\theta = 0$.

For a source which is smaller than, and in close proximity to, the fibre core, and assuming cylindrical symmetry, the coupling efficiency $\Im_{max}$ for a step-index fibre is given by (J.R.Senior 1985). :

$$\Im_{max} = \frac{\int_o^{\theta_{omax}} I(\theta) \sin\theta \, d\theta}{\int_o^{\pi/2} I(\theta) \sin\theta \, d\theta} = \sin^2\theta_{omax} \qquad \ldots\ldots 4.2$$

$$= \quad NA^2 \qquad \text{for } r_s \leq a$$

$$= \quad NA^2 \left(\frac{a}{r_s}\right)^2 \qquad \text{for } r_s > a$$

For graded-index fibre, where NA depends on the distance r from the fibre axis for $r_s < a$, $\Im_{max} = NA^2 - \frac{NA^2}{2}\left(\frac{r_s}{a}\right)^2$ for $\alpha = 2$ and $r_s < a$(core),

which clearly shows that the coupling efficiency for step-index fibres is higher than graded-index fibres by a factor of $\frac{NA^2}{2}\left(\frac{r_s}{a}\right)^2$

(Further information on coupling efficiency is given in Appendix D).

If the refractive index (n) of a medium is different from the core index n_{co}, then the power coupled into the fibre reduced by a factor

$$R = \left[\frac{n_{co} - n}{n_{co} + n}\right]^2 \qquad \text{(J.M.Senior 1985)}$$

The fibre accepts only those rays contained within a cone whose maximum angle is determined by total internal reflection at the core-cladding interface. Hence, an input coupling loss will result if the angular emission cone of the source exceeds that defined by the numerical aperture of the fibre. This is illustrated in Figure 4.4 for a source coupled to a single strand fibre. Only those rays contained within the core shaded cone are trapped in the core.

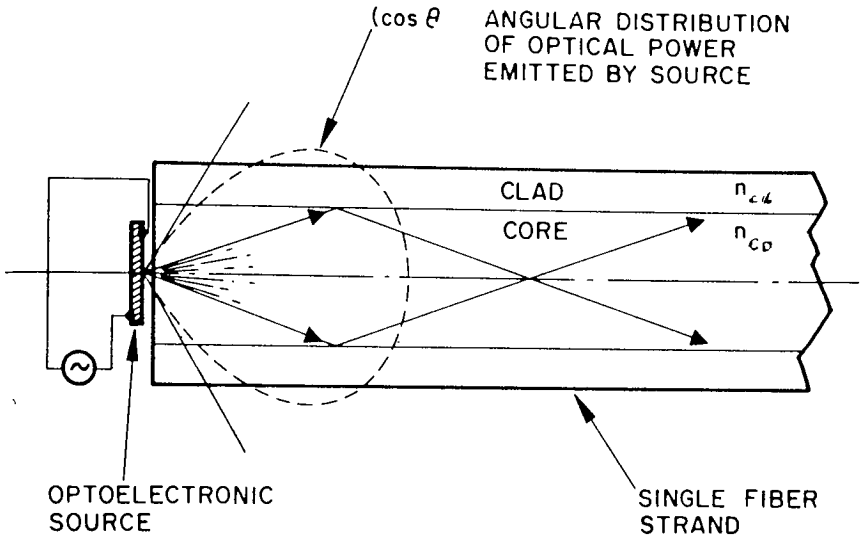

Figure 4.4 Schematic diagram of source coupled to single strand fibre wave-guide(G.Kieser, 1976)

4.3.1 The Use of a Lens to Improve Coupling Efficiency

The optical power-coupling analysis given earlier is based on coupling a flat fibre end face directly over the light source. If the source-emitting area is larger than the fibre core area, then the resulting optical power coupled into the fibre is the maximum that can be achieved. This is a result of fundamental energy and radiance conservation principles (A.Born and E.Wolf, 1965), also known as the law of brightness. However, if the emitting area of the source is smaller than the core area, a miniature lens may be placed between the source and the fibre to improve the power coupling efficiency (G.Keiser 1976).

The function of the microlens is to magnify the emitting area of the source to match exactly the core area of the fibre end face. If the emitting area is increased by a magnification factor M, the solid angle, within which optical power is coupled to the fibre from the source, is increased by the same factor. Several possible lensing schemes are used. These include a rounded-end fibre, a small glass sphere (non-imaging microsphere) in contact with both the fibre and the source, a larger spherical lens used to image the source on the core area of the fibre end and a taper-ended fibre.

One of the most efficient lensing methods is the use of non-imaging microsphere (G.Keiser 1976), Figure 4.5. In making the practical assumptions that the spherical lens has a refractive index of about 2.0, the outside medium is air (n = 1.0) and the emitting area is circular, this gives the object distance $s = f = 2R_L$ where f is the focal length and R_L is the radius of curvature of the lens, and the focal point is located on the lens surface

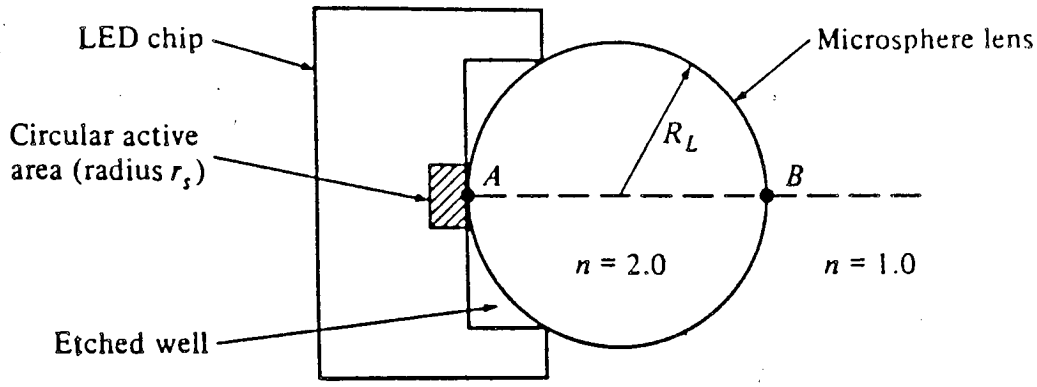

Figure 4.5 Schematic diagram of an LED emitter with microsphere lens.

(G. Keiser, 1976)

placing the source close the the lens surface results in a magnification M of the emitting area. This given by the ratio of the cross sectional area of the lens to that of the emitting area:

$$M = \frac{\pi R_L^2}{\pi r_s^2} = \left(\frac{R_L}{r_s}\right)^2$$

Using equation (4.2), it can be shown that, with the lens, the optical power P_L that can be coupled into a full aperture angle 2θ is given by:

$$P_L = P_s \left(\frac{R_L}{r_s}\right)^2 (\sin^2\theta) = P_s M NA^2$$

where P_s is the total output power from the source without the lens.

For a fibre of radius a and numerical aperture NA, the maximum coupling efficiency $\Im_{max}$ is given by:

$$\Im_{max} = \left(\frac{a}{r_s}\right)^2 NA^2 \quad \text{for} \quad \frac{r_s}{a} > NA$$

$$= 1 \quad \text{for} \quad \frac{r_s}{a} \leq NA$$

Thus when the radius of the emitting area is larger than the fibre radius, no improvement in coupling efficiency is possible with lens. In this case, the best coupling efficiency is achieved by a direct-butt method.

It is of interest to note that optical power launched into the fibre does not depend on the wavelength of the source but only on its brightness. Since the number of modes which can be propagated in graded index fibre is given by equation 4.1:

$$M_S = \left(\frac{2\pi a n_{co}}{\lambda}\right)^2 \Delta \frac{\alpha}{\alpha+2} ,$$

where, a is the fibre radius and α is the index profile.

Thus, for example, twice as many modes propagate in a given fibre at 900 nm than at 1300 nm. The radiant power per mode P_s / M_s from a source at a particular wavelength is given by the radiance, B_0, multiplied by the square of the nominal source wavelength, i.e. $P_s / M_s = B_0 \lambda^2$. Twice as much power is launched into a given mode at 1300 nm than at 900 nm. Hence, two identically sized sources operating at different wavelengths but having identical radiances will launch equal amounts of optical power into the same fibre.

4.4 Optical Fibre Bundles:

Since the input coupling loss from a small area device into a single strand of fibre waveguide varies as $(NA)^2$, a considerable amount of power emitted by the source is lost in the coupler. It is possible to minimise the input coupling loss by using a fibre bundle configuration and inserting an optical element such as a lens. If the proper choice is made, the input coupling efficiency can be reduced to the packing fraction loss. Estimates of such losses can be obtained by considering some basic bundle configurations, such as those illustrated in Figure 4.6.

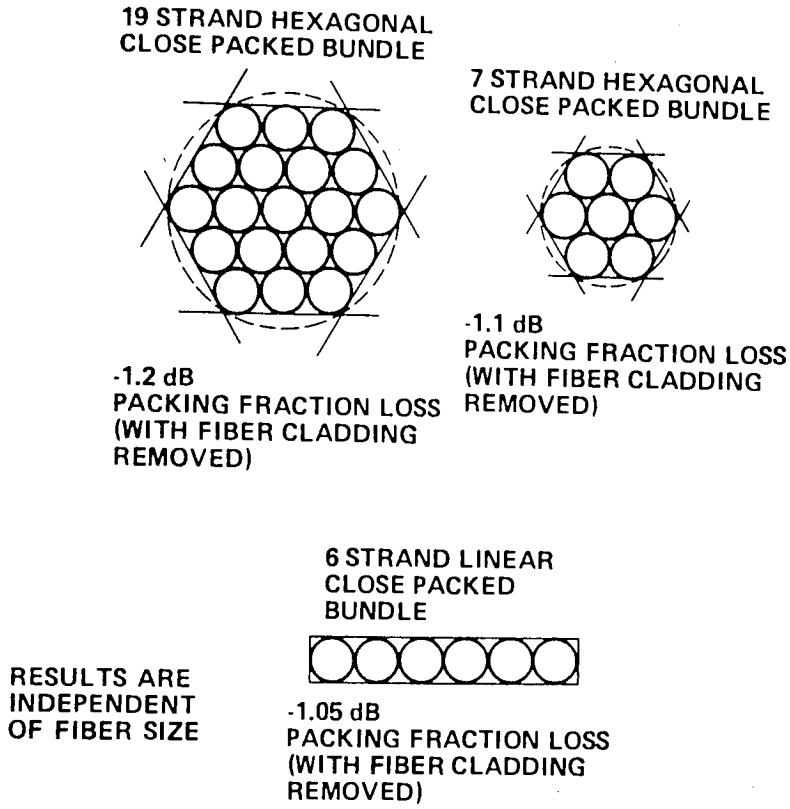

Figure 4.6 Basic bundle configurations for close-packed fibre bundles.

(R.Tiedeken, 1973)

The packing fraction for a hexagonal, closed packed bundle containing a total of N fibres with N_d fibres along the diameter of the smallest circumscribed circle containing all fibres in the bundle is given by (G.Kieser 1976) :

$$f_p = \frac{N}{N_d^2} \left(\frac{a_{co}}{a_{cl}}\right)^2$$

where a_{co} is the core diameter of the fibre and a_{cl} is the fibre diameter (core + clad).

For bundles assembled using fibres with a thick cladding which has not been stripped from the core, such as fibres with 125μm overal diameter and 95μm core diameter, the packing fraction increased by the factor: $(a_{co} / a_{cl})^2$. In the example considered, the total bundle packing fraction is -5.6 dB km^{-1}.

In a hexagonal closed packed bundle, the highest packing fraction is achieved using fibres with inherently very thin cladding, or fibres where the cladding is essentially stripped from the core over the short length of the coupler. When $a_{co} = a_{cl}$ the packing fraction becomes N / N_d^2 , which is approximately -1.2 dB km^{-1} for hexagonal bundles containing either 7, 19, 37 or 61 fibres.

The packing fraction for a linear closed-packed bundle, again containing a total of N fibres, is given by (H.F.Wolf 1979):

$$f_p = \frac{\pi}{4}\left[\frac{N}{1+(N-1)\frac{a_{cl}}{a_{co}}}\right]$$

For bundles with fibres of 125 μm outside diameter and 75 μm core diameter, the packing fraction increase by a factor of approximately -2 dB km^{-1} for bundles containing 6 to 20 fibre waveguides. The total packing fraction for these bundles is approximately -3dB km^{-1}, which is approximately 2.5 dB km^{-1} better than the loss associated with the hexagonal format. The higher packing fraction is achieved using fibres with thin cladding.

Light guides commercially available have the polychromatic transmittances given in Table 4.1 (R.Tiedeken 1973), and the spectral transmission as a function of wavelength is given in Figure 4.7 (H.F.Wolf 1979).

Coupling losses equal to the packing fraction losses have been observed by E.Schil 1974, employing a ball lens and linear, six strand bundle of low loss fibre whose emission was contained with a ± 30° cone. The components were arranged as shown in Figure 4.8. The lens reduces the angular content of the optical fibre radiation to the numerical aperture of the fibre, which simultaneously maintains the size of the radiation pattern at the input to the bundle equal to that of the bundle area itself. Thus the input coupling loss can be reduced to the packing fraction loss if the angular emission from the source (θ_s) can be sufficiently collimated so as to have no angle (θ_I) greater than the numerical aperture of the fibre.

Length (mm)	Transmittance %
500	≈ 60 to 40
1000	≈ 55 to 35
1500	≈ 50 to 30
2000	≈ 45 to 25
For $20\mu m \leq a \leq 70\mu m$ and $0.5 \leq NA \leq 0.6$	

Table 4.1 The transmittance of ordinary commercial light guides (R.Tiedeken,1973).

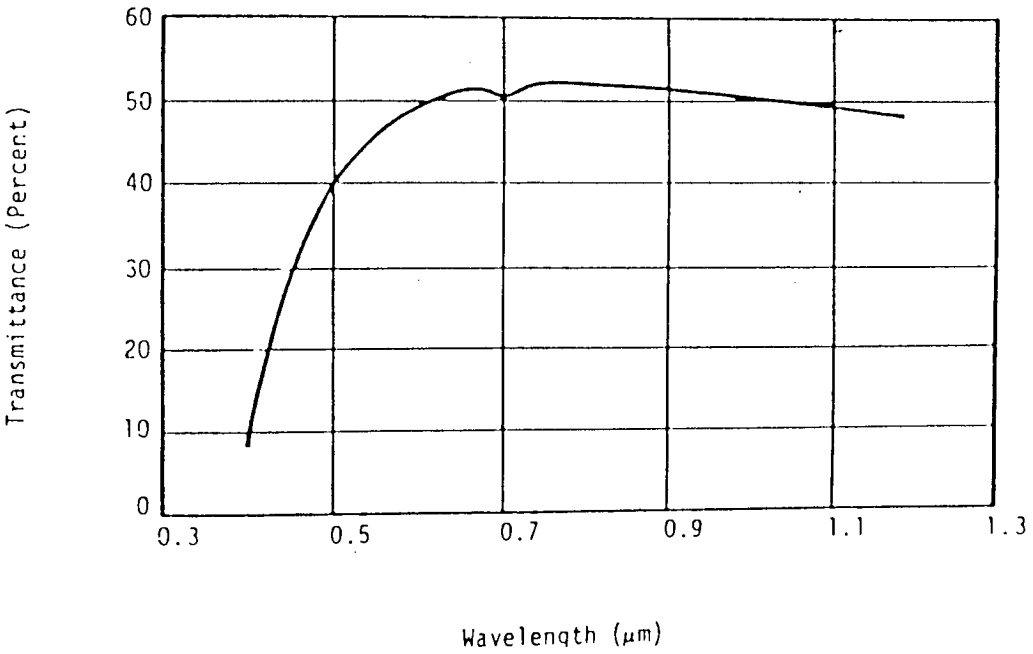

Figure 4.7 Spectral transmittance of a fibre bundle 2m long of NA = 0.55

(R.Tiedeken, 1973)

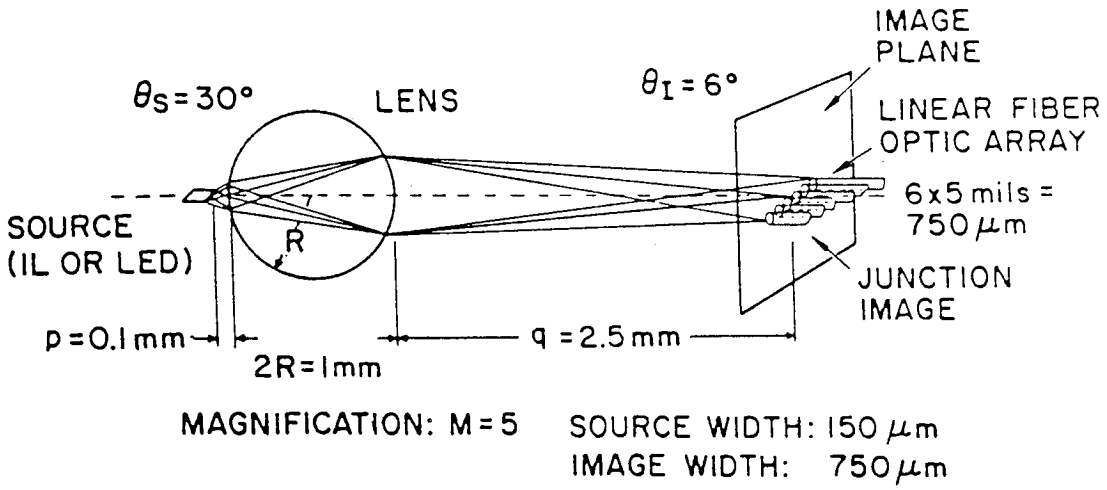

Figure 4.8 Schematic diagram of image formation by a "ball lens" source-to-fibre bundle input connector (Courtesy of E.Schiel, U.S. Army Electronics Command N.J. Ft. Monmouth).

Light emerges from the end of optical fibre bundles, diverging in approximately a 67 degree cone. To provide more intense illumination in a small area a 'lens head' has been designed (Ealing Electro-Optics plc), for 6.4 mm bundles which reduces the divergence to approximately 15 degrees. This device slips conveniently over the end of the fibre bundle and attaches securely with a small set screw.

4.5 The Experimental Optical Fibre Coupling System

4.5.1 The Optical Fibre Bundle

The optical fibre used in this work was a two metre long fibre bundle of diameter 10mm*. It is a white light fibre which transmits nearer to the ultraviolet region. Figure 4.9 gives the spectral response of a two metre (50 μm single fibre diameter) fibre bundle from the same manufacturer. The acceptance angle conditions were expected to match those shown in Figure 4.10 for the 10mm fibre bundle.

As discussed in Chapter 3, the spectral output of the liquid scintillator NE213 peaks at around 425nm and, hence, the optical fibre cable should transmit the NE213 output, but with limited efficiency. As information from the manufacturer indicated a transmission capability down to 250nm instead of 350nm, an experiment was devised to measure the spectral response of the fibre bundle in the region 380nm to 900nm.

---

* Eurotic Optical Fibres Limited, Doncaster, (U.K.)

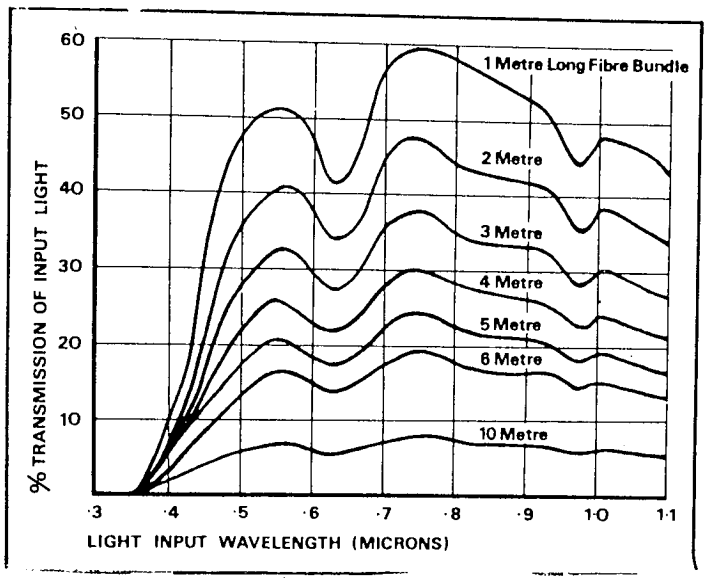

Figure 4.9 Spectral light transmission for a 50μm diameter single fibre bundle (Eurotic optical fibres)

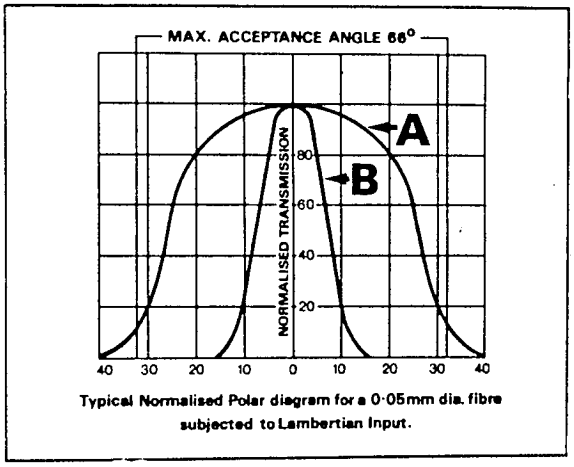

Figure 4.10 Typical normalised polar diagram for a 50μm diameter single fibre bundle. (Curve A for standard fibre product NA of 0.54 and Curve B a modified polar curve for narrow light emission) (Eurotic optical fibres)

A schematic diagram of the apparatus used is shown in Figure 4.11. A constant deviation spectrometer was used to select light of wavelength 380nm to 900nm from a tungsten-halogen white light source. This light was collimated and focused onto the end of the fibre bundle. Two detectors were used for the experiment: an S11 photomultiplier and a large area photodiode. The photomultiplier provides the higher spectral sensitivity in the wavelength region 380nm to 500nm, and the photodiode the higher spectral sensitivity in the region 500nm to 900nm. A second photodiode was used to monitor the output power fluctuations of the tungsten-halogen source. The constant deviation spectrometer was calibrated using the 633nm light from a He-Ne laser.

The measured transmission of fibre bundle can be represented as:

$$M(\lambda) = S(\lambda) \times F(\lambda) \times D(\lambda)$$

where $S(\lambda)$ is the spectral output of the source, $F(\lambda)$ the spectral transmission of the fibre bundle and $D(\lambda)$ the spectral sensitivity of the detector. Hence, $F(\lambda)$ can be obtained from the measured spectral transmission by elimination of $S(\lambda)$ and $D(\lambda)$. The spectral characteristics of the white light and the detector, i.e. $S(\lambda) \times D(\lambda)$, were investigated with both the photodiode detector and the photomultiplier without the fibre bundle. The fibre bundle was then inserted between source and detector and the spectral response again measured over the wavelength range of 380nm to 900nm. Figure 4.12 was obtained by elimination of $S(\lambda) \times D(\lambda)$ and with results from the two detectors normalised in the region of approximately 490nm to 540nm. A comparison of Figures 4.9 and 4.12 shows the same major features in each, except that the fibre bundle used in this work transmits more efficiency in the region from 350nm to 550nm.

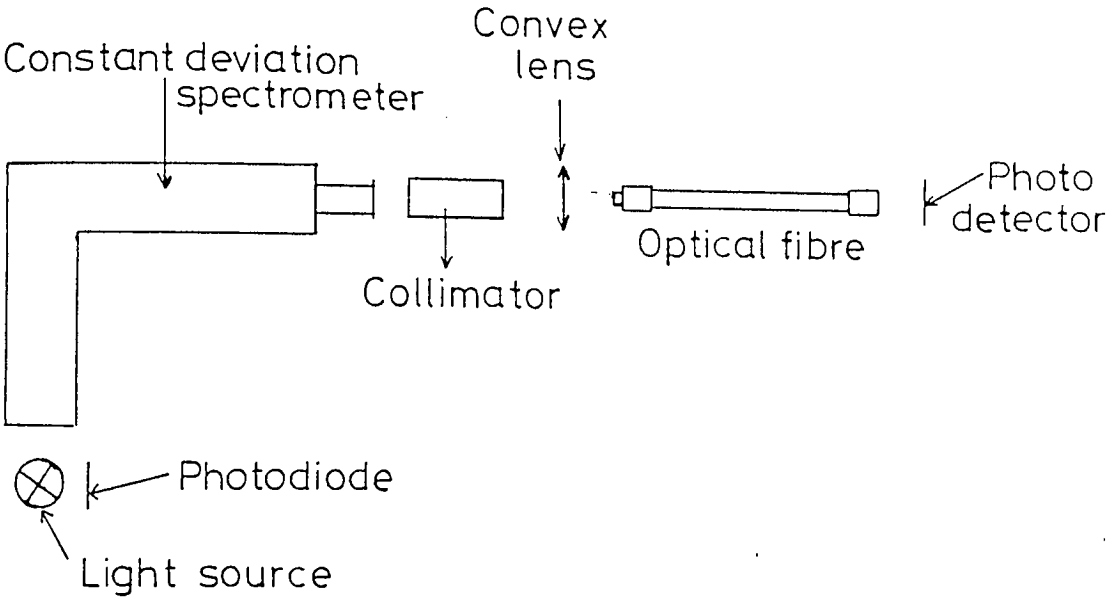

Figure 4.11 Schematic diagram of apparatus used for fibre spectral response.

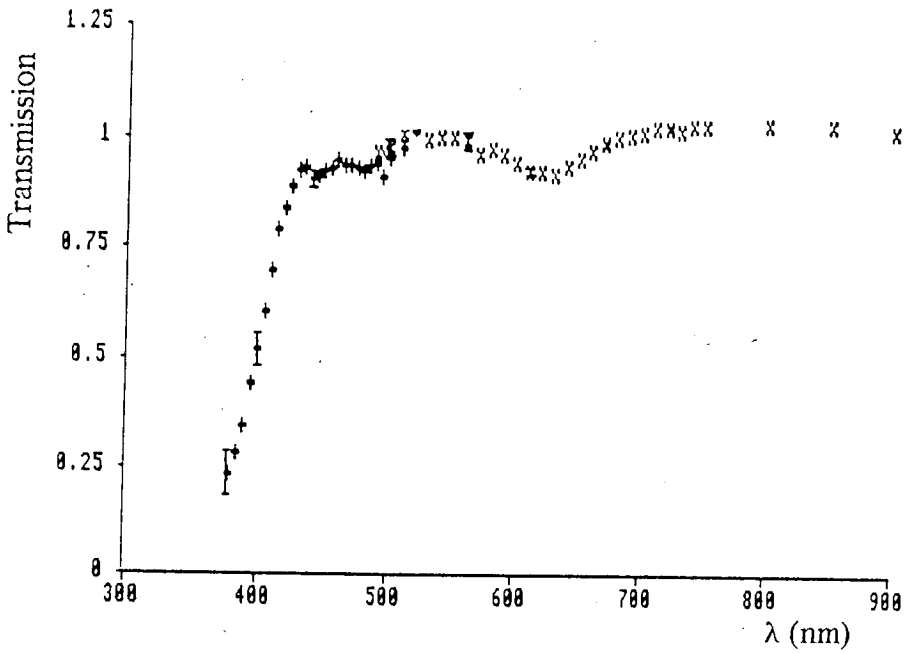

Figure 4.12 Spectral response of 10mm fibre bundle.

The experimental arrangement used to measure the numerical aperture is shown in the schematic diagram, Figure 4.13. It consists of a rotating table and adjustable arm, on which was mounted a 10mm diameter photodiode detector. The photodiode was connected to an implifier circuit and the output from the amplifier output to a digital voltmeter. A 6mm focal length convex lens was used to produce the overfill conditions required for measurement of the numerical aperture, from the helium-neon laser used as a light source. At 633nm the photodiode detector is about 70% efficient.

The intensity of output from the fibre bundle, as a function of angle from the optic axes, is shown in Figure 4.14. The acceptance angle was taken to be the 10% intensity levels, and the numerical aperture calculated from the equation: $NA = \sin^{-1} \theta_c$, where θ_c is the acceptance angle. A value for the numerical aperture of 0.56 ± 0.01 was obtained and is in very good agreement with the manufacturers value of 0.54 for the standard single fibre of 50μm diameter.

4.5.2 The Photomultiplier Response

The S11 photocathode of the photomultiplier used in the measurements of the gamma and neutron dose previously described (Chapter 3) has a 40mm diameter sensitive area and a spectral response, Figure 4.15, which are not well matched to the fibre bundle. The photomultiplier was replaced with an EMI 9789B bialkali cathode tube, Table 4.2, which incorporates a modified first dynode input section to reduce the effective photocathode diameter to 10mm. This results in very low dark current, essential for low light level applications, whether d.c. or photon counting. A "good" signal-to noise ratio can be

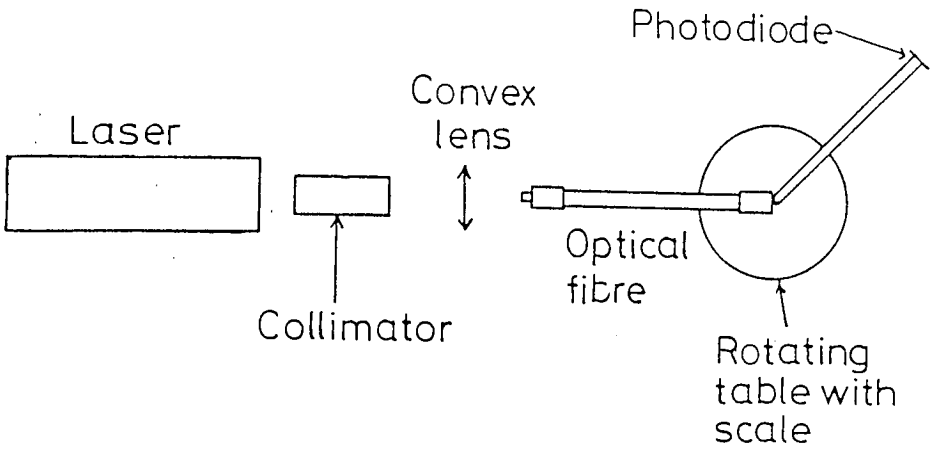

Figure 4.13 Experimental arrangements for measuring the numerical aperture of the 2m cable.

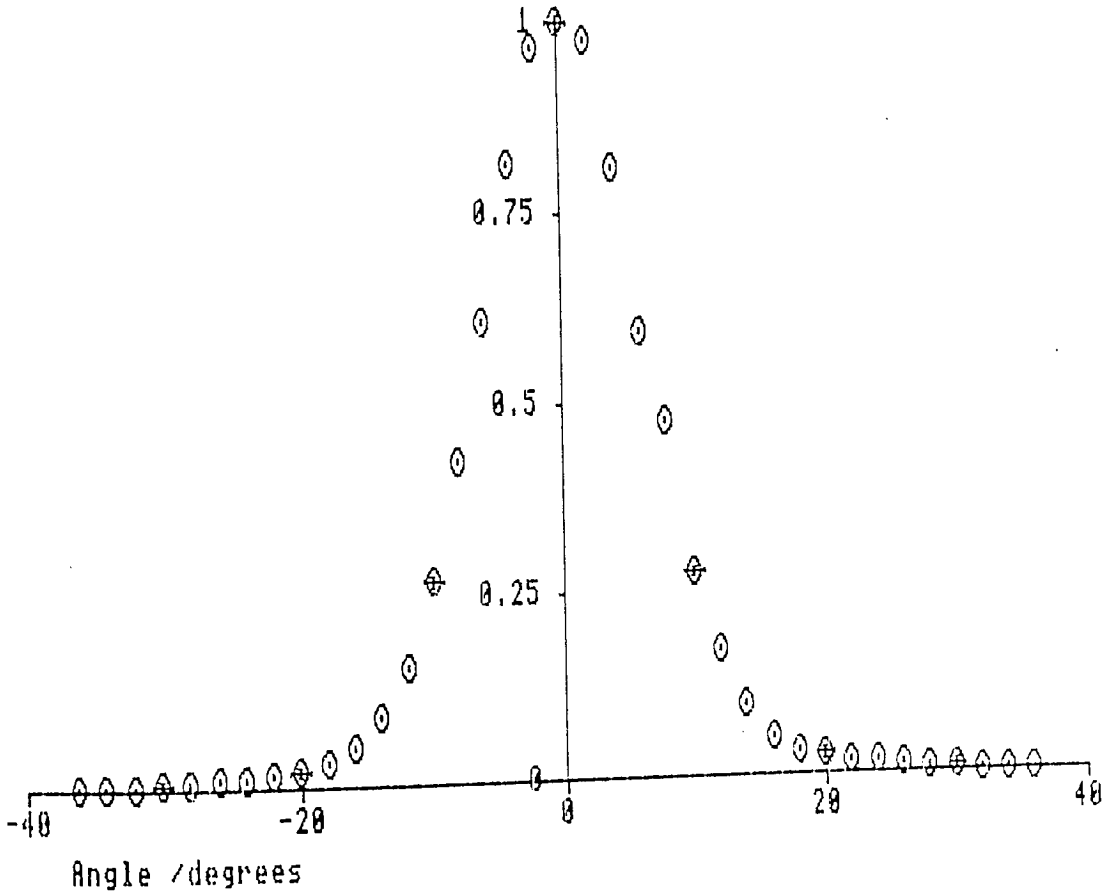

Figure 4.14 Normalised acceptance angle for the experimental numerical aperture.

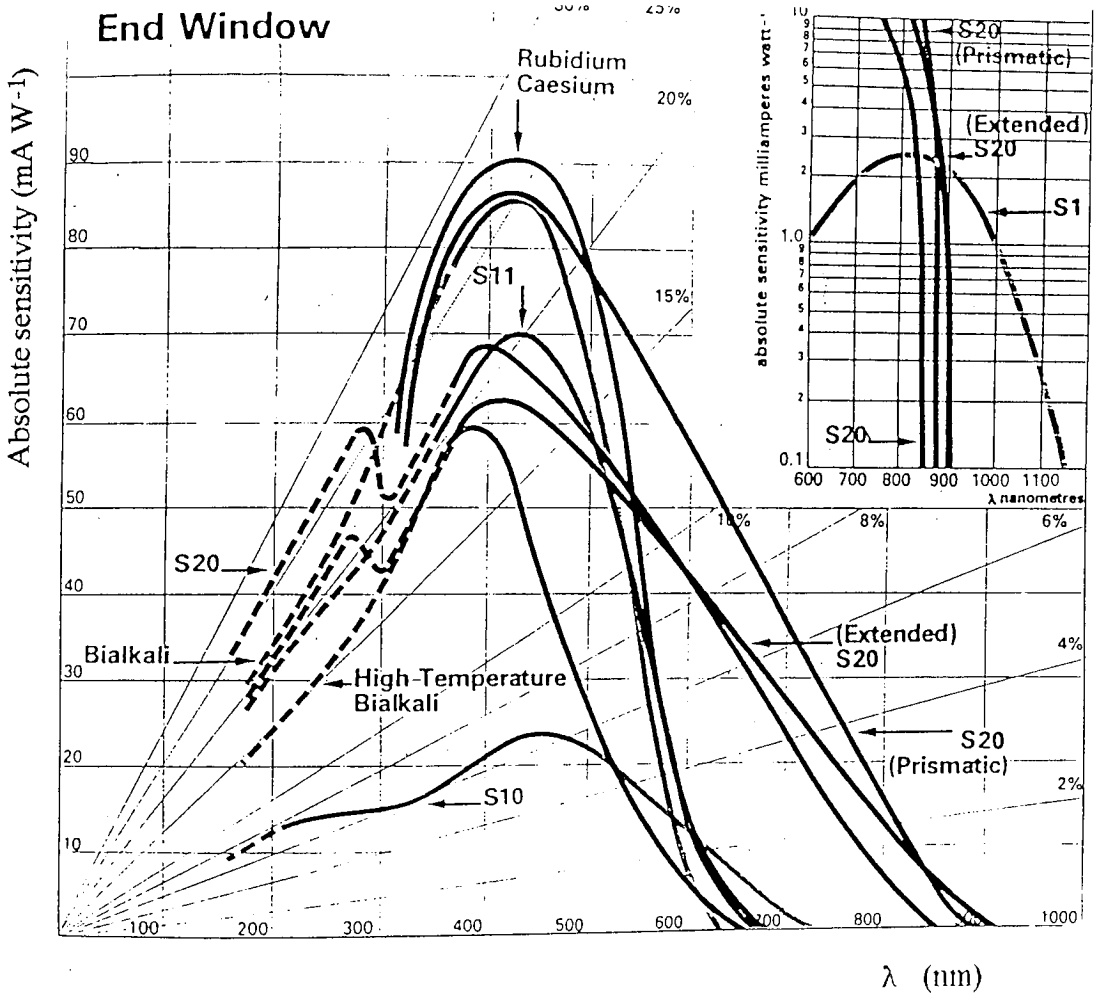

Figure 4.15 Typical spectral response of 9789B photomultiplier (Thorn EMI. 1984)

Effective cathode diameter (mm)	10
Anode sensitivity (A/Lm) Vk-a (V) Photomultiplier Gain	2000 1100 → 1500 2.7 x 10^7
Quantum efficiency (%)	25
Dark emission (nA/Lm)	mimimum 0.3, maximum 1.5
Rise time (ns)	10

Table 4.2: Photomultuplier 9789B data

obtained even from energy less than a few kev for gamma, and less than 50 kev for neutrons, from stilbene or NE213 scintillator. The green-shifted spectral sensitivity of the rubidium-caesium photocathode of the 9879B photomultiplier illustrated in Figure 4.15 improves the spectral match of the optical fibre bundle and photomultiplier.

Although the cable is able to transmit radiation reasonably well at 425nm, the wavelength of the maximum light output of the NE213, a higher transmission efficiency could be achieved by shifting the wavelength of the radiation emitted from the scintillator to around 500nm. This was attempted by placing a 12.7 x 10mm conical glass device (BBQ)* between the NE213 liquid scintillator source and the fibre, as illustrated in Figure 4.16. The liquid scintillator used had the same characteristics as listed in Table 3.1, except for the dimensions 12.7 x 25.4mm.

The response of the system was investigated using a ^{60}Co gamma source. The output spectrum for different configurations, with and without the optical fibre bundle and wavelength shifter are illustrated in Figures 4.17, 4.18, 4.19 and 4.20, respectively. From these results it is evident that no improvement in light transmission efficiency is possible using the wavelength shifter in conjunction with the optical fibre bundle. The photons absorbed by the wavelength shifter are scattered in all directions and only those within the acceptance angle of the fibre are being collected.

---

* BBQ - Supplied by Nuclear Enterprise Ltd (U.K.)

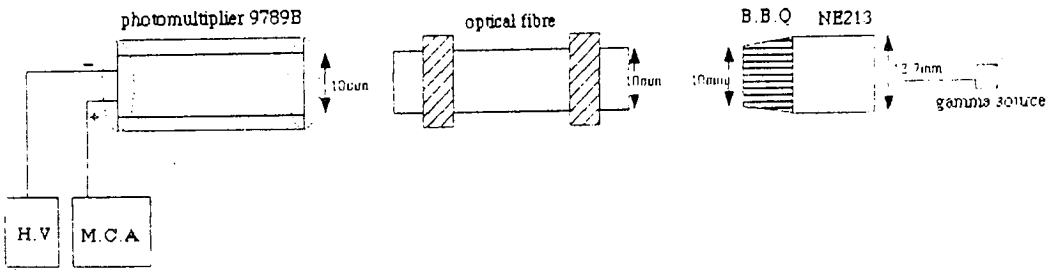

Figure 4.16 Schematic arrangement for B.B.Q. testing with optical fibre.

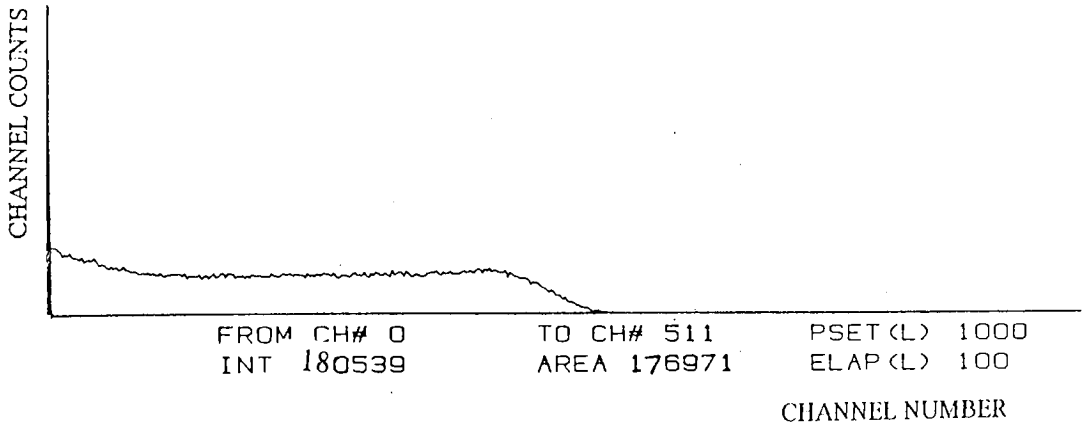

Figure 4.17 Gamma spectrum for ^{60}Co gamma source

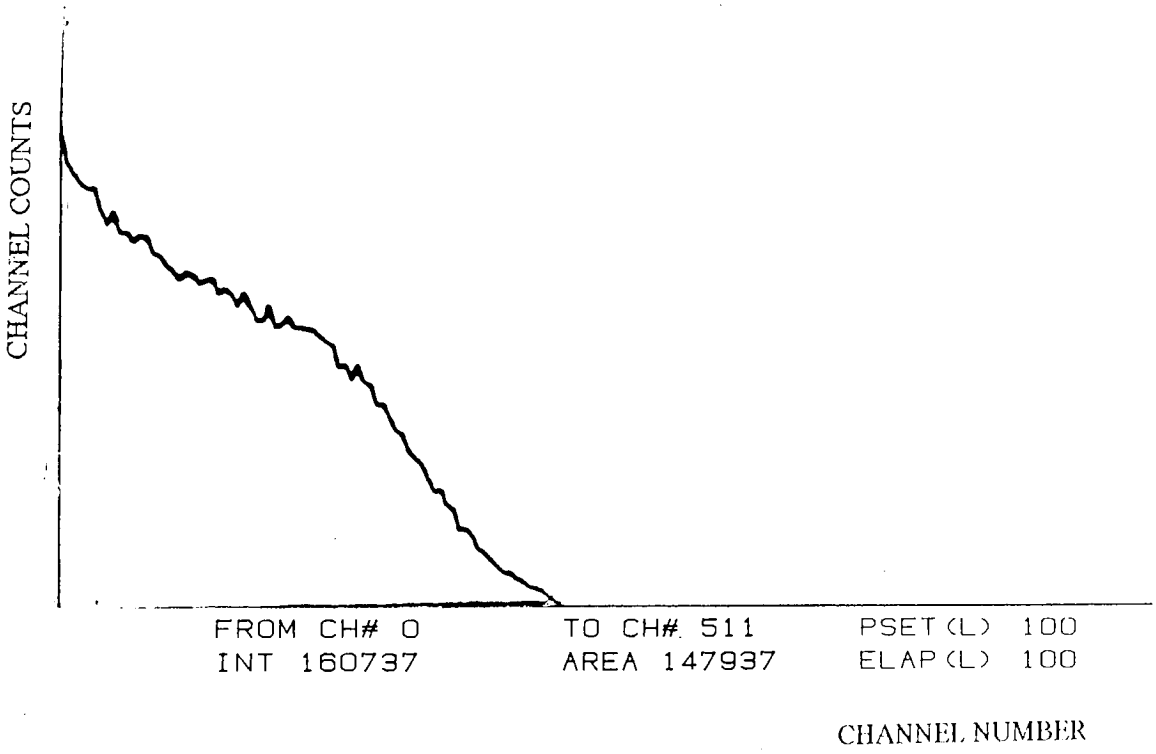

Figure 4.18 Gamma spectrum for ^{60}Co gamma source with fibre

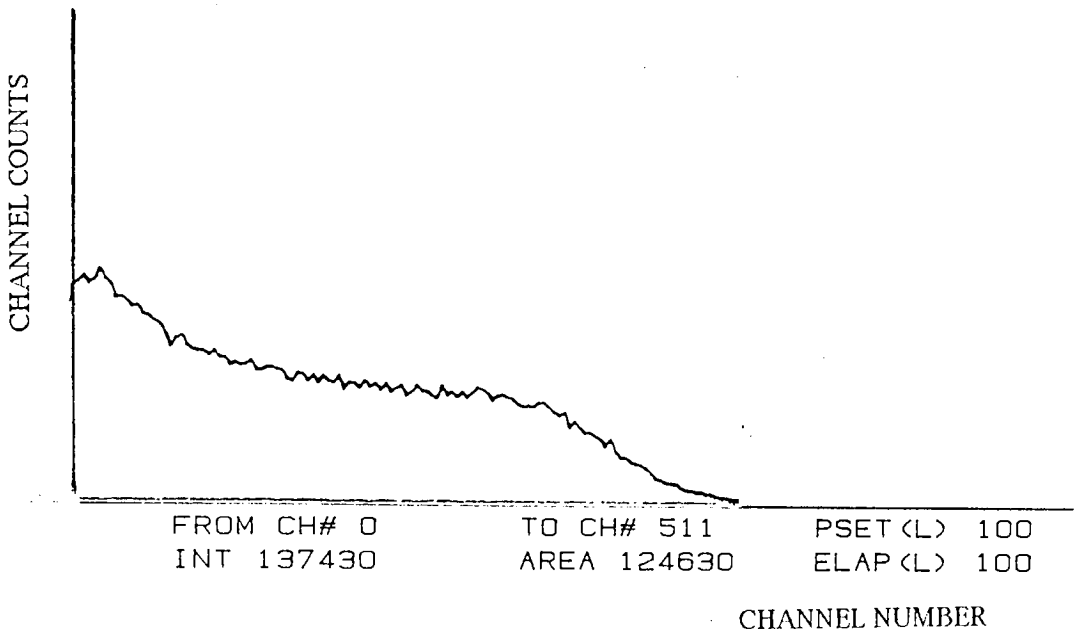

Figure 4.19 Gamma spectrum for ^{60}Co gamma source with B.B.Q.

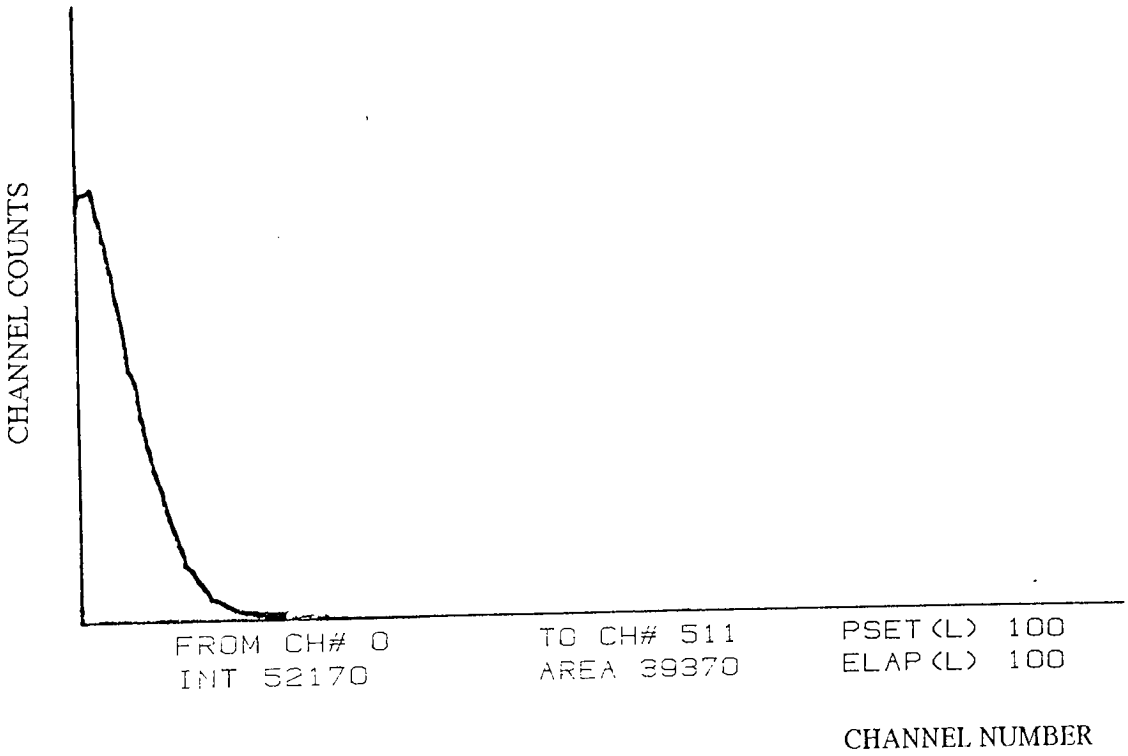

Figure 4.20 Gamma spectrum for ^{60}Co gamma source with (Fibre + B.B.Q.)

As discussed in Section 4.31, a lens cannot be used to improve the coupling efficiency when the source emitting area is larger than the fibre bundle core area. Hence, it was concluded that the maximum light transmission efficiency for the system was obtained when the scintillator was directly coupled to the optical fibre bundle, which in turn was directly coupled to the photomultiplier - the bialkali tube, to obtain the benefit of the extended spectral response of this photocathode.

CHAPTER FIVE: MEASUREMENT OF DOSE RATES WITH AN OPTICAL FIBRE COUPLED SYSTEM

5.1 Neutron and Gamma Discrimination:

The output from the pulse-shape discriminator (Sec. 3.3), when viewed on an oscilloscope, determines the performance of the detector system in separating neutron and gamma events. A typical oscilloscope display with good separation of neutron and gamma rays is reproduced in Figure 5.1(a). The corresponding oscilloscope display of a neutron-gamma source measured with the NE213 scintillator optically coupled to the 9789B bialkali photomultiplier by the optical fibre bundle is shown in Figure 5.1(b). It is evident that the system fails to discriminate between neutron and gamma rays in a mixed radiation field.

This photomultiplier used was selected to be used with the optical fibre bundle with a diameter of 10mm to give maximum coupling efficiency, a higher sensitivity in the green region of the spectrum, to increase the collection efficiency, and for its low dark current, essential for low count measurements. However, the photomultiplier has the disadvantage of a low time response (Table 4.2) and is slower than that of the NE213 liquid scintillator, preventing the system from being used in conjunction with a pulse-shape discriminator for measurements of neutron and gamma dose rates in mixed radiation fields.

Consequently, it was possible only to measure gamma dose rates (from a gamma source)

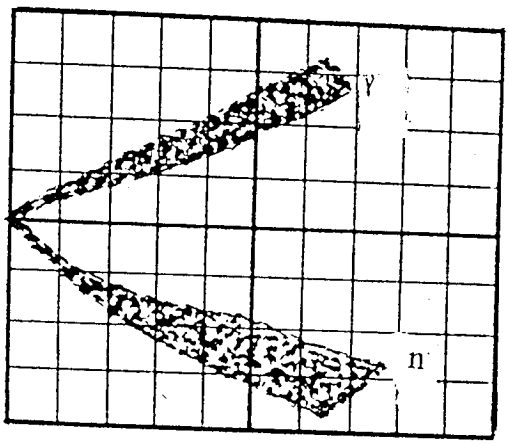

(a)

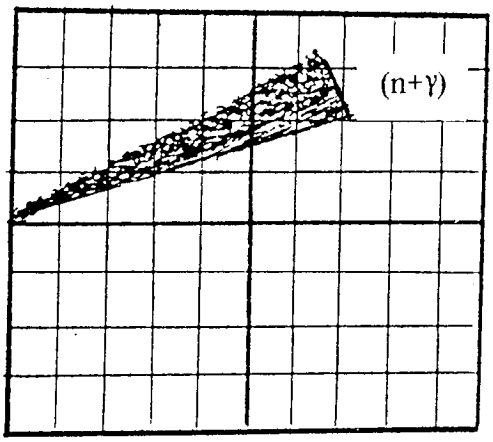

(b)

Figure 5.1 Sketch of oscilloscope display showing

a) - Gammas + Neutrons (discriminated)

b) - Gammas + Neutrons (non-discriminated)

and to investigate the effect of the perturbation of the field by the detector by using the optical fibre to couple the scintillator and photomultiplier. ^{60}Co and ^{137}Cs gamma sources were used for these measurements

5.2 Measurement of Gamma Dose Rates

The analysis follows that described in Section 3.3. Values of calculated and measured dose rates are presented in Table 5.1 for ^{60}Co gamma source of known activity, with the scintillator and photomultiplier directly coupled. Figure 5.2 presents a typical gamma spectrum.

A cesium 137 source of known activity was used to check further the accuracy of the system. The ^{137}Cs source had been purchased from Radio Chemical Centre, Amercham, providing, on the 23rd of June 1971, an activity of 5mc. At the time of measurements described in this chapter (January,1987), the absorbed dose at particular distances was calculated using the known ^{137}Cs half life of 30 years. These values are presented in Table 5.2 alongside experimentally measured dose rates. Figure 5.3 presents a typical gamma spectrum for the ^{137}Cs source with a directly coupled system.

The corrections and uncertainty factors detailed in (Section 3.2) must again be applied. Table 5.3 presents the uncertainty and correction factors applied to Tables 5.1 and 5.2, and Table 5.4 presents the corrected calculated and measured gamma dose rate for the ^{60}Co and ^{137}Cs gamma sources.

Position (m)	Calculated dose rate μGyh^{-1}	Measured dose rate μGyh^{-1}
1.0	21.90	20.87
0.5	87.60	83.50
0.3	243.34	232.11

Table 5.1: Calculated and measured dose rate for ^{60}Co gamma source

Position (m)	Calculated dose rate μGyh^{-1}	Measured dose rate μGyh^{-1}
1.0	12.81	11.93
0.5	51.24	46.14
0.3	142.34	128.11

Table 5.2: Calculated and measured dose rate for ^{137}Cs gamma source

Gamma Source	Position (m)	Source strength uncertainty μGyh^{-1}	Attenuation factor	Source detector position uncertainty μGyh^{-1}	Standard deviation of measurement μGyh^{-1}	Background correction μGyh^{-1}
^{60}Co	1.00	± 1.1	1.05	± 0.1	± 0.02	0.96
	0.5	± 4.4	1.05	± 0.8	± 0.4	0.96
	0.3	± 12.2	1.05	± 3.9	± 1.0	0.96
^{137}Cs	1.0	-	1.12	± 0.06	± 0.02	1.02
	0.5	-	1.12	± 0.5	± 0.3	1.02
	0.3	-	1.12	± 2.1	± 1.0	1.02

Table 5.3 : Correction and uncertainty factors for ^{60}Co and ^{137}Cs gamma sources

Gamma Source	Position (m)	Calculated dose rate μGyh^{-1}	Measured dose rate μGyh^{-1}
^{60}Co	1.0	21.9 ± 1.1	21.8 ± 0.1
	0.5	87.6 ± 4.4	87.6 ± 1.2
	0.3	243.4 ± 12.2	243.6 ± 4.9
^{137}Cs	1.0	12.81	12.13 ± 0.08
	0.5	51.24	50.1 ± 0.8
	0.3	142.34	141.71 ± 3.1

Table 5.4: Corrected, calculated and measured dose rate for ^{60}Co and ^{137}Cs gamma sources

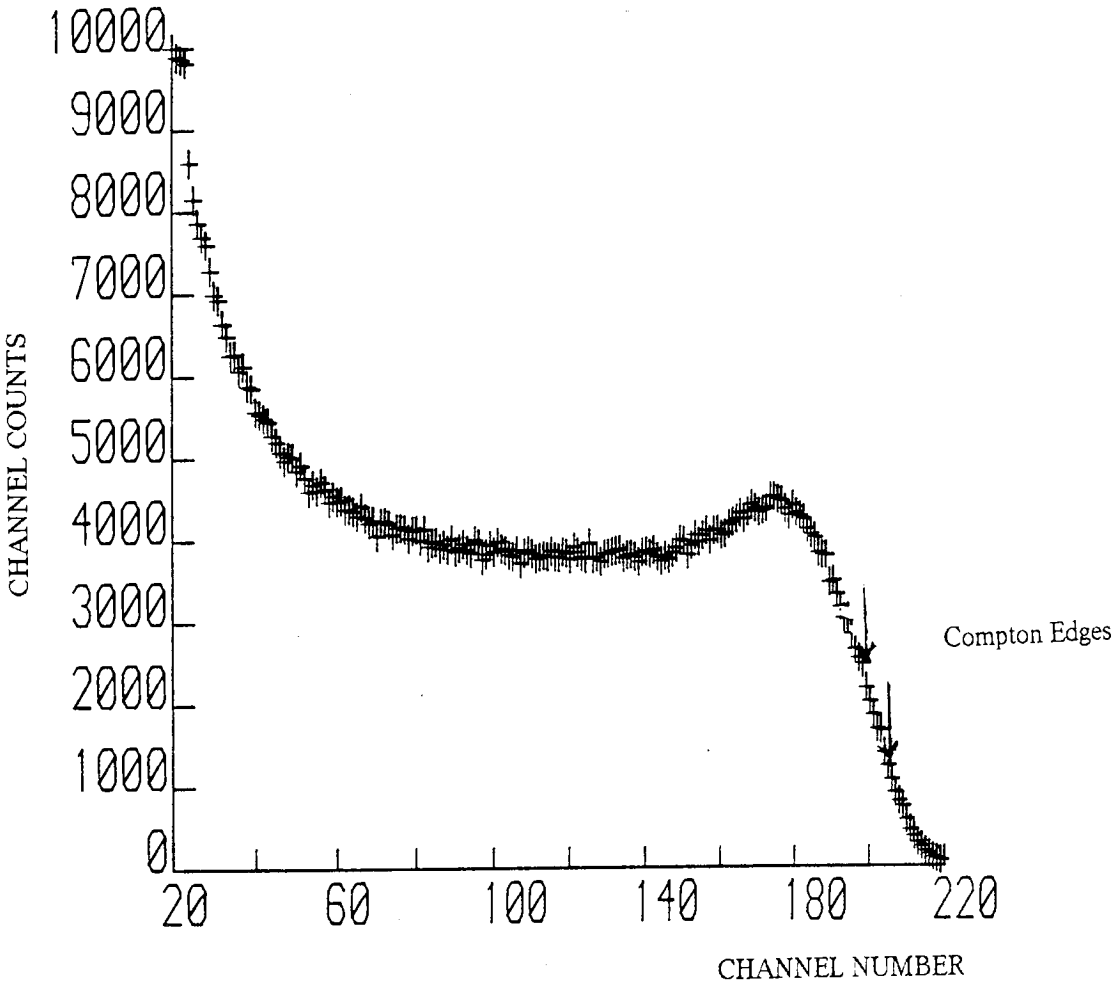

Figure 5.2 Gamma spectrum for ^{60}Co gamma source.

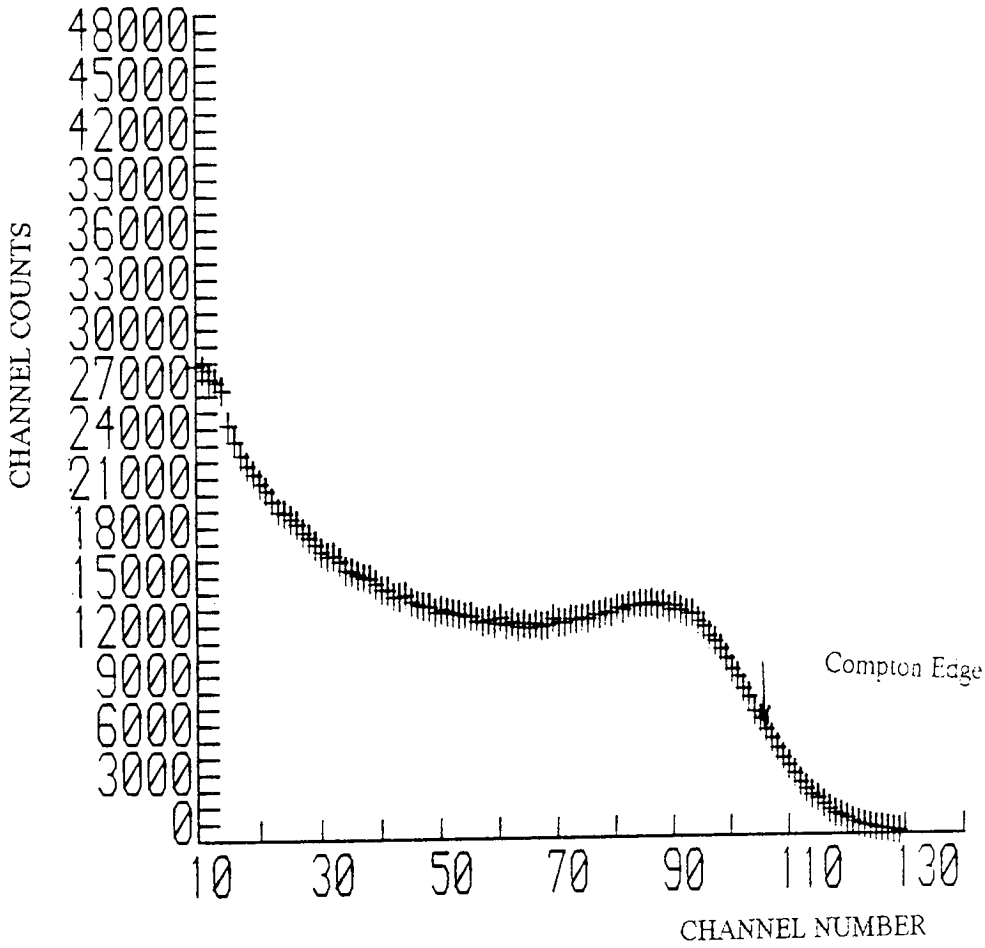

Figure 5.3 Gamma spectrum for ^{137}Cs gamma source.

A better agreement was reached between the calculated and the experimental results than previously, due to the very low dark current of the photomultiplier used, essential for low counting rates.

The results for a directly-coupled NE213 scintillator and photomultiplier system were then compared with measurements for an optically coupled system. Table 5.5 presents the calculated and measured dose rates for the ^{60}Co gamma source, and Table 5.6 for the ^{137}Cs source. Figures 5.4 and 5.5 present a typical gamma spectra for ^{60}Co and ^{137}Cs gamma sources, respectively. Table 5.7 presents the corrected, calculated and experimental results for the ^{60}Co and ^{137}Cs gamma sources, after applying the correction factors given in Table 5.3. The background dose is measured at 1.34 $\mu G_y h^{-1}$ for ^{60}Co and 1.23 $G_y h^{-1}$ for ^{137}Cs source.

The experimentally measured dose rates for the two gamma sources agree favourably, to within 5%, with the calculated results. A small difference between these results is due to a small reduction in the counting rate, when the level discriminator is used.

A comparison of the results in Table 5.7 with the results presented in Table 3.4, for the dose rates for the ^{60}Co gamma source, indicates that a better agreement was achieved between the calculated and measured results than previously, primarily due to the lower dark current for the photomultiplier used, and the reduced effect of the perturbation field by the detector.

Position (m)	Calculated dose rate μGyh^{-1}	Measured dose rate μGyh^{-1}
1.0	21.90	20.51
0.5	87.60	83.21
0.3	243.34	230.41

Table 5.5: Calculated and measured dose rate for ^{60}Co gamma source (fibre)

Position (m)	Calculated dose rate $\mu Gy h^{-1}$	Measured dose rate $\mu Gy h^{-1}$
1.0	12.81	11.95
0.5	51.24	45.96
0.3	142.34	128.45

Table 5.6: Calculated and measured dose rate for ^{137}Cs gamma source (fibre)

Gamma Source	Position (m)	Calculated dose rate μGyh^{-1}	Measured dose rate μGyh^{-1}
^{60}Co	1.0	21.9 ± 1.1	20.3 ± 0.1
	0.5	87.6 ± 4.4	86.11 ± 1.2
	0.3	243.4 ± 12.2	240.7 ± 4.9
^{137}Cs	1.0	12.81	12.06 ± 0.1
	0.5	51.24	49.6 ± 0.8
	0.3	142.34	141.24 ± 3.1

Table 5.7: Corrected, calculated and measured dose rate for ^{60}Co and ^{137}Cs gamma sources (fibre)

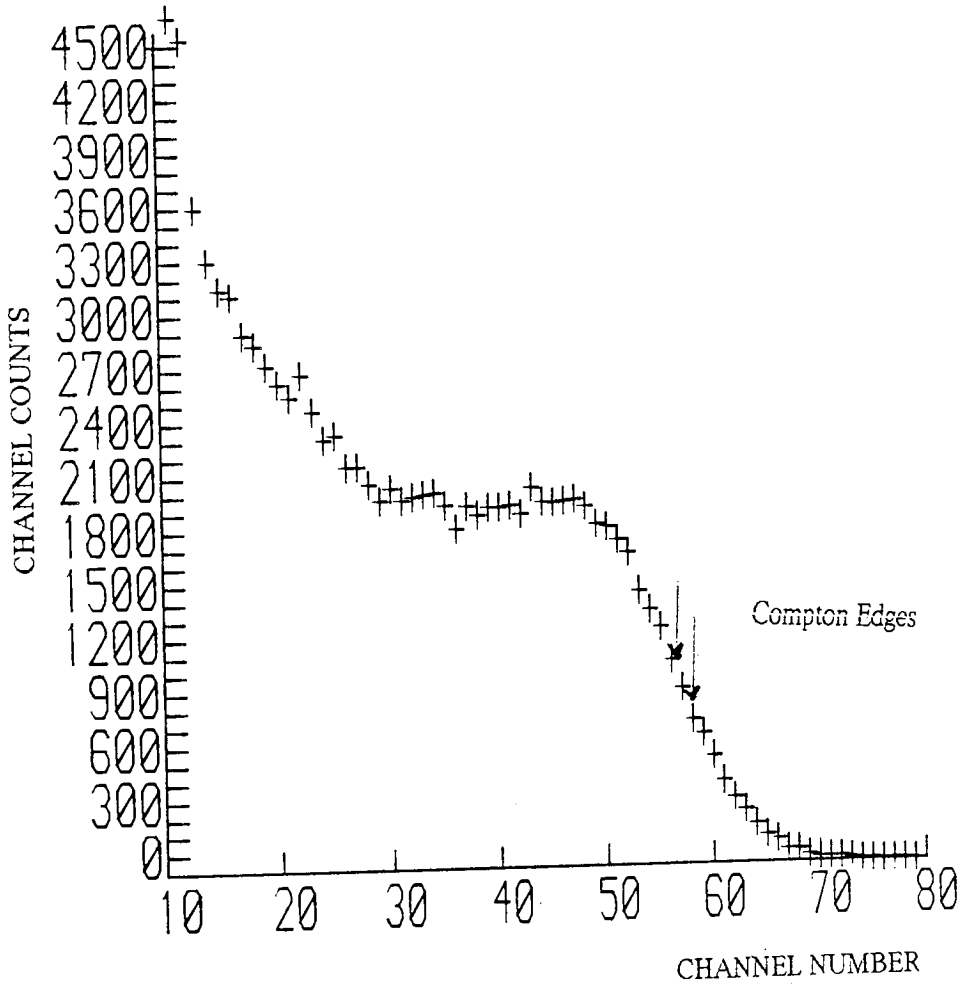

Figure 5.4 Gamma spectrum for ^{60}Co gamma source (fibre)

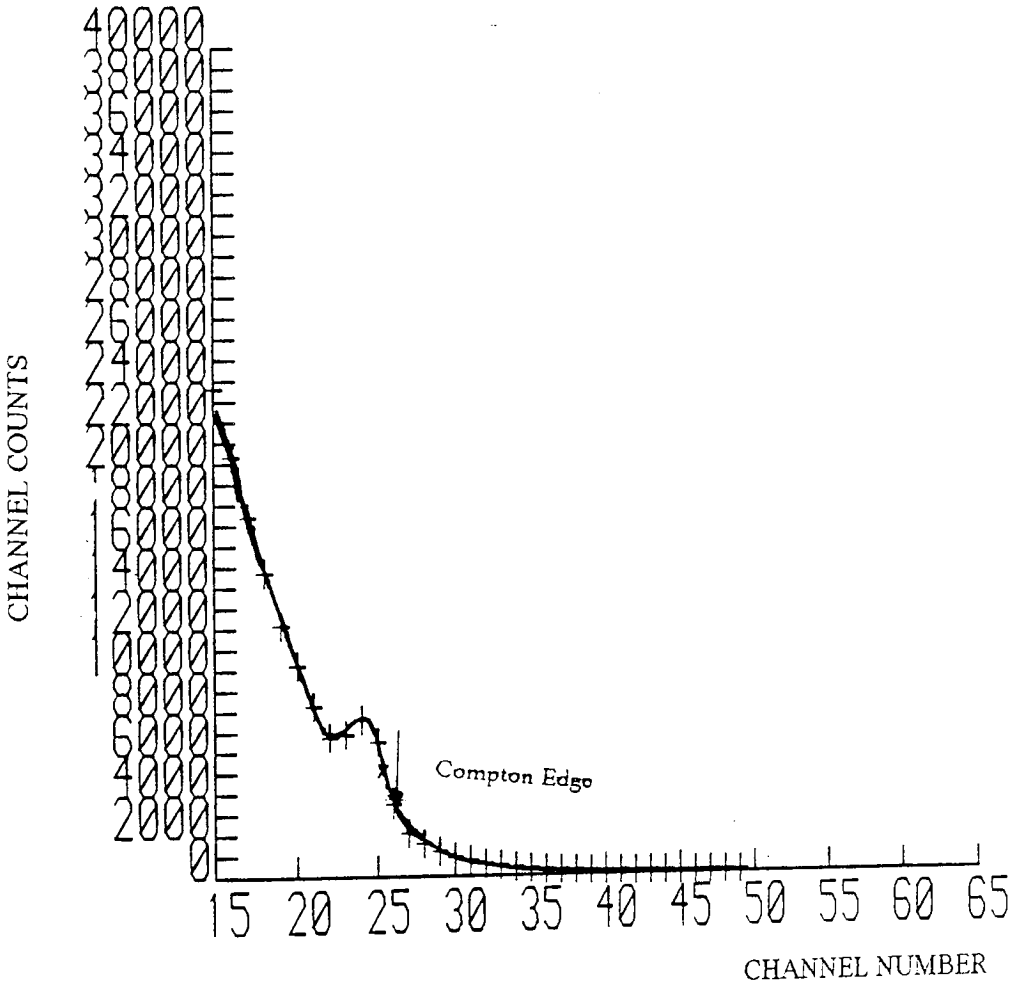

Figure 5.5 Gamma spectrum for ^{137}Cs gamma source (fibre).

In general, the new photomultiplier and detector system improved the measured dose rates from gamma sources, with and without the optical fibre bundle. However, the introduction of optical fibre coupling reduces the transmission efficiency of the detector system and, consequently affects the agreement between measured and calculated dose rates.

CHAPTER SIX : CONCLUSIONS AND SUGGESTIONS FOR FURTHER FUTURE WORK

6.1 Conclusions

The liquid scintillator NE213 was used successfully in conjunction with a pulse shape discriminator to measure neutron and gamma dose rates in mixed radiation fields. Agreement was reached with calculated dose rates and with the work of other authors (Section 3.3).

Measured dose rates from a gamma source, using a S11 photomultiplier tube directly coupled to a NE213 liquid scintillator (40mm x 40mm), were in agreement to within 5-10% of calculated results. The difference was due to the perturbation of the gamma field by the detector and from the dark current of the photomultiplier, which limits the calculations at the lower energy range for gamma. This problem was solved by using a higher quantum efficiency, lower dark current bialkali photomultiplier coupled to a smaller (12.7mm x 25.4mm) NE213 liquid scintillator. The gamma dose rates measured with this system were in very good agreement with the calculated results.

In addition, to further reduce the perturbation of the radiation field, a 10mm diameter fibre-optic bundle was used to couple the scintillator and photomultiplier. Measurement of dose rates for ^{60}Co and ^{17}Co gamma sources with the optically-coupled system showed sufficient agreement with the calculated results to indicate that it would be possible to construct a portable dosimetry system with an optimised combination of

photomultiplier and scintillator coupled by an optical-fibre bundle.

Unfortunately, whilst gamma and neutron dose rates in a mixed radiation field are successfully measured with a S11 photocathode photomultiplier, the optically de-coupled system, using a bialkali photocathode photomultiplier developed for gamma dose measurements, could not be used in a mixed radiation field. The slower time response of this system would not allow gamma neutron discrimination to be performed. Improvements to the detection system are suggested in the following section.

6.2 Suggestions for Further Future Work

The bialkali photomultiplier (EMI 9789B) was not fast enough to be used in conjunction with the pulse shape discriminator, which requires a fast response of 3 to 5ns for measurements of neutron and gamma dose rates in mixed radiation fields. This requirement could be met in several ways.

The 12.7mm diameter NE213 liquid scintillator, the dimensions chosen as a compromise between the detection efficiency and radiation field perturbation, could be used with a photomultiplier retaining the necessary high quantum efficiency and low dark current characteristics, but having a fast pulse rise time, for example the EMI 9893/350 bialkali photomultiplier with effective cathode diameter of 9mm, a fast response of 2.5ns and dark current of 0.1 to 1.0 nA lum^{-1}. An improvement of results could be expected due to the higher quantum efficiency and higher gain of this photomultiplier tube. Gamma-neutron discrimination should be possible with the improved rise time, even with optical fibre coupling of the scintillator and photomultiplier.

An alternative to the photomultiplier should be investigated. A possible replacement could be a blue/UV-enhanced silicon photovoltaic diode (EMI, Type 530532),* with spectral response in the range of 150nm to 1100nm (Figure 6.1) and effective sensitive area of 2.5mm x 3.5mm. This photodiode is primarily used for radiation monitoring. The rise time is controlled by the CR product (i.e. device capacitance time circuit series resistance). However, the unity gain of the photodiode may present serious signal-to-noise problems despite the advantage of good spectral match of the optical fibre bundle and photodiode, and higher quantum efficiency. Furthermore, a convex lens would need to be inserted between the fibre bundle and photosensor to maximise the coupling efficiency.

* THORN EMI ELECTRON TUBES LTD (U.K.)

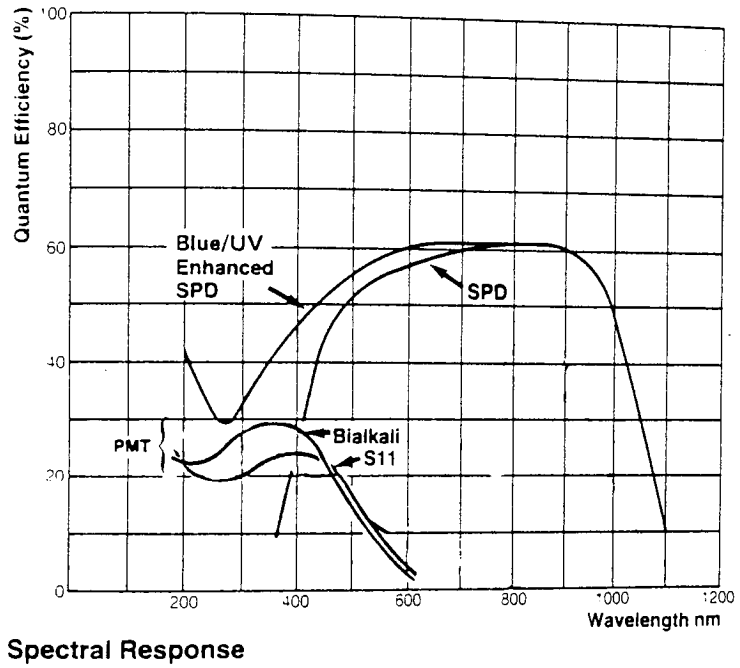

Figure 6.1 Photocathode (S11 + Bialkali) and silicon photodiode spectral response (Thorn EMI, 1984)

REFERENCES

W.Abson and R.P.Henderson. A twin ion chamber system for continuous monitoring of dose and dose rate from mixed neutron and gamma radiations. I.A.E.A, vol 2, (1962), p.331

K. K. Aglintsev. Applied dosimetry. London ILIFFE Books Ltd (1965).

F.H.Ahir, T.L.Johnson, E.J.West, A.E.Nash and S.G.Gobics. Thermoluminescent dosimeters for personal monitoring. Vol III of Proceedings of the congress on nuclear electronics and radio protection, Toulouse, France, (1968).

Z.B.Alfassi, L.Feldman and A.P.Kushelvesky. Gamma rays dosimetry by solutions of cholesteric liquid crystals. Radiation Effects Vol. 32, (1977), pp. 67-72.

I.O.Anderson and J.Braun. A neutron rem counter with uniform sensitivity from 0.025 ev to 10 Mev. (I.A.E.A.) Vol.2, (1962), p.87.

J.A.Axier, W.S.Snyder and J.D.Jones. Neutron interaction and penetration in tissue. Radiation Dosimetry, Vol.1, New York London Academic Press, (1968).

M.K.Batnoski. Fundamentals of optical fibre communications. New York London Academic Press, (1976).

E.E.B.Basch. Optical fibre transmission. Howard W. Sams and Co., (1986).

P.W.Benjamin. The use of recoil, proton methods for measuring neutron spectra in fast reactor. (I.A.E.A) Vol.1, (1962), p.307.

J.B.Birks. Theory and practice of scintillation counting. Pergammon Press, (1964).

A.Born and E.Wolf. Principles of Optics. 5th ed. Pergamon Press, New York (1965)

H.W.Breok and C.E.Anderson. The stilbene scintillation crystals as a spectrometer for continuous fast neutron spectra. Rev. Scint. Inst. 31, p.1063 (1960).

B.Brunfelter, J.Kockum and N.Starfelt. An organic scintillator as a spectrometer for neutrons in the 0.5 to 15 Mev range. (I.A.E.A.), Vol.2, (1962), p.351.

B.Burgkhardt, E.Piesch and D.Singh. High dose characteristics of LiF and $Li_2B_4O_7$, Thermoluminescent dosimeters. Nucl. Inst. and Method., 148 (1978), pp.613-617.

S.Cameron and L.Defronceshi. Method of determining fast neutron dose equivalent. Nucl. Inst. and Method., 50, (1967), p. 321.

R.S.Caswell, W.B.Beverly and V.Spieger Jr. Energy dependence of proportional counter fast neutron dosimeters. N.B.S., 75 Washington, D.C., (1963).

R.S.Caswell. Neutron - intensive proportoinal counter for gamma-ray dosimetry. Rev.Sci.Instr. Vol.31 (1960) p. 869

P.Christensen. Manganese activated lithium borate crystals, glasses and sintered pelefs as thermoluminescent dosimeters. Second International Conference on Luminescence Dosimetry, Denmark, (1968).

J.H.Cobb and D.J.Miller. A solid argon ionization chamber. Nucl. Inst. and Method., 141 (1977), pp. 433-437.

C.J.Daniels and J.L.Silberberg. A portable scintillation counter with pulse shape discrimination for measurement of fast neuton spectra and dose in mixed n-γ field. I.E.E.E. proceeding of Southeaston 77. Williamsburg, VA, (1977).

C.J.Daniels. A portable scintillation counter with pulse shape discrimination for measurements of fast neutron spectra and dose in mixed n-γ field. M.Sc. Thesis, Physics Departement, University of Maryland, (1976).

R.F.Duorak. A neutron monitor for simultaneous measurements of flourescences and dose equivalent. ANL-7085 (1965)

Ealing-Electro-Optics plc. Greycaine Road, Watford, England

G.G.Eichhotz and J.W.Poston. Principles of nuclear radiation detection. Ann Arbor, Mich Ann Arbor, (1979)

I.Faneinelli and M.Martini. Measurement of integrated thermal neutron doses by the Source-depletion method (I.A.E.A), Vol. 1, (1962), p.211.

D.F.Fitzgerald. Mathematical theory of radiation dosimetry. Gordon and Breach, (1967).

M.Fry. Neutron energy conversion factors for radioactive neutron sources. Health Physics 12 (1966), p. 855.

Y.Furruta and S.Tanaka. Fast neutrons thermoluminescent dosimetry. Nucl. Inst. and Method., 104, (1972), pp. 365-374.

M.Geither et al. Rev. Sci. Inst. 31(1976) p.450

R.J.Ginther and R.D.Kirk. Thermoluminescence of CaF_2.Mn and its application to dosimetry. Naval Research Lab. Progress Report (1956)

R.J.Ginther and R.D.Kirk. Thermoluminescence of CaF_2.Mn and its application to dosimetry. J.Electrochem. Soc. Vol.104 (1957) p.365

D. Gloge. Optical fibre Technology. Inst. Electr. (1971)

T.J.Gooding and H.G.Pugh. The response of plastic scintillators to high energy particles. Nucl. Inst. and Method., 7, (1960), p.189.

S.G.Gorbics, K.Kerris and F.H.Attix. Thermoluminescent dosimeters for high dose applications. Health Physics, Vol. 25 (1973), pp. 499-506.

L.H.Grey and J.Read. Measurement of neutron dose in biological experiments. Nature 144, p.439, (1939).

H.Gredez and M.Sabel. A stilbane scintillation counter with pulse-shape discrimination against gamma radiation for measurement of fast neutron spectra and dose. Neutron monitoring (I.A.E.A.) Vienna (1967), p.167.

J.A.Grundl, V.Speigel, C.M.Eisenhaure, H.T.Heaton, D.M.Gillian and J.Bigelow. A Californium -252 fission facility for neutron reaction rate measurements. Nucl. Tech., 32 (1977), p. 315.

F.D.Gvarrani and R.Malaroda. Two different technique measurements of the neutron spectrum of an Am-Be source. Nucl. Inst. and Method., 92, (1971).

D.E.Hankins. New methods of a neutron dose rate evaluation. Neutron Dosimetry, Vol.2, I.A.E.A., Vienna (1963) p.123

D.E.Hankins. A neutron monitoring intsrument having a response approximately proportional to the dose rate, from thermal to 7 MeV, LA 2717, (1962)

D.E.Hankins. A method of determining the intermediate energy neutron dose IDO - 16655 (1961)

D.E.Hankins. New methods of neutron dose-rate evaluation. I.A.E.A., Vol.2, (1962), p. 137.

F.X.Hass Jnr. and J.T. McCarthy. A stilbane fast neutron spectrometer for the study of a neutron spectrum of a Pu-Be source. Nucl. Inst. and Method. 50 (1967), p. 340.

.Hatsumi, R.Hiroshi and S.Takashi. A new Rem-counter for neutrons. Health Physics, Vol.13, p.559-565, (1967)

C.Hilsum and H.O.Rees. New low-loss liquid core fibre waveguides. Electronics Letters, 27th July, Vol. 8, No. 15, p.374, (1972).

.Hine and M.Brownwell. Radiation dosemetry, Academic Press Inc., (1965).

G.S.Hurst. An absolute tissue dosimeter for fast neutrons. British Journal of Radiology Vol.27 (1954) p.353

.C.R.U. International Commission for Radiological Protection and Units, (1962)

International Commission on Radiation Units and Measurements. Neutron Fluence, Neutron Spectra and Kerma, I.C.R.U. Report No. 13, (1969)

R.D.Johnson. Neutron dose conversion factors for Am-Be and Am-B sources. Health Physics, 12, (1966), p. 856.

D.W.Jones and M.E.Toms. A neutron spectrometer using organic scintillators. NRL Report 7324, Washington D.C, (1971)

P.Kaiser et al. A new optical fibre. Bell. Syst. Tech. J. Vol.52 No.2 (1973) p.265

C.J.Karzmark, J.White and J.F.Fowler. Lithium fluoride thermoluminescence dosimetry. Physics Med. Biol. No. 9, p.273

L.Kaufman, V.Perez-Mendez and G.Stoker. Performance of a pressurised xenon-filled multiwire proportional chamber. Nuc. Inst. & Methods (1972), p. 146.

D.B.Keck et al. Attenuation of multimode glass optical waveguides. Appl. phys. lett. 21(5) (1972) p.215

G.Keil. Scintillation counting with a fluorescence radiation converter. Nucl. Inst. and Method. 83, (1970), pp. 145-147.

I.B.Keirn-Marcus. Use of fissionable substances in neutron dosimetry. Neutron monitoring. (I.A.E.A.), 1971, p.425.

G.Keiser. Optical Fibre Communications. New York McGraw Hill, (1976).

G.F.Knol. Radiation detection and measurement. J. Wiley & Sons, (1979)

D.Kuppers et al. Preparation methods for optical fibres applied in Philips research. I00C77 p.319 Tokyo, July (1976)

W.Lahmann and A Hinzpeter. Measurement of average gamma-ray dose with uniformly distributed sources. I.J. Appl. Radiation & Isotop., 27 (1976), pp. 137-141.

L.Larson and R.Katz. Supralinearity of thermoluminescent dosimeters. Nucl. Inst. and Methods., 138 (1976), pp. 631-636.

J.M.Leak. Portable instrument for the measurements of the neutron dose equivalent rate in steady state and pulsed neutron fields. Neutron monitoring I.A.E.A., Vienna, (1967), p.313

J.B.MacChesney et al. Optical waveguides with very low losses. Bell System Technical Journal, 53, (May - June 1974), pp. 951-954.

J.B.Marion and J.L.Fowler. Fast neutron physics part 1, Interscience publishers Inc, New York (1960)

A.Martin. Introduction to Radiation Protection. Academic Press, 2nd edition (1979).

R.W.Matthews and D.F.Sangster. A comparison of some aqueous chemical dosimeters for absorbed doses of less than 100 rads. Int. J. Appl. Radiation & Isot. (GB), Vol. 29, No. 1, pp. 1-8, (1978).

S.A.McGuire. A dose instrument for neutrons from thermal to 100MeV LA 3435 (1966)

W.J.Meredith and J.B.Massey. Fundamental physics of radiology. Wright, (1967).

J.E.Midwinter. Optical fibre transmission. John Wiley & Sons, (1979).

S.E.Miller and A.G.Chynoweth. Optical fibre telecommunications. Academic Press (1979).

I.T.Myers. National Aeronautics and Space Administration. NASA. Lewis Research Centre, Cleveland Ohio (1968)

D.Nachtigal. Flounce-conversion curves and their applications to neutron calibration techniques with (α,n) sources. Neutron monitoring for radiological protection I.A.E.A. (1967), p. 633.

D.Nachtigal. Contribution of intermediate energy neutrons to the neutron dose equivalent outside the shielding of reactors and energy accelerators. Neutron monitoring I.A.E.A. (1967) p. 329.

D.Nachtigal. Average and effective energies, fluence-dose conversion factors and quality factors of neutron spectra of some (α,n) sources. Health Physics 13 (1967) p.213.

D.Nachtigal. Determination and measurement accuracy results of rem-counter measurements. Radiation dose measurements, (I.E.N.E.A.), (1967), p. 391.

D.Nachtigal. The comparison of average energy of a fast-neutron flux with portable neutron survey instruments. I.A.E.A. Vol. 2, (1962), p. 269.

(N.B.S.) National Bureau of Standard Handbook 84. Radiation quantities and units, Washington D.C. (1962)

N.B.S.) National Bureau of Standard Handbook 85. Physical aspects of radiation, Washington D.C. (1964)

N.B.S.) National Bureau of Standard Handbook 63 (1957)

N.C.R.P) International commission on radiological protection, Report 63, Table 193 (1961)

IEC Electronics (U.K.) Limited

M.Nair and J.Mitschke. Nucl. Inst. and Method. Vol.59 (1968) p.227

L.V.Neufield and W.S.Snyder. Selected topics in radiation dosimetry. I.A.E.A., Vienna (1961), p. 35.

E.Nuetfied. Comments on quality factor. Health Physics 17, (1969) p. 625

T.Okoshi. Optical fibres. Academic Press (1982)

R.Olshansky. Mode Coupling effects in graded index optical fibres. Appl. Opt. 14(4) (1975) p.935

H.Osanai et al. Spectral losses of low - OH - content optical fibres. Elect. Lett. Vol.12 No.12 (1960) p.310

G.H.Owyang. Foundations of optical waveguides. London Edward Arnold (1981).

G.Portal, F.Berman, P.L.Boanchard and R.Prigent. Improvement of sensitivity and linearity of radiothermoluminescent lithium fluoride. Department of Protection Intitute, (France), (1976).

S.Pretre. Neutron depth dose in man and corresponding quality factors, some heritical considerations. Proceeding of the International Congress on Protection against Accelerator and Space Radiation. Geneva Switzerland, 26-30 April 1971, (CERN), 1971, pp. 300-327.

S.Pszona. The NE102A organic scintillator as an acceptable LET dependent detector for quality factor and dose equivalent determinations in mixed radiation fields. Proceeding of the International Congress on Protection against Accelerator and Space Radiation. Geneva Switzerland, 26-30 April, (CERN), 1971, pp. 388-402.

J.J.Ritts, M.Solomito and P.N.Stevens. "Calculation of neutron fluence-to-kerma factors for human body". Nucl. Appl. and Tech. 1 (169), 89.

H.H.Rossi and W.Rosenzweg. A device for measurements of dose as a function of specific ionization. Radiology 64, p. 404, (1955)

H.H.Rossi. Ionization chambers in nuetron dosimetry. (I.A.E.A.), Vol. 2 (1962), p.55.

H.H.Rossi and G.Failla. Tissue-equivalent ionization chambers. Nucleonics. Vol.14, No.2 (1956) p.32

A.Rubbino. Energy spectra of neutrons from standard sources (Po-Be). Nuclear Physics 29 (1962) 507.

C.P.Sandbank. Optical fibre communication systems. John Wiley, Chichester (1980)

E.Schiel. U.S. Army Electronics Command. N.J.Ft. Monmouth (1974)

J. Senior. Optical fibre communication, Principles and Practice. Prentice/Hall International (1985)

J.L.Silberbeg and R.L.Walchle. Evaluation of a portable neutron spectrometer / kerma rate meter. IEEE Transactions on Nuclear Science, Vol. NS-25, No. 1, (1978), pp. 81-85.

J.L.Silberberg. Design of a microcomputer processing sub-system for a portable neutron spectrometer / kerma-rate meter. M.Sc. Thesis, Electrical Engineering Department, University of Maryland, (1976)

J.L.Silberberg. A microprocessor system for a portable neutron spectrometer. Kerma/rate-meter. I.E.E.E. Trans on Nucl. Scint., Vol. NS-24, No.1 (1977), pp. 386-390.

A.B.Smith, R.R.Fields and J.H.Roberts. Spontaneous fission neutron spectrum of Cf-252. Physics Rev., 108 (1957), 411.

E.Snitzer. Cylindrical dielectric waveguide modes. J. Opt. Soc. Am 51(5) (1961) p.491

W.S.Snyder. Measurement of neutrons and mixture of gamma and neutron dose rate. N.B.S. Handbook Vol.75 (1961)

C.E.E.Stewart, D.Tyldsley, B.Scott, H.Rawson and G.R.Newns. High purity glasses for optical fibre communication. Electronics Letters, 9, 21 (October 1973) 482-483

J.Stone. Optical transmission in liquid core quartz fibres. Appl. Phys. Lett. Vol. 20, No. 7, April, (1972).

F.Surny and M.Kralik. A new thermoluminescent detector for 14.7 Mev neutrons. Nucl. Inst. and Methods, 137 (1966) 593-594.

S.I.Tanaka and Y.Furruta. Estimation of gamma-ray exposure in mixed gamma-neutron fields by ^{6}LiF and ^{7}LiF thermoluminescence dosimeters in pair use. Nucl. Inst. and Methods, 117 (1974) 93.

S.I.Tanaka and Y.Futura. Usage of thermoluminescent dosimeters as a thermal neutron detector with high sensitivity. Nucl. Inst. and Methods. 133 (1976) 495.

G.V.Tapin. Chemical and colormetric indicators in radiation dosimetry. (G.J.Hing and Brownell ed.), (1956)

H.Tatsuta. A new rem counter for neutrons. Health physics Vol.13 (1967) p.559

R.Tiedeken. Fibre optics and its applications. London press (1973)

M.N.Thompson and J.M.Taylor. Neutron spectra from Am-Be and Ra-Be sources. Nucl. Inst. and Methods, 37 (1965) p.305

L.I.Tingye. Optical Fibre Communications. Vol. 1, Academic Press, Harcourt Brace Jovanovich, (1985).

J.G.Titchmarsh. Fibre control with the double crucible technique. Proceedings of the Second European Conference on Optical Fibre Communications, Paris, (1976), pp. 41-45

E.Tochlin and B.W.Shumway. Dosimetry of neutrons and mixed (n + γ) fields. Radiation Dosimetry, Vol. III, New York London Academic Press, (1969).

A.R.Tynes et al. IEEE. J. Quantum Electron. QE 8(2) (1972) p.217

V.V.Verbinski and W.R.Burrus. Proton-recoil neutron spectrometry with organic scintillators. Neutron monitoring (I.A.E.A.), Vienna, (1967), p.151

E.J.Wenham, G.W.Dorling, J.A.N.Snell and B.Taylor. Physics, concepts and models, Addison Wesley, London (1972)

P.M.Whelan and M.J.Hodgson. The Essential Principles of Physics. John Murray, London, (1979)

W.H.Wike. Intrinsic efficiency of thermoluminescent dosimetry phosphors. NRL Report 7104 (1970)

F.S.Williamson and P.Mitacek Jr. Calculation of kerma due to fast neutrons in tissue like materials. In neutron monitoring, I.A.E.A., Vienna (1967), p.17

C.Wingate, E.Tochlin and N.Goldstein. The response of LiF to neutrons and charged partices in thermoluminescence dosimetry. Proc. Int. Conf. Luminescence Dosimetry, Stanford University, (1965) Conf. 65037, p.421, U.S.A., At. Energy, Oak Bridge, Tennessee.

H.F.Wolf. Handbook of Optical Fibres, Theory and Applications. Granada, London (1979)

R.Yokota, I.Niyamaga, R.Nariyama and Y.Nishiwaki. The basic principles and role of glass dosimeters in personal dosimetry. (I.E.N.E.A.), (1967), p. 87.

APPENDIX A : MEASUREMENT OF GAMMA DOSE RATE (FORTRAN 77)

```
      MASTER GAMMA
      DIMENSION C(511)
      READ (1,200)SM,DE
200   FORMAT (2F0.0)
      WRITE (2,600) SM,DE
600   FORMAT (17H  SCINTILLOR MASS = ,F8.3,23HKG  ENERGY PER CHANNEL =,
     # 1F8.5,3HMEV)
      CALL  CANSPEC (C, T, 3)
      SUM = 0.0
      DO  10  I = 1, 511
      SUM = SUM + C (I) * (I - 0.5)
 10   CONTINUE
      DOSR := SUM * DE / (SM * 17   36 * T)
      WRITE (2,300) DOSR
300   FORMAT (1HO, 9HDOSERATE =, F8.3, 7H μSV / H)
      STOP
      END
      SUBROUTINE  CANSPEC (C, T, M)
      DIMENSION N(575), C(511)
      DATA  10 / 4H    0 /
   4  FORMAT (A4)
   1  READ (M, 4) ICH
      IF (ICH.NE.10) GO TO 1
   5  FORMAT (10)
      READ (M,5) (N(I), I = 1, 575)
      T = N (1)
      DO  2  I = 1,7
      C(I) = N(I + 1)
   2  CONTINUE
      J = 0
      DO  3  I = 8, 504, 8
      J = J + 1
      DO  3  K = 1, 8
      C (I + K - 1) = N (I + K + J)
   3  CONTINUE
      RETURN
      END
      FINISH
```

APPENDIX B: MEASUREMENT OF NEUTRON DOSE RATE (FORTRAN 77)

```
      MASTER NEUTRON
      DIMENSION C(511)
      READ (1, 200) SM, DE
200   FORMAT (2F0.0)
      WRITE (2,600)SM, DE
600   FORMAT (17H SCINTILLOR  MASS =, F8.3,23HKG  ENERGY PER CHANNEL =,
     # 1F8.5, 3HMEV)
      QF = 7.4
      CALL CANSPEC (C, T, 3)
      SUM = 0.0
      N = INT (1.85 / DE)
      DO  10  I = 1, N
      SUM = SUM + C (I) * 3.48 * (I * DE) * * 0.666
 10   CONTINUE
      DO  20  I = N + 1, 511
      SUM = SUM + C (I) * 1.78 * (I * DE + 1.1)
 20   CONTINUE
      DOSR = SUM * QF / (SM * 17  36 * T)
      WRITE (2, 300) DOSR
300   FORMAT (1H0, 9HDOSERATE =, F8.3, 7H  μSV / H)
      SUBROUTINE  CANSPEC (C, T, M)
      DIMENSION  N(575), C(511)
      DATA  10 / 4H   0 /
  4   FORMAT (A4)
  1   READ (M, 4) ICH
      IF (ICH.NE.10) GO TO 1
  5   FORMAT (10)
      READ (M, 5) (N (I), I = 1, 575)
      T = N (1)
      DO  2  I = 1, 7
      C(I) = N(I+1)
  2   CONTINUE
      J = 0
      DO  3  K = 1, 8
      C(I + K - 1) = N(I + K + J)
  3   CONTINUE
      RETURN
      END
      FINISH
```

APPENDIX C : OPTICAL FIBRE THEORY

Most common fibres are glasses or plastic, although a liquid has been used (C.Hilsum and H.D. Rees, 1972). Many plastics are excluded from further consideration because of the presence of hydrogen in their structure, which gives rise to very high transmission loss, and their molecular size which leads to large scattering losses.

Propagation within the uniform core of the step-index wave guide, Figure C1 is along straight lines. If a ray originates at P on one interface and makes an angle θ_z with the wave guide axis, it will meet the opposite interface at Q. The situation at Q is equivalent to incidence at an interface between two half-spaces of refractive indices n_{co} and n_{cl}, as shown in Figure (C2a,b). Reflection in this situation is governed by Snell's law: $n_{co} \cos \theta_z = n_{cl} \cos \theta_t$, which are usually expressed in terms of angles relative to the normal Q N. Thus, in terms of complementary angles, the incident ray at Q is totally internally reflected if $o \leq \theta_z < \theta_c$, and is partly reflected and partly refracted if $\theta_c < \theta_z \leq \pi/2$, where θ_c is the complement of the critical angle, defined by:

$$\theta_c = \cos^{-1}\left[\frac{n_{cl}}{n_{co}}\right] = \sin^{-1}\left[1 - \frac{n_{cl}^2}{n_{co}^2}\right]^{1/2}$$

In the first case, Figure C.2a shows the refracted ray leaving the interface at the same angle θ_z as the incident ray, while in the second case, Figure C.2b, part of the ray is reflected at angle θ_z and part of it transmitted to the cladding at an angle θ_t to the interface, which satisfies Snell's law.

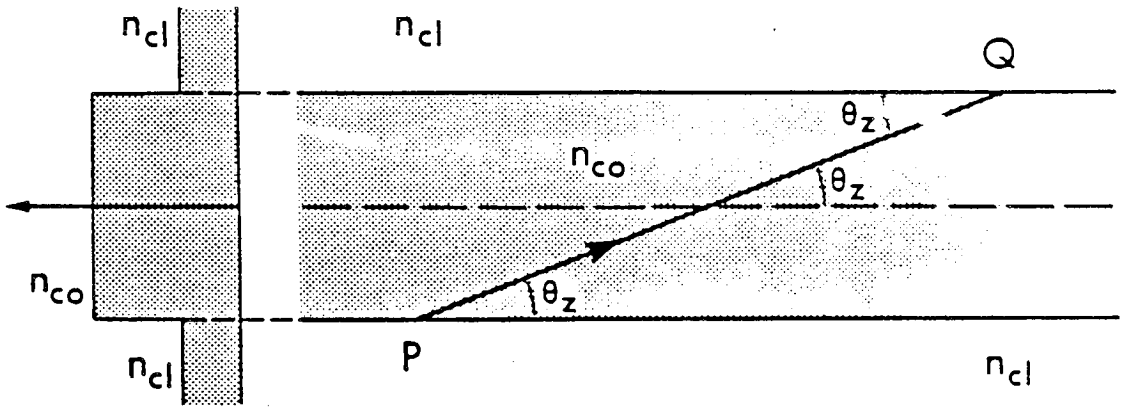

gure C_1 Propagation along a straight line between interfaces in the core of a step-profile planar wave-guide.

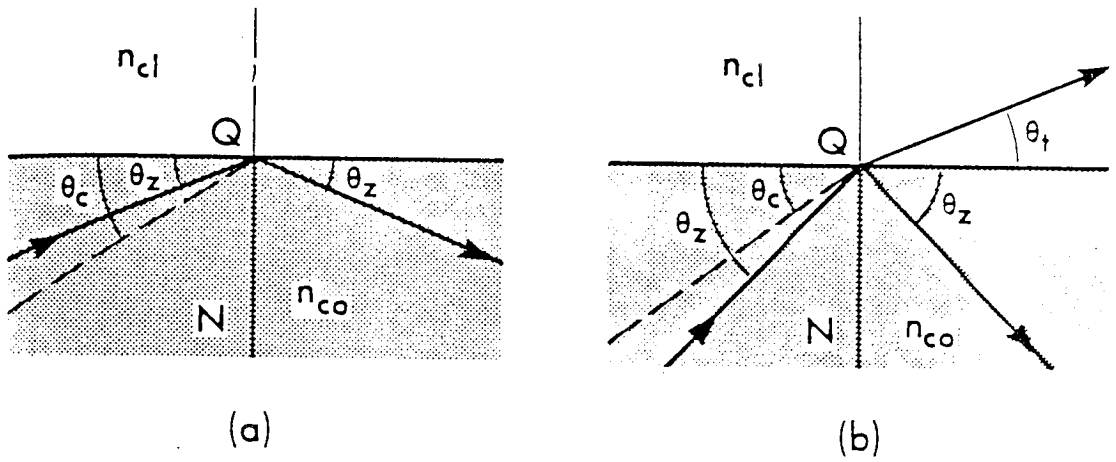

Figure C_2 Reflection at a planar interface between unbound regions of refractive indices n_{co} and n_{cL}, showing
a) reflection and b) partial reflection and refraction.

Only total internal reflection returns all the ray power, i.e. the energy flowing along the ray, back into the core medium. A ray is reflected from the interface into the core at angle θ_z regardless of whether partial or total reflection occurs. A ray which is totally reflected at every reflection is referred to as a bound ray, since its path is entirely confined within the cores (a), while a ray that is partly reflected at each reflection is referred to as a refracting ray. These rays may be categorised by the value of θ_z according to:

Bound ray : $0 \leq \theta_z < \theta_c$

Refracting rays : $\theta_c \leq \theta_z \leq \pi/2$

Since the power of the bound ray is totally reflected back into the core at every reflection, the ray can propagate indefinitely without any loss of power.

APPENDIX D: OPTICAL FIBRES AND DIFFUSE SOURCES

A diffuse or lambertian source is one where each differential area dA of the source area emits light in all directions, i.e. $\theta_z = \pi/2$ (Figure D). The source emits light within a cone of half angle θ_o to the normal, has intensity $I(\theta_o)$ per unit solid angle per unit area of source. The element power dP radiated is given by:

$$dP = I(\theta_o)\, d\Gamma\, dA \quad 0 \le \theta_o \le \theta_s$$

$$dP = 0 \quad \theta_s \le \theta_o \le \pi/2 \quad 0 \le \theta_o \le \theta_s$$

For a lambertian source, the intensity distribution is given by :

$$I(\theta) = I_o \cos\theta_o \quad \le \theta_o \le \pi/2 \; 0 \le \theta_o \le \pi/2$$

& $B(\theta, \phi) = B_o \cos\theta_o$

$I(r) = A \exp(-\alpha\, r^2 / r_s^2)$, where r_s is the source radius and A & α are positive constants.

If the source radius r_s is less than the fibre core radius a, for a lambertian emitter:

$$B(\theta, \phi) = B_o \cos\theta_o \quad \text{and}$$

$$P_f = \int_o^{r_s} \int_o^{\pi/2} (2\pi B_o) \int_o^{\theta_{omax}} \cos\theta_o \sin\theta_o \, d\theta_o \, d\theta_s \, rdr,$$

$$= \pi B_o \int_o^{r_s} \int_o^{2\pi} NA \, d\theta_s \, rdr = \pi^2 r_s^2 B_o NA^2 \qquad \text{.....D1}$$

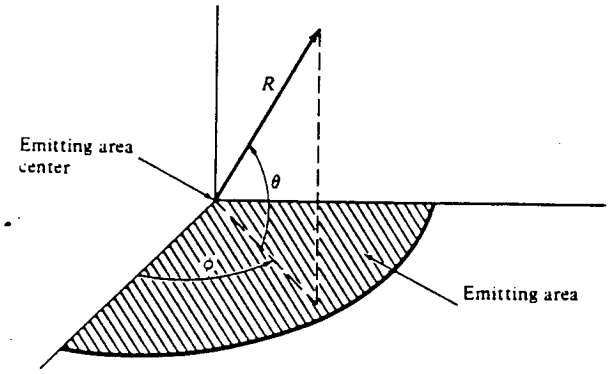

Figure D Characteristic emission pattern for a diffused optical source

The total optical power P_s that is emitted from the source of area A_s into a hemisphere ($2\pi sr$) is given by:

$$P_s = A_s \int_0^{2\pi} \int_0^{\pi/2} B(\theta,\phi) \sin\theta_o \, d\theta \, d\phi$$

$$= \pi r_s^2 \; 2\pi \; B_o \int_0^{\pi/2} \cos\theta_o \sin\theta_o \, d\theta$$

$$= \pi^2 \; r_s^2 \; B_o \qquad \text{.....D2}$$

Equations D1 and D2 give the coupling efficiency $\Im_{max}$ for step-index fibre,

$\Im_{max} = NA^2$ for $r_s \leq a$

$= NA^2 (a/r_s)^2$ for $r_s > a$

For graded index fibre, where NA depends on the distance r from the fibre axis, for $r_s < a$

$$P_f = 2\pi^2 B_o \int_0^{r_s} (n^2(r) - n_{cl}^2) \, r \, dr$$

$$= 2\pi^2 r_s^2 B_o n_{co}^2 \Delta \left[1 - \frac{2}{\alpha+2} \left(\frac{r_s}{a} \right)^{\alpha} \right]$$

$$= 2P_s n_{co}^2 \Delta \left[1 - \frac{2}{\alpha+2} \left(\frac{r_s}{a} \right)^{\alpha} \right]$$

$$\Im_{max} = \frac{P_f}{P_s} = 2n_{co}^2 \Delta \left[1 - \frac{2}{\alpha+2} \left(\frac{r_s}{a} \right)^{\alpha} \right]$$

$$= NA^2 - \frac{NA^2}{2} \left(\frac{r_s}{a} \right)^2 \quad \text{for } \alpha = 2 \ \& \ r_s < a \text{ (core)}$$